# Cavity Expansion Theory and its Application to the Analysis of Pressuremeters

by

**Hai-Sui Yu**

B.Sc. (Eng.), M.Sc., D.I.C.

A thesis submitted for the
Degree of Doctor of Philosophy
at the University of Oxford

St. Anne's College

Trinity Term, 1990

# Abstract


**Cavity Expansion Theory and its Application to the Analysis of Pressuremeters**

**H. S. Yu**
**St. Anne's College, University of Oxford**

A thesis submitted for the Degree of Doctor of Philosophy
Trinity Term, 1990

The successful application of in-situ testing of soils heavily depends on development of methods of interpretation of the tests. The purpose of this thesis is to develop a consistent theoretical basis for the interpretation of pressuremeter tests in cohesive and frictional materials. The research programme is based on cavity expansion theory with additional details provided by a large strain finite element analysis.

A unified analytical solution is developed for the expansion and contraction of both cylindrical and spherical cavities in dilatant elastic-plastic soils. For the first time, explicit solutions for the pressure-expansion and pressure-contraction relationships are derived without any restriction being imposed on the magnitude of the deformation.

In addition, the finite element method is adopted for solving the cavity expansion problem. This is mainly due to the fact that only in special cases when simple material models and boundary conditions are involved has it been possible to solve the problem analytically. A finite element analysis of the cone-pressuremeter test in sand is described.

A series of two-dimensional finite element calculations on both the self-boring pressuremeter test and the cone-pressuremeter test is performed. In modelling the penetration process of cone-pressuremeter tests, the stresses evaluated by the cavity expansion theory are used as the starting condition for the finite element analysis. Emphasis is placed on quantifying the effects of pressuremeter geometry on derived deformation and strength parameters.

In the finite element formulation, a special effort is devoted to developing a lower order finite element suitable for analysing axisymmetric elastic-plastic problems which involve incompressibility constraints. The formulation of a new six-noded isoparametric displacement finite element is presented. To account for large strain (rotation) effects, an Eulerian description of deformation is adopted and the Jaumann stress rate is used in the soil constitutive equations.

The suitability of the conventional interpretation methods for pressuremeter tests is critically assessed in the light of the finite element results. Based on the numerical results, improved procedures for obtaining in-situ soil parameters from pressuremeter tests in both clay and sand have been proposed.

# Acknowledgements

The research described in thesis was carried out at Oxford during the period September 1987 to July 1990. The financial support of a Technical Co-operation Award provided by the Chinese Educational Committee and British Council is gratefully acknowledged.

First of all, I wish to express my thanks to my supervisor, Dr. Guy Houlsby, for his advice and guidance and allowing me to use his mesh generation program to produce the two-dimensional finite element meshes used in the research. The discussions we had during different phases of the research have proved to be most valuable in helping me to clarify my ideas and strengthen my arguments.

I am indebted to Professor Peter Wroth for his stimulation and encouragement while I was involved in the development of the closed form solution for the cavity expansion problem. I would also like to thank Dr. Scott Sloan for his help during the early stages of the research.

My thanks go to all other members of the Soil Mechanics Research Group for their advice and encouragement. In particular, I am grateful to Dr. H.J. Burd for his supervision during the period when Dr. Guy Houlsby was away on sabbatical leave and providing me a copy of the frontal solver program. I would also like to thank Dr. H.J. Burd and Dr. C.I. Teh for allowing me to use some of their stress-update routines in the development of two-dimensional finite element formulation. In order to give a complete description of the two-dimensional finite element formulation, a description of some of the basic procedures is given. In Section 3.5 a discussion is given of the solution scheme used in the program; this discussion follows closely Section 2.4 in Dr. Burd's thesis and is repeated here with his permission. Sections 5.8 (except 5.8.2) and 5.10 on the general description of constitutive models and stress update procedures for axisymmetric finite

element analysis are mainly based on Chapters 3 and 4 of Dr. Burd's thesis for the plane strain case with minor modifications for the case of axisymmetry. The inclusion of these Sections in this thesis is purely for the sake of completeness. I am also grateful to Fernando Schnaid for the many discussions we had on various aspects of pressuremeter tests.

To the best of the Author's knowledge, the following four aspects of the thesis are original, namely the analytical study (Chapter 2), the modified finite element formulation (Section 3.3 and Section 5.4 to Section 5.6), the constitutive modelling (Section 3.4 and Section 5.8.2) and the parametric studies of pressuremeter tests (Chapter 4 and Chapter 6). Where the Author has derived any information from other references, these have been duly cited in the text, to these authors I would like to record my gratitude.

The privilege of studying under Professor E.T. Brown at Imperial College before I started my research at Oxford remains memorable and his continuous encouragement and suggestion are very much appreciated.

Last, but by no means least, I would like to thank my wife Xiuli for her continuous understanding, patience and love, which has always been a source of inspiration during the course of my study.

Assumptions, hasty, crude and vain,
Full oft to use will science deign;
The corks the novice plies today,
The swimmer soon shall cast away.

A.H. Clough, Poem (1940)

To

my wife and
my parents

# Nomenclature

## Chapter 1

| | |
|---|---|
| $A, c$ | Constants |
| $G$ | Shear modulus |
| $I_r$ | Rigidity index |
| $K$ | Function of the critical state friction angle |
| $m$ | Factor identifying cavity type |
| $P$ | Pressure of cavity expansion |
| $P_l$ | Limit pressure of cavity expansion |
| $s_u$ | Undrained shear strength |
| $S_d$ | Plastic pressuremeter loading slope |
| $u_0$ | In-situ pore pressure |
| $\sigma_{h0}$ | In-situ total horizontal stress |
| $\sigma'_{h0}$ | In-situ effective horizontal stress |
| $\tau$ | Shear stress |
| $\phi'$ | Effective friction angle |
| $\psi$ | Dilation angle |
| $\phi'_{cv}$ | Critical state friction angle |

## Chapter 2

| | |
|---|---|
| $a$ | Radius of the cavity during loading |
| $a_0$ | Radius of the cavity at initial unloaded state |

| | |
|---|---|
| $a''$ | Radius of the cavity during unloading |
| $A, B$ | Constants of integration |
| $A_n^1, A_n^2$ | General terms of the series |
| $b$ | Outer radius of the plastic zone during loading |
| $b''$ | Position of outer radius of the loading plastic zone during unloading |
| $c$ | Cohesion of the soil |
| $d$ | Position of outer radius of the reverse plastic zone at fully loaded state |
| $d''$ | Outer radius of the reverse plastic zone during unloading |
| $E$ | Young's modulus |
| $G$ | Shear modulus |
| $m$ | Factor identifying cavity type |
| $n$ | Integer from zero to infinity |
| $p$ | Applied cavity pressure |
| $p_0$ | Initial hydrostatic pressure |
| $p_\infty$ | Limit applied cavity pressure |
| $p_1$ | Applied cavity pressure causing the first yielding |
| $p_2$ | Applied cavity pressure causing the first reverse yielding |
| $r$ | Material radius measured from initial unloaded state during loading |
| $r_0$ | Material radius at initial unloaded state |
| $r''$ | Material radius measured from initial unloaded state during unloading |
| $u$ | Radial displacement during loading measured from unloaded state |
| $u'$ | Radial displacement during unloading measured from fully loaded state |

| | |
|---|---|
| $u''$ | Radial displacement during unloading measured from unloaded state |
| $x$ | Unloading factor |
| $x_2$ | Unloading factor causing the first reverse yielding |
| $(x, y)$ | Auxiliary variables |
| $Y$ | Function of cohesion and friction angle |
| $z$ | Axial direction for cylindrical cavity |
| $\sigma, \epsilon$ | Stress and strain vectors during loading measured from initial state |
| $\sigma', \epsilon'$ | Stress and strain vectors during unloading measured from fully loaded state |
| $\sigma'', \epsilon''$ | Stress and strain vectors during unloading measured from initial state |
| $\sigma_R$ | Cavity pressure ratio |
| $\sigma_{R\infty}$ | Limit cavity pressure ratio |
| $\nu$ | Poisson's ratio |
| $\alpha$ | Function of friction angle |
| $\beta$ | Function of dilation angle |
| $\phi$ | Friction angle |
| $\psi$ | Dilation angle |
| $\Omega, \eta$ | Non-dimensional coefficients |
| $(\rho, \zeta)$ | Auxiliary variables |
| $\kappa, \lambda$ | Non-dimensional coefficients |
| $\Lambda_1, \Lambda_2, \Lambda_3$ | Power Series |

## Chapter 3

| | |
|---|---|
| $[B]_{ij}$ | Matrix relating strain rate and nodal velocity |
| $C_0, C_1$ | Constants of displacement interpolation |
| $C_2, C_3$ | Constants |

| | |
|---|---|
| $[D]^e$ | Elastic material matrix |
| $[D]^{ep}$ | Elastic-plastic material matrix |
| $f, g$ | Yield function and plastic potential respectively |
| $G$ | Shear modulus |
| $[K]_{ij}$ | Elemental stiffness matrix |
| $K_{ss}$ | Radial stiffness of infinite spring element |
| $m$ | Factor identifying cavity type |
| $[N]_{ij}$ | Shape function matrix |
| $\mathbf{P}$ | Nodal force vector |
| $r$ | Radial coordinate |
| $r_n$ | Inner radius of the infinite spring element |
| $u$ | Radial velocity |
| $\underline{u}$ | Radial nodal velocity vector |
| $\lambda_1, \lambda_2$ | Scalar multipliers |
| $\dot{\epsilon}$ | Strain rate vector |
| $\dot{\sigma}$ | Cauchy stress rate |

## Chapter 4

| | |
|---|---|
| $a$ | Final radius of the cavity |
| $a_0$ | Initial radius of the cavity |
| $C_d$ | Chamber to testing device diameter ratio |
| $G$ | Shear modulus |
| $I_r$ | Rigidity index |
| $m$ | Factor for identifying cavity type |
| $n, N$ | Functions of $\nu$, $\phi$ |
| $q_t$ | Cone resistance |
| $R_d$ | Relative density |
| $S_d$ | Slope of unloading curve in logarithmic plot |

| | |
|---|---|
| $\epsilon_c$ | Tensile hoop strain at pressuremeter surface |
| $\epsilon_{cm}$ | Maximum tensile hoop strain at pressuremeter surface |
| $\nu$ | Angle of dilation |
| $\phi$ | Peak angle of friction in plane strain |
| $\phi_{cv}$ | Angle of friction at constant volume |
| $p$ | Pressuremeter pressure |
| $p_l$ | Pressuremeter limit pressure |
| $p_l^m$ | Measured pressuremeter limit pressure |
| $p_l^n$ | Calculated pressuremeter limit pressure |

## Chapter 5

| | |
|---|---|
| $a_i$ | Coordinate vector |
| $\mathbf{a_m^e}, \mathbf{a^e}$ | Nodal velocity vectors |
| $\mathbf{b}$ | Body force vector |
| $\mathbf{B}, \mathbf{B_n}$ | Matrices relating nodal velocity and strain rate vector |
| $\mathbf{C}, \mathbf{C^n}$ | Distortion rate matrices |
| $d_{ij}$ | Rate of deformation tensor |
| $[D]^e$ | Elastic material matrix |
| $[D]^p$ | Plastic material matrix |
| $[D]^{ep}$ | Elastic-plastic material matrix |
| $\dot{e}_{ij}$ | Deviatoric strain rate |
| $E_{ij}$ | Green-Lagrange strain |
| $I_1, I_2, I_3$ | Stress invariants |
| $\mathbf{K}, \mathbf{K_n}$ | Element stiffness matrices |
| $m_e$ | Number of d.o.f. per element |
| $\mathbf{N}, \mathbf{N_n}$ | Shape function matrices |
| $\mathbf{P_m^e}, \mathbf{P^e}$ | Nodal forces vectors |
| $(r, z)$ | Original coordinate space |
| $(R, z)$ | Generalized coordinate space |

| | |
|---|---|
| $\dot{R}$ | Jaumann rotation matrix |
| $s_{ups}$ | Plane strain undrained shear strength |
| $s_{utc}$ | Triaxial undrained shear strength |
| $\dot{S}_{ij}$ | Deviatoric Cauchy stress rate |
| $\hat{S}_{ij}$ | Deviatoric Jaumann stress rate |
| $t, T_0, T$ | Time |
| $u_i$ | Deformation tensor |
| $\mathbf{u_m}, \mathbf{u}$ | Velocity field vectors |
| $\dot{v}$ | Volumetric strain rate |
| $x_i$ | Coordinate vector |
| $\delta_{ij}$ | Kronecker delta |
| $\hat{\sigma_{ij}}$ | Jaumann stress rate |
| $\dot{\sigma_{ij}}$ | Cauchy stress rate |
| $\dot{\omega_{ij}}$ | Skew-symmetric spin tensor |
| $\theta_i^e$ | Internal angle for node $i$ of element $e$ |
| $(\alpha, \beta)$ | Local (area) coordinate space |
| $\dot{\epsilon_{ij}}$ | Strain rate |
| $\phi_{ps}$ | Plane strain friction angle |
| $\phi_{tc}$ | Triaxial compression friction angle |
| $\psi_{ps}$ | Plane strain dilation angle |
| $\psi_{tc}$ | Triaxial compression dilation angle |

## Chapter 6

| | |
|---|---|
| $a, b$ | Inner and outer radius of the cylinder |
| $B$ | Radius of the footing |
| $G^{\infty}$ | Derived shear modulus from the cone-pressuremeter test with $\frac{L}{D} = \infty$ |
| $G^{10}$ | Derived shear modulus from the cone-pressuremeter test with $\frac{L}{D} = 10$ |

| | |
|---|---|
| $G^c, \nu^c$ | Shear modulus and Poisson's ratio of the correcting layer |
| $G, \nu$ | Shear modulus and Poisson's ratio of the continuum |
| $I_r$ | Rigidity index |
| $I_s$ | Stiffness index |
| $P_0$ | Initial hydrostatic pressure |
| $P$ | Applied total internal pressure |
| $\frac{L}{D}$ | Length to diameter ratio of the pressuremeter |
| $(S^n_{dc6}, \phi^n_{dc6})$ | Derived loading slope and friction angle from the pressuremeter test with $\frac{L}{D} = 6$ using central strain measurement |
| $(S^n_{dv6}, \phi^n_{dv6})$ | Derived loading slope and friction angle from the pressuremeter test with $\frac{L}{D} = 6$ using volumetric strain measurement |
| $(S^n_{dc\infty}, \phi^n_{dc\infty})$ | Derived loading slope and friction angle from the pressuremeter test with $\frac{L}{D} = \infty$ using central strain measurement |
| $(S^n_{dv\infty}, \phi^n_{dv\infty})$ | Derived loading slope and friction angle from the pressuremeter test with $\frac{L}{D} = \infty$ using volumetric strain measurement |
| $(S^{te}_{d\infty}, \phi^{te}_{d\infty})$ | Derived loading slope and friction angle from an exact cavity expansion curve which takes into account of elastic compressibility in plastic zone |
| $(S^{ta}_{d\infty}, \phi^{ta}_{d\infty})$ | Derived loading slope and friction angle from an approximate cavity expansion curve which ignores elastic compressibility in plastic zone |
| $s_u$ | Undrained shear strength |
| $s^l_{uv}$ | Undrained shear strength derived from the Menard limit pressure using volumetric strain measurement |
| $s^l_{uc}$ | Undrained shear strength derived from the Menard limit pressure using central strain measurement |

| | |
|---|---|
| $s_{ur}$ | Undrained shear strength derived from the expansion slope using volumetric strain measurement |
| $s_{uc}$ | Undrained shear strength derived from the expansion slope using central strain measurement |
| $s_{utc}$ | Triaxial compression undrained shear strength |
| $s_u^{\infty}$ | Derived undrained shear strength from the cone-pressuremeter test with $\frac{L}{D} = \infty$ |
| $s_u^{10}$ | Derived undrained shear strength from the cone-pressuremeter test with $\frac{L}{D} = 10$ |
| $\phi_{ps}$ | Plane strain friction angle |
| $\psi$ | Applied pressuremeter pressure |
| $\psi_{lm}$ | Menard pressuremeter limit pressure |
| $\epsilon_c$ | Central strain of the pressuremeter membrane |
| $\epsilon_{cm}$ | Maximum central strain of the membrane |
| $\phi_{cv}$ | Critial state friction angle |
| $\sigma_{h0}^{\infty}$ | Derived in-situ total horizontal stress from the cone-pressuremeter test with $\frac{L}{D} = \infty$ |
| $\sigma_{h0}^{10}$ | Derived in-situ total horizontal stress from the cone-pressuremeter test with $\frac{L}{D} = 10$ |

# Contents

# Chapter 1

# Introduction

## 1.1 Background

Site investigation and assessment of the characteristics of soil or rock are essential parts of the geotechnical design process. The principal parameters of interest to designers are strength, deformation moduli, in-situ horizontal stress and permeability. In-situ testing to complement laboratory tests in obtaining these fundamental soil properties is becoming increasingly important in practice. It is always good practice to undertake different types of test in order to obtain as broad a view as possible of the geotechnical properties of the strata being considered. Demand for in-situ testing has developed with a growing appreciation of the inadequacy of conventional laboratory testing. Inevitable sample disturbance affects laboratory test results and raises questions as to the validity of the soil strength and deformation properties measured. As was reported by Marsland(1973), work at the Building Research Station has shown that, for example, the actual deformation moduli of the ground may be several times greater than those measured in good quality tests in the laboratory on good quality samples. Consequently predictions of the deformation of the ground around a foundation based on laboratory data may be grossly overestimated, and the resulting design could be unnecessarily conservative and expensive. Another important advantage of in-situ testing is that the soil in question will be tested at the relevant level of effective stress, presuming that disturbance of the ground due to insertion of the instrument has been kept to a minimum. However, in-situ testing

generally involves more complex boundary conditions, and less control over stress path, than conventional laboratory testing, and therefore considerable difficulities exist for the interpretation of in-situ test data (see, for example, Wroth, 1984; Wroth, 1988).

The reason for the rapid development and wide use of the self-boring pressuremeter as a site investigation tool is that, in theory, the boundary conditions are relatively well defined, as are the stress and strain conditions in the surrounding soil mass (Wroth and Hughes, 1973). The basis of the test is the expansion of a long cylindrical membrane installed in the ground with the minimum of disturbance using the self-boring technique. In-situ strength and deformation properties of the ground can then be deduced from the measurements of the pressure and the change in volume or radius of the expanding membrane using cavity expansion theory. In doing this, some simplifying assumptions about the boundary conditions and soil stress-strain behaviour may need to be made.

As an alternative to the self-boring pressuremeter, the cone-pressuremeter is a new in-situ testing device which combines a $60^0$ electric piezocone with the pressuremeter test. The full development of the cone-pressuremeter test, however, is subject to the rational theoretical modelling of initial installation of the full displacement pressuremeter in both undrained and drained soils. Although the Strain Path Method (Baligh, 1985; Tumay et al., 1985) has proved to be a successful method in modelling steady cone penetration in undrained soils, it is not yet possible to apply this approach to deep foundation problems in drained soils. Teh (1987) has implemented the Strain Path Method for the analysis of the $60^0$ cone and found that the stresses calculated using the Strain Path Method do not fully satisfy equilibrium. This failure is reflected in the dependence of the octahedral mean stress on the integration path. On the other hand, it can be shown theoretically that cylindrical cavity expansion theory models correctly the penetration of a cone with a small tip angle, but is only approximate for the $60^0$ cone tip (Norbury and Wheeler, 1987). In addition, Teh's analysis shows that the stress distribution far behind the cone tip is very close to the distribution created by the expansion of a cylindrical cavity from zero radius followed by a small amount of contraction. The use of large strain cylindrical cavity expansion or contraction theory for the interpretation of cone-pressuremeter tests in both clays and sands is justified provided that the bottom of the pressuremeter section

is located far enough behind the cone tip.

In the analysis of cavity expansion or contraction, only in special cases has it been possible to solve the problem analytically and so a numerical treatment has often been used, particularly when more realistic constitutive models and boundary conditions have been employed.

## 1.2 Interpretation of pressuremeter tests

### 1.2.1 Self-boring pressuremeter tests

#### Pressuremeter tests in clay

The development of the self-boring pressuremeter test allowed the pressuremeter to be inserted into the ground with minimum soil disturbance. The pressuremeter test simulates the expansion of a cylindrical cavity and because it has well defined boundary conditions, it is more amenable to rigorous theoretical analysis (i.e. cavity expansion theory) than most other in-situ tests.

For an elastic-perfectly plastic undrained soil with a Tresca plastic model, an exact solution for the relation between cavity pressure and cavity strain was first derived by Gibson and Anderson (1961) using large strain analysis in the plastic zone and small strain analysis in the elastic zone.

As the cavity pressure is increased, the response is initially elastic with small strains. Once the cavity pressure is increased above the yield value, an expanding annulus of plastic soil develops around the cavity while clay further away from the cavity continues to respond elastically. During the plastic phase, we have:

$$P = P_l + s_u \ln[1 - (\epsilon_c + 1)^{-2}] \tag{1}$$

where $P$ and $\epsilon_c$ denote the cavity pressure and cavity strain respectively and the limit pressure $P_l$ can be written as follows:

$$P_l = \sigma_{h0} + s_u[1 - \ln I_r] \tag{2}$$

in which

$$I_r = \frac{G}{s_u} \tag{3}$$

where $\sigma_{h0}, s_u$ and $I_r$ denote the initial in-situ horizontal stress, undrained shear strength and rigidity index, respectively. Having used the above analysis, the stiffness and undrained shear strength for clay can be deduced from the cavity pressure-cavity strain relationship obtained from pressuremeter tests. Palmer (1972) presented an alternative method of analysis in which the precise form of shear stress-shear strain curve can be deduced from the measured pressure-strain relationship. The exact expression for the shear stress, $\tau$, at a cavity strain $\epsilon_c$ in undrained clay is:

$$\tau = \frac{1}{2}\epsilon_c(1 - \epsilon_c)(2 - \epsilon_c)\frac{\partial P}{\partial \epsilon_c} \tag{4}$$

The Gibson and Anderson and the Palmer analyses are in no way contradictory. Each of them can be used for different purposes.

### Pressuremeter tests in sand

The interpretation of pressuremeter tests in sand is complicated by the fact that all tests are drained tests, and volume changes in the sand around the expanding cavity are able to occur freely. Therefore, any reliable analysis has to take account of the effects of volume change during the test. The most widely used method of interpretation is based on the analysis presented by Hughes et al.(1977) assuming that the pressuremeter is long enough for the test to be simulated by the expansion of a cylindrical cavity. Their analysis is summarised here.

Hughes et al. described a model in which the sand is assumed to be isotropic linear elastic until yield occurs when the Mohr-Coulomb condition is satisfied. The material then flows plastically at a constant angle of dilation. The elastic deformation in plastic zones is assumed to be small compared with the plastic strain component and is therefore ignored in the analysis for simplicity. The stress-dilatancy flow rule of Rowe (1962) was used to relate the ratio of moblised friction angle and dilation angle in terms of the angle of friction at constant volume (i.e. critical state friction angle).

With these assumptions about the behaviour of the sand, plasticity is initiated at the wall of the cavity when

$$P - u_0 = \sigma'_{h0}(1 + \sin\phi') \tag{5}$$

Once plasticity has been initiated, small strain cavity expansion theory can be used to give the following relationship between the cavity pressure and cavity strain,

$$\ln(P - u_0) = S_d \ln(\epsilon_c + \frac{c}{2}) + A \tag{6}$$

where

$$S_d = \frac{(1 - \sin\psi)}{(1 - \sin\phi')} \sin\phi' \tag{7}$$

and $u_0, \sigma'_{h0}$ denote the in-situ pore pressure and the in-situ horizontal effective stress; $A$ and $c$ are constants; $\phi', \psi$ denote the effective mobilised angle of friction and mobilised dilation angle.

By using Rowe's stress-dilatancy flow rule, we can deduce $\psi$ and $\phi'$ from the value of the pressuremeter loading slope $S_d$ as follows:

$$\sin\phi' = \frac{(K + 1)S_d}{(K - 1)S_d + 2} \tag{8}$$

$$\sin\psi = \frac{2KS_d - (K - 1)}{K + 1} \tag{9}$$

and

$$K = \frac{1 + \sin\phi'_{cv}}{1 - \sin\phi'_{cv}} \tag{10}$$

where $\phi'_{cv}$ denotes the angle of friction at constant volume.

A new method of analysis related to the cavity contraction phase of the pressuremeter test has been presented by Houlsby et al.(1986), based on the same soil model as described above. The data may be obtained from a loading stage as well as from an unloading stage. The key advantage of the unloading analysis is that the method is less sensitive to any initial disturbance caused by the installation of the pressuremeter. It could therefore be

expected that for the cone-pressuremeter test an unloading analysis will be more useful than a loading analysis.

Recently an analogous analysis to Palmer's for the pressuremeter test in sand has been developed by Manassero (1989), in which a flow rule such as the stress-dilatancy expression of Rowe (1962) is adopted. This analysis allows a stress ratio-shear strain relationship to be derived from a pressuremeter test in a drained material.

### 1.2.2 Cone-pressuremeter tests

#### Cone-pressuremeter tests in clay

The cone-pressuremeter is an in-situ testing device which shows clear promise for the rapid measurement of undrained strength and shear stiffness. An analysis for full displacement pressuremeter tests in undrained clay soil has recently been presented by Houlsby and Withers (1988) using a large strain cavity expansion and contraction theory.

The main conclusion of their analysis is that some soil properties can be deduced from measured plastic unloading curves. The analysis of the loading phase is similar to that derived by Gibson and Anderson (1961). In the Houlsby and Withers analysis, the following plastic unloading curve for Tresca soil was derived :

$$P = P_l - \frac{2(2-m)}{3} s_u \{1 - \ln[\sinh \frac{m+1}{2}(\epsilon_{cm} - \epsilon_c)] - \ln[\sinh \frac{1}{I_r}]\} \tag{11}$$

where

$$m = \begin{cases} 1 & \text{for cylindrical cavity} \\ 2 & \text{for spherical cavity} \end{cases} \tag{12}$$

and $P_l, I_r$ denote the cavity limit pressure and rigidity index of clay; P is the cavity pressure; $\epsilon_c$ and $\epsilon_{cm}$ denote cavity strain and maximum cavity strain.

The above equation implies that the slope of the plastic unloading curve, when it is plotted as P against $-\ln[\frac{m+1}{2}(\epsilon_{cm} - \epsilon_c)]$, is approximately $\frac{2(2+m)}{3} s_u$. In addition, the shear modulus and in-situ horizontal stress can be obtained from the measured loading and unloading curves. The derived stiffness and strength parameters using cylindrical cavity contraction theory are found to be in good agreement with some other measurements. The

failure of using their analysis in obtaining realistic in-situ horizontal stresses indicates, however, that further research is needed in order to obtain reliable horizontal stress using the cone-pressuremeter.

### Cone-pressuremeter tests in sand

The first attempt to improve the understanding of the cone-pressuremeter tests in sands by determining the stress path followed by the tests was presented by Hughes and Robertson (1985). They found that the elastic shear moduli from cone-pressuremeter tests show remarkable agreement with the values obtained from self-boring pressuremeter tests. This means that the elastic shear modulus obtained by performing an unloading-reloading cycle during a pressuremeter expansion test is insensitive to the method of installation.

In addition, results comparing cone-pressuremeter tests and the self-boring pressuremeter tests suggest that in sands the lift-off pressure obtained from the cone-pressuremeter is probably of the same order of magnitude as the initial in-situ horizontal stress. However, calibration chamber tests by Schnaid (1990) have shown a very poor relationship between the lift-off pressure and the applied lateral boundary stress.

Because of the large initial disturbance caused by the installation of the cone pressuremeter, application of the small strain analysis presented by Hughes et al.(1977) to the cone-pressuremeter tests for a radial displacement of up to 10 %, gives unacceptably high values of friction angle. A similar finding has also been reported by Withers et al.(1989) based on field test results and Schnaid (1990) using the chamber tests. This evidence suggests that it is necessary to use a large strain analysis to interpret the full displacement pressuremeter test in sand, which requires a significant development of the closed form solution for large strain cavity expansion or contraction in dilatant materials.

## 1.3 Objectives of the investigation

As mentioned above, there is an urgent need to conduct further research into the development of the closed form solution for large strain cavity expansion or contraction in

dilatant materials, in order to provide a theoretical basis for interpretation of the cone-pressuremeter test in sand. Any further development of the cone-pressuremeter test may, to some extent, depend on the availability of a rational method of interpretation. The first objective of the work described in this thesis is to develop a closed form solution for large strain cavity expansion or contraction in soils with dilation.

Since the development of the self-boring pressuremeter, the pressuremeter test has become a frequently used method of deriving strength and stiffness parameters for both clay and sand. The method of deriving both stiffness and undrained shear strength proposed by Gibson and Anderson (1961) and the method of estimating friction angle and dilation angle developed by Hughes et al.(1977) have been widely used to interpret the results of self-boring pressuremeter tests in clay and sand respectively. However, the values obtained from the pressuremeter test are consistently higher than those traditionally used in design or obtained from other measurements. The high values of strength and deformation parameters obtained from pressuremeter tests may be partly due to the lower disturbance associated with the pressuremeter as compared with laboratory tests. Consistently high strength parameters obtained from the pressuremeter test may also be related to the validity of the assumption that the expansion of the pressuremeter is identical with that of an infinitely long cavity; i.e. that the effects of the finite length to diameter ratio can be neglected in the analysis. In addition, the failure of cavity expansion theory to allow derivation of realistic in-situ horizontal stress values from the cone-pressuremeter test may be largely explained by the finite length of the pressuremeter. It is therefore appropriate to re-evaluate some of the assumptions on which the methods of interpretation are based. Starting from this basis, the extension and development of the methods for interpretation of both self-boring pressuremeter test and the cone-pressuremeter test to deal with the effects of finite length of probe on derived parameters, and the effects of finite boundary of laboratory calibration chamber on observed pressuremeter behaviour, is the second objective of the research.

In order to achieve the second objective, a finite element analysis was adopted. It is well accepted, however, that severe numerical difficulities arise when using the conventional displacement finite element to analyse soils because of incompressibility constraints

(Sloan, 1981). This effect is caused by a conflict between the plastic flow rule and the finite element discretization. Although several approaches have been proposed to deal with this difficulty, none of these have proved to be wholly satisfactory. It is the third objective of the research presented in this thesis to develop a rational large strain displacement type finite element for modelling soil behaviour under axisymmetric loading conditions.

# Chapter 2

# Finite Cavity Expansion and Contraction in Dilatant Materials

## 2.1 Introduction

Cavity expansion theory was first developed for application to metal indentation problems (Bishop, Hill and Mott, 1945; Hill, 1950). The application of cavity expansion theory to geotechnical problems came later (e.g. Gibson and Anderson, 1961; Meyerhof, 1951) and has been progressively refined in the last two decades. The analysis of a cylindrical cavity has been applied to practical problems such as the interpretation of pressuremeter tests (Gibson and Anderson, 1961; Ladanyi, 1963; Ladanyi, 1972; Palmer, 1972; Hughes, Wroth and Windle, 1977; Houlsby, Clarke and Wroth, 1986; Houlsby and Withers, 1988) because the pressure-expansion curve obtained in a pressuremeter test directly reflects some properties of the soil stress-strain relationship. A detailed study of the application of cylindrical cavity expansion in modelling the installation of driven piles was given by Randolph and Wroth (1979) and Randolph, Carter and Wroth (1979). The effect of longitudinal shaft friction in a cylindrical expanding cavity, which is important for application to pile bearing capacity analysis, has also been considered recently (Sagaseta, 1984). It should be noted that all the analytical studies mentioned above are either large strain analysis in an incompressible soil or small strain analysis in a dilatant soil. The large strain cavity expansion problem in dilatant soil is therefore generally solved

by a finite element method (e.g. Carter and Yeung, 1985). However, it is well accepted that severe numerical difficulties arise when using the finite element method to analyse constrained problems (e.g. incompressible and dilatant solids). Hence care must be taken when using the conventional finite element approach to model elastic-plastic soil behaviour. A comprehensive study of the numerical difficulties in using the conventional finite element method to model elastic-plastic deformation involving incompressibility and dilatancy will be given in Chapter 3 and Chapter 5.

As far as the spherical cavity problem is concerned , some solutions have been obtained for cavities in various types of materials. Hill (1950) gave a general solution of the finite expansion of the spherical cavity by using the Tresca yield function. Later Chadwick (1959) presented a more comprehensive solution for the expansion of a spherical cavity in an elastic-plastic material obeying the associated Mohr-Coulomb flow rule. The closed form limit pressure for the special case of a purely cohesive incompressible material was also presented in the same paper. However, it is believed that the derivation of unloading solution in the paper is not fully correct. This is due to the fact that the parameter $\kappa$ defined in equation (60) of the paper could well be negative for a material with a high dilation angle. Hence the solution of equation (60) in the paper may become undefined. Vesic (1972) extended the analysis to compressible soils by assuming that the soil volumetric strain is not zero but a finite value and presented an approximate solution for limit pressure for spherical cavity expansion. He applied this solution to the determination of bearing capacity factors for deep foundations. More recently, Carter, Booker and Yeung (1986) presented an analytical solution for limit pressures for cavity expansion in a non-associated Mohr-Coulomb material by assuming that a pseudo steady state deformation is approached at a very large deformation. It is the author's opinion that this assumption is not fully justified and the limit pressure solution presented in their paper can only be treated as an approximate solution. The important role of the elastic deformations in the plastic zone for the cavity expansion problem is emphasised by Bigoni and Laudiero (1989) using numerical (Gaussian) integration. In their paper, a similar approach to Chadwick's is used and the non-associated Mohr-Coulomb criterion is adopted. The longitudinal normal stress is assumed to coincide with the mean of the

other two principal stresses for the case of the cylindrical cavity. However, it is believed that they made an assumption about the stress and strain condition in the axial direction which results in a violation of the plastic flow rule.

In this chapter, a unified analytical solution is presented for the expansion of both cylindrical and spherical cavities in dilatant elastic-plastic soils by using the Mohr-Coulomb yield criterion with a non-associated flow rule. For the case of cylindrical cavity expansion, the axial (or vertical) stress is assumed to be the intermediate stress and the assumption of plane strain conditions in the axial direction has been made. An explicit expression for the pressure-expansion relation is derived without any restriction being imposed on the magnitude of the deformations. This is achieved by integrating the governing equation with the aid of a series expansion. Consequently, the limit cavity pressure when the radius of the cavity approaches infinity can be determined analytically with no additional assumption being made about the deformation mode. In addition, closed form solutions for residual stress and displacement distributions are obtained at any stage of the unloading process. For the unloading analysis the problem, which was found in the paper of Chadwick (1959), has been avoided by adopting a new means of transformation for integration variables in forming the displacement governing equation in the plastic zone.

## 2.2 Definition of the problem

An unbounded three-dimensional medium of dilatant soil contains a single cylindrical or spherical cavity. Initially the radius of the cavity is $a_0$ and a hydrostatic pressure $p_0$ acts throughout the soil which is assumed to be homogeneous. An additional pressure $p$ is then applied inside the cavity and increased sufficiently slowly for dynamic effects to be negligible. The major concern of this chapter is the distribution of stress and displacement in the soil as the additional pressure $p$ increases from zero and when removal of this pressure subsequently takes place.

The soil is modelled as an isotropic dilatant elastic-perfectly plastic material. It behaves elastically and obeys Hooke's law until the onset of yielding which is determined

by the Mohr-Coulomb criterion. When the principal stress components satisfy the inequalities $\sigma_i \leq \sigma_j \leq \sigma_k$, the Mohr-Coulomb yield function takes the form

$$\alpha\sigma_k - \sigma_i = Y \tag{13}$$

where

$$\alpha = \frac{1 + \sin\phi}{1 - \sin\phi} \tag{14}$$

$$Y = \frac{2c\cos\phi}{1 - \sin\phi} \tag{15}$$

in which $c$ and $\phi$ denote the cohesion and friction angle of the soil respectively.

The solutions for the cylindrical cavity and the spherical cavity can be developed together by defining

$$m = \begin{cases} 1 & \text{for cylindrical cavity} \\ 2 & \text{for spherical cavity} \end{cases} \tag{16}$$

The initial position of a particle of soil is specified by spherical polar coordinates $(r_0, \theta, \omega)$ for a spherical cavity and by cylindrical polar coordinates $(r_0, \theta, z)$ for a cylindrical cavity. Plane strain conditions in the $z$ direction are assumed for the cylindrical cavity. In addition, the vertical stress $\sigma_z$ is assumed to be the intermediate principal stress and therefore there is no component of plastic strain in the vertical direction. These two assumptions are sufficient for determining the vertical stress as long as the other two stress components are known. This can be achieved simply by calculating the increase in $\sigma_z$ in both elastic and plastic zones from the following equation:

$$\dot{\sigma}_z = \nu(\dot{\sigma}_r + \dot{\sigma}_\theta) \tag{17}$$

where $\nu$ denotes Poisson's ratio. The implication of these two assumptions will be discussed at length later.

Before any additional pressure is applied within the cavity wall ($t = 0$), the cavity has a radius $a_0$ and an internal pressure $p_0$. At time $t$ after application of additional pressure

$p$, the cavity radius increases to $a$. A typical material point now has moved to radius $r$ from $r_0$.

At the current position, the total stress must be in equilibrium with the current boundary traction. Because of symmetry, this requirement can be expressed as

$$\sigma_\theta = \sigma_r - \frac{r}{m}\frac{\partial \sigma_r}{\partial r} \tag{18}$$

subject to the two general boundary conditions:

$$\sigma_r(a) = -p - p_0 \tag{19}$$

$$\lim_{r \to \infty} \sigma_r = -p_0 \tag{20}$$

noting that the notation of tension positive is used in this thesis.

The displacement defined by

$$u = r - r_0 \tag{21}$$

is purely radial and Young's modulus $E$ and Poisson's ratio $\nu$ are used to define the elastic behaviour of the soil. As soils are characterized by the strong inequality $Y \ll E$ for both total stress undrained analysis and effective stress drained analysis, the use of the small strain theory throughout the initial phase of elastic deformation is justified provided that $p_0 \ll E$ because the strain to the initiation of plasticity is then small. A combination of a large strain analysis in the plastic region and a small strain solution in the elastic region is adopted in this chapter.

## 2.3 Elastic response

As the applied pressure $p$ increases from zero, the deformation of the soil at first is purely elastic. Under conditions of radial symmetry the elastic stress-strain relationship may be expressed as:

$$\dot{\epsilon_r} = \frac{\partial \dot{u}}{\partial r} = \frac{1 - \nu^2(2-m)}{E}\{\dot{\sigma_r} - \frac{m\nu}{1-\nu(2-m)}\dot{\sigma_\theta}\} \tag{22}$$

$$\dot{\epsilon}_\theta = \dot{\epsilon}_z = \frac{\dot{u}}{r} = \frac{1-\nu^2(2-m)}{E}\{-\frac{\nu}{1-\nu(2-m)}\dot{\sigma}_r - [1-\nu(m-1)]\dot{\sigma}_\theta\} \tag{23}$$

where the vertical strain for a cylindrical cavity is assumed to be zero.

The solution of equations ( 22),( 23) and ( 18) subject to the boundary conditions ( 19) and ( 20) can be easily shown to be:

$$\sigma_r = -p_0 - p(\frac{a}{r})^{m-1} \tag{24}$$

$$\sigma_\theta = -p_0 + \frac{p}{m}(\frac{a}{r})^{m+1} \tag{25}$$

$$u = \frac{p}{2mG}(\frac{a}{r})^{m+1}r \tag{26}$$

where $G$ denotes the shear modulus.

Since a compressive negative notation is used, the yield equation takes the form:

$$\alpha\sigma_\theta - \sigma_r = Y \tag{27}$$

As the pressure $p$ increases further, an initial yielding starts at the cavity wall when the following condition is satisfied:

$$p = p_1 = \frac{m(Y + (\alpha-1)p_0)}{m-\alpha} \tag{28}$$

The consistency of the stress and strain assumptions in the axial direction used for the expansion of a cylindrical cavity is discussed now. The assumption of plane strain conditions and the intermediacy of $\sigma_z$ results in two relationships between stresses in the plastic zone. They are defined by equation ( 17) and equation ( 27). Before the soil becomes plastic, the radial stress decreases while the hoop stress increases and the vertical stress remains unchanged. Once the soil deforms plastically, all three stresses start to decrease. The relative magnitude of the decrease in each stress can easily be derived from equation ( 17) and equation ( 27) as follows:

$$\frac{\dot{\sigma}_z}{\dot{\sigma}_r} = \frac{2\nu}{1+\sin\phi} \geq 0 \tag{29}$$

$$\frac{\dot{\sigma}_\theta}{\dot{\sigma}_r} = \frac{1-\sin\phi}{1+\sin\phi} \geq 0 \tag{30}$$

From the above two equations, we can conclude that the sufficient condition for $\sigma_z$ to remain as the intermediate stress is

$$\frac{\dot{\sigma}_z}{\dot{\sigma}_r} \geq \frac{\dot{\sigma}_\theta}{\dot{\sigma}_r} \tag{31}$$

which can be further simplified to:

$$2\nu \geq 1 - \sin\phi \tag{32}$$

The condition defined by equation (32) breaks down only when both Poisson's ratio and friction angle of a soil are rather small. Even if this condition is violated, then the assumption that the axial stress remains intermediate may still be valid throughout the analysis, since, even though $\sigma_z$ is approaching $\sigma_\theta$, it may not reach it before the end of the analysis is reached. This has been proved by looking at the stress distributions when the cavity limit pressure is reached.

## 2.4 Elastic-plastic response : stress analysis

After an initial yielding takes place at the cavity wall, a plastic zone within the region $a \leq r \leq b$ is formed around the inner wall of the cavity with the increase of the applied pressure $p$. We now consider the plastic and elastic regions of the soil separately.

**The plastic region,** $a \leq r \leq b$

The stress components which satisfy the equilibrium equation ( 18) and yield condition ( 27) can be found to be:

$$\sigma_r = \frac{Y}{\alpha - 1} + Ar^{-\frac{m(\alpha-1)}{\alpha}} \tag{33}$$

$$\sigma_\theta = \frac{Y}{\alpha - 1} + \frac{A}{\alpha} r^{-\frac{m(\alpha-1)}{\alpha}} \tag{34}$$

where $A$ is a constant of integration.

**The elastic region,** $r \geq b$

The stress components in the elastic zone may be obtained from equations ( 18)-( 20) and ( 22), ( 23) as follows:

$$\sigma_r = -p_0 - Br^{-(1+m)} \tag{35}$$

$$\sigma_\theta = -p_0 - \frac{1}{m} Br^{-(1-m)} \tag{36}$$

where $B$ is a second constant.

The continuity of stress components at the elastic-plastic interface can be used to determine the constants $A$ and $B$ in terms of the interface radius $b$:

$$A = -\frac{(1-m)\alpha(Y - (\alpha-1)p_0)}{(\alpha-1)(m-\alpha)} b^{\frac{m(\alpha-1)}{\alpha}} \tag{37}$$

$$B = \frac{m(Y - (\alpha-1)p_0)}{m-\alpha} b^{1-m} \tag{38}$$

Combining equations ( 19) and ( 33) allows the elastic-plastic interface radius to be expressed in terms of the cavity pressure ratio $\sigma_R$ and the current cavity radius $a$:

$$\frac{b}{a} = (\sigma_R)^{\frac{\alpha}{m(\alpha-1)}} \tag{39}$$

where the cavity pressure ratio $\sigma_R$ is defined by:

$$\sigma_R = \frac{(m+\alpha)(Y + (\alpha-1)(p - p_0))}{\alpha(1-m)(Y + (\alpha-1)p_0)} \tag{40}$$

The relationship between the stress distribution and the elastic-plastic interface radius in the soil has now been established. Once the elastic-plastic interface radius is known, the stress can be determined using the expressions developed in this section.

## 2.5 Elastic-plastic response : displacement analysis

As we know, the results obtained above cannot be used to calculate the distribution of stress until the displacement field is known. On substituting from equations ( 35),( 36),( 38) into ( 23) the displacement in the elastic zone, $r \geq b$, can be shown to be :

$$u = \frac{(Y - (\alpha - 1)p_0)}{2(m - \alpha)G}(\frac{b}{r})^{1-m}r \tag{41}$$

The determination of displacement field in the plastic zone requires the use of a plastic flow rule which indicates the relative magnitude of plastic strains in different directions. It is assumed that while yield is occurring, the total strain is decomposed additively into elastic and plastic components. Indices $\epsilon, p$ are used to distinguish the elastic and plastic components of the total strains. Following Davis (1969), the soil is assumed to dilate plastically at a constant rate. The non-associated flow rule combined with the Mohr-Coulomb yield criterion has been well established for modelling soil behaviour with dilation. For the phase of loading in cavity expansion, the non-associated flow rule may be expressed as:

$$\frac{\dot{\epsilon}_r^p}{\dot{\epsilon}_\theta^p} = -\frac{m}{\beta} \tag{42}$$

where

$$\beta = \frac{1 + \sin\psi}{1 - \sin\psi} \tag{43}$$

in which $\psi$ denotes the angle of dilation for the soil.

Substituting equations ( 22),( 23) into the plastic flow rule defined by equation ( 42) results in:

$$\begin{aligned} \beta\dot{\epsilon}_r + m\dot{\epsilon}_\theta &= \frac{1 - \nu^2(2 - m)}{E}\{[\beta - \frac{m\nu}{1 - \nu(2 - m)}]\dot{\sigma}_r \\ &\quad + [m - \nu m^2 + m\nu - \frac{m\beta\nu}{1 - \nu(2 - m)}]\dot{\sigma}_\theta\} \end{aligned} \tag{44}$$

The distributions of stress and strain in the soil at the initiation of plastic yield are obtained from equations ( 22)-( 26) by putting $p = p_1$. The integral of equation ( 44) subject to these conditions is found to be:

$$\beta\epsilon_r + m\epsilon_\theta = \frac{1 - \nu^2(2 - m)}{E}\{[\beta - \frac{m\nu}{1 - \nu(2 - m)}]\sigma_r$$

$$-[m-\nu m^2-m\nu-\frac{\beta m\nu}{1-\nu(2-m)}]\sigma_\theta$$
$$-[\beta-m-m\nu-m^2\nu-\frac{m\nu(1-\beta)}{1-\nu(2-m)}]p_0\} \tag{45}$$

In order to account for effects of large strain in the plastic zone, the logarithmic strain is adopted, namely

$$\epsilon_r=\ln(\frac{dr}{dr_0}) \tag{46}$$
$$\epsilon_\theta=\ln\frac{r}{r_0} \tag{47}$$

Substituting equations ( 46),( 47) and ( 33), ( 34),( 37) into equation ( 45) leads to:

$$\ln[(\frac{r}{r_0})^{\frac{m}{\beta}}\frac{dr}{dr_0}]=\ln\eta-\Omega(\frac{b}{r})^{\frac{m(\alpha-1)}{\alpha}} \tag{48}$$

where

$$\eta=exp\{\frac{(\beta+m)(1-2\nu)(Y+(\alpha-1)p_0)[1+(2-m)\nu]}{E(\alpha-1)\beta}\} \tag{49}$$

$$\Omega = \frac{[1-\nu^2(2-m)](1+m)(Y+(\alpha-1)p_0)}{E(\alpha-1)\beta(m-\alpha)}[\beta+m-m\nu$$
$$-m^2\nu+(\alpha-1)\beta-\frac{m\nu(\alpha-\beta)}{1-\nu(2-m)}] \tag{50}$$

By means of the transformation

$$\rho=(\frac{b}{r})^{\frac{m(\alpha-1)}{\alpha}} \tag{51}$$
$$\zeta=(\frac{r_0}{b})^{\frac{\beta+m}{\beta}} \tag{52}$$

and the use of equation ( 41), equation ( 48) can be integrated over the interval $[b,r]$, leading to:

$$\frac{m(\alpha-1)\beta\eta}{\alpha(\beta+m)}\{[1-\frac{(Y+(\alpha-1)p_0)}{2(m+\alpha)G}]^{\frac{\beta+m}{\beta}}-(\frac{r_0}{b})^{\frac{\beta+m}{\beta}}\} =$$
$$\int_1^{(\frac{b}{r})^{\frac{m(\alpha-1)}{\alpha}}}\epsilon^{\Omega\rho}\rho^{-\frac{\alpha(\beta+m)}{m(\alpha-1)\beta}-1}d\rho \tag{53}$$

By putting $r_0 = a_0, r = a$, and making use of equation ( 39), we have

$$\frac{m(\alpha-1)\beta\eta}{\alpha(\beta+m)}\{1-\frac{(Y-(\alpha-1)p_0)}{2(m-\alpha)G}[\frac{\beta+m}{\beta}-\sigma_R^{-\frac{\alpha(\beta+m)}{m(\alpha-1)\beta}}(\frac{a_0}{a})^{\frac{\beta+m}{\beta}}\} = \int_1^{\sigma_R}\epsilon^{\Omega\rho}\rho^{-\frac{\alpha(\beta+m)}{m(\alpha-1)\beta}-1}d\rho \tag{54}$$

For spherical cavity expansion in the associated Mohr-Coulomb material (i.e. $m = 2$ and $\beta = \alpha$) equation ( 54) reduces to the solution given by Chadwick (1959).

With the aid of the series expansion

$$\epsilon^{\Omega\rho} = \sum_{n=0}^{\infty}\frac{(\Omega\rho)^n}{n!} \tag{55}$$

the following explicit expression for the pressure-expansion relationship is obtained:

$$\frac{a}{a_0} = \{\frac{\sigma_R^{-\frac{\alpha(\beta+m)}{m(\alpha-1)\beta}}}{[1-\frac{(Y+(\alpha-1)p_0)}{2(m-\alpha)G}][\frac{\beta+m}{\beta}-\frac{\alpha(\beta-m)}{m(\alpha-1)\beta\eta}\Lambda_1(\sigma_R,\Omega)}\}^{\frac{\beta}{\beta+m}} \tag{56}$$

where

$$\Lambda_1(x,y) = \sum_{n=0}^{\infty}A_n^1 \tag{57}$$

in which

$$A_n^1 = \begin{cases} \frac{y^n}{n!}\ln x & \text{if } n = \frac{\alpha(\beta+m)}{m(\alpha-1)\beta} \\ \frac{y^n}{n![n-\frac{\alpha(\beta+m)}{m(\alpha-1)\beta}]}[x^{n-\frac{\alpha(\beta+m)}{m(\alpha-1)\beta}}-1] & \text{otherwise} \end{cases}$$

Having noted that $\Omega$ is a small value with an order $\frac{Y+(\alpha-1)p_0}{E}$, we can easily prove that the series defined by equation ( 57) converges very rapidly for all values of $\alpha, \beta$ of the soil. In general, the first few terms in the series may be used to give satisfactory results.

By putting $\frac{a}{a_0} \to \infty$, the limit applied pressure $p_\infty$ may be obtained from:

$$\Lambda_1(\sigma_{R\infty},\Omega) = \frac{m(\alpha-1)\beta\eta}{\alpha(\beta-m)}[1-\frac{(Y+(\alpha-1)p_0)}{2(m-\alpha)G}]^{\frac{\beta-m}{\beta}} \tag{58}$$

where

$$\sigma_{R\infty} = \frac{(m-\alpha)(Y+(\alpha-1)(p_\infty-p_0))}{\alpha(1-m)(Y+(\alpha-1)p_0)} \tag{59}$$

By contrast, it can be shown that the small strain assumption will lead to the following closed form expression for displacement in the plastic zone:

$$u = \frac{(Y+(\alpha-1)p_0)}{2(m-\alpha)G} - \frac{\alpha\beta\Omega}{m(\alpha-(\alpha-1)\beta)-\beta\alpha} - \frac{\beta\ln\eta}{\beta-m}\left(\frac{b}{r}\right)^{\frac{m}{\beta}}b - \frac{\beta\ln\eta}{\beta-m}r - \frac{\alpha\beta\Omega}{m(\alpha-(\alpha-1)\beta)+\beta\alpha}\left(\frac{b}{r}\right)^{\frac{m(\alpha-1)}{\alpha}}r \tag{60}$$

which is only applicable to the situation where the maximum value of the applied pressure is sufficiently small for the squares and higher power of strains included in the large strain definition ( 46)-( 47) to be negligible.

In addition, neglecting the elastic deformation in the plastic zone results in the relatively simple large strain pressure-expansion expression:

$$\sigma_R = \left\{\frac{1-\left(\frac{a_0}{a}\right)^{\frac{\beta+m}{\beta}}}{1-\left[1-\frac{(Y+(\alpha-1)p_0)}{2(m+\alpha)G}\right]\cdot\frac{\beta+m}{\beta}}\right\}^{\frac{m(\alpha-1)\beta}{\alpha(\beta+m)}} \tag{61}$$

The comparison between large strain solution equation ( 61) and the small strain solution given by Hughes,Wroth and Windle (1977) clearly indicates that effects of large strain in the plastic zone are closely related to the magnitude of deformations and dilatancy of the soil.

## 2.6 Elastic unloading and reverse yielding

Assuming that an elastic-plastic state of the soil around the cavity has been reached by monotonically increasing the applied pressure to the value $p$, the effect of monotonically reducing the pressure to the value $(1-x)p, 0 \leq x \leq (1+\frac{p_0}{p})$ is now considered. The restriction imposed on the value of $x$ allows us only to consider the case when all stress in the soil remains compressive. The configuration of the system on the completion of loading is used as a reference state from which the stress and displacement of the

unloading process are measured. Deviations from this state are denoted by a single prime and current values of field quantities by a double prime.

$$\sigma_r'' = \sigma_r + \sigma_r' \tag{62}$$

$$\sigma_\theta'' = \sigma_\theta - \sigma_\theta' \tag{63}$$

$$u'' = u + u' \tag{64}$$

As $x$ increases from zero, the soil at first unloads elastically. Superimposing upon the stress distribution at the completion of loading (see equations ( 33)-( 38)) an elastic stress field produced by the application of an additional pressure $-xp$ at the cavity wall. we find,

$$\sigma_r'' = \frac{Y}{\alpha - 1} - \frac{\alpha(1+m)(Y-(\alpha-1)p_0)}{(\alpha-1)(m+\alpha)}(\frac{b}{r})^{\frac{m(\alpha-1)}{\alpha}} - xp(\frac{a''}{r''})^{1+m} \tag{65}$$

$$\sigma_\theta'' = \frac{Y}{\alpha - 1} - \frac{(1+m)(Y-(\alpha-1)p_0)}{(\alpha-1)(m+\alpha)}(\frac{b}{r})^{\frac{m(\alpha-1)}{\alpha}} - \frac{1}{m}xp(\frac{a''}{r''})^{1+m} \tag{66}$$

for $a'' \leq r'' \leq b''$, and

$$\sigma_r'' = -p_0 - \frac{m(Y+(\alpha-1)p_0)}{m+\alpha}(\frac{b}{r})^{1+m} + xp(\frac{a''}{r''})^{1+m} \tag{67}$$

$$\sigma_\theta'' = -p_0 + \frac{Y+(\alpha-1)p_0}{m+\alpha}(\frac{b}{r})^{1+m} - \frac{1}{m}xp(\frac{a''}{r''})^{1+m} \tag{68}$$

for $r'' \geq b''$.

As $x$ increases, $\sigma_r''$ increases and $\sigma_\theta''$ decreases, the reverse yielding will commence when

$$\alpha\sigma_r'' - \sigma_\theta'' = Y \tag{69}$$

Recalling equations ( 65) and ( 66) it can be shown that this condition is first satisfied at the cavity wall $r'' = a''$ when $x = x_2$, where

$$x_2 = \frac{m(1-\alpha)(Y+(\alpha-1)(p_0+p))}{\alpha(1+m\alpha)p} \tag{70}$$

which implies that if $p > p_2$, where

$$p_2 = \frac{m(1+\alpha)(Y-(\alpha-1)p_0)}{m-\alpha} - \frac{\alpha(1-m\alpha)}{m-\alpha}p_0 \tag{71}$$

then $0 < x_2 < (1 - \frac{p_0}{p})$ and a reverse plastic zone must be formed around the cavity during the unloading.

Following the same procedure in determining the consistency of stress and strain assumptions in the axial direction of a cylindrical cavity expansion, it can easily be proved that the sufficient condition for keeping the vertical stress as the intermediate stress in the reverse plastic zone is

$$2\nu \leq 1 + \sin\phi \tag{72}$$

Because the value of Poisson's ratio can not be greater than 0.5, the above condition is automatically satisfied for a soil with any real soil parameters.

## 2.7 Plastic unloading : stress analysis

Consider now the situation when $p > p_2$ and $x > x_2$. We denote the outer radius of the reverse plastic zone by $d''$ and assume, for the present, that $d'' < b''$. The distribution of stress in the soil is now obtained by considering the regions $a'' \leq r'' \leq d''$ and $d'' \leq r''$ separately and matching the solutions at the interface $r'' = d''$. The general results of this analysis, which is not described here in detail, are as follows,

$$\sigma_r'' = \frac{Y}{\alpha-1} - \frac{(1+m)(Y+(\alpha-1)p_0)}{(\alpha-1)(m+\alpha)}\left(\frac{b}{d}\right)^{\frac{m(\alpha-1)}{\alpha}}\left(\frac{r''}{d''}\right)^{m(\alpha-1)} \tag{73}$$

$$\sigma_\theta'' = \frac{Y}{\alpha-1} - \frac{\alpha(1-m)(Y+(\alpha-1)p_0)}{(\alpha-1)(m+\alpha)}\left(\frac{b}{d}\right)^{\frac{m(\alpha-1)}{\alpha}}\left(\frac{r''}{d''}\right)^{m(\alpha-1)} \tag{74}$$

for $a'' \leq r'' \leq d''$, and

$$\sigma_r' = \frac{m(1+m)(1-\alpha)(Y+(\alpha-1)p_0)}{(\alpha-1)(m-\alpha)}\left(\frac{b}{d}\right)^{\frac{m(\alpha-1)}{\alpha}}\left(\frac{d''}{r''}\right)^{1-m} \tag{75}$$

$$\sigma'_\theta = -\frac{(1-m)(1-\alpha)(Y-(\alpha-1)p_0)}{(\alpha-1)(m+\alpha)}\left(\frac{b}{d}\right)^{\frac{m(\alpha-1)}{\alpha}}\left(\frac{d''}{r''}\right)^{1+m} \tag{76}$$

for $r'' \geq d''$.

The stress condition at the cavity wall

$$\sigma''_r(a'') = -p_0 - (1-x)p \tag{77}$$

can be used to provide the additional relation,

$$\left(\frac{a''}{d''}\right)^{m(\alpha-1)}\left(\frac{a}{d}\right)^{\frac{m(\alpha-1)}{\alpha}} = \frac{\alpha(1+m\alpha)[Y+(\alpha-1)(p_0+(1-x)p)]}{(m-\alpha)(Y-(\alpha-1)(p_0-p))} \tag{78}$$

The unloading displacement in the region $r'' \geq d''$ can be shown to be

$$u' = -\frac{(1+m)(1-\alpha)(Y-(\alpha-1)p_0)}{2(m+\alpha)(1+m\alpha)G}\left(\frac{b}{d}\right)^{\frac{m(\alpha-1)}{\alpha}}\left(\frac{d''}{r''}\right)^{1-m} r'' \tag{79}$$

and in particular we have

$$\begin{aligned} d &= d'' - u'(d'') \\ &= d''\left[1 - \frac{(1+m)(1-\alpha)(Y+(\alpha-1)p_0)}{2(m+\alpha)(1-m\alpha)G}\left(\frac{b}{d}\right)^{\frac{m(\alpha-1)}{\alpha}}\right] \end{aligned} \tag{80}$$

The consistency of the above results and the earlier assumption $d'' < b''$ can be generally proved as follows. Combining equations ( 70) and ( 78) leads to:

$$\left(\frac{a''}{d''}\right)^{m(\alpha-1)}\left(\frac{a}{d}\right)^{\frac{m(\alpha-1)}{\alpha}} < 1 \tag{81}$$

Inequality ( 81) and $a'' < d''$ imply that $a < d$. Use of the condition that at the cavity wall the value of the displacement after reverse yielding exceeds elastic unloading displacement may be made to give $\frac{a}{d} > \frac{a''}{d''}$.

From equations ( 39) and ( 78) we have

$$\begin{aligned} \left(\frac{a}{d}\right)^{m(\alpha-1)}\left(\frac{b}{d}\right)^{\frac{m(\alpha-1)}{\alpha}} &> \left(\frac{a''}{d''}\right)^{m(\alpha-1)}\left(\frac{b}{d}\right)^{\frac{m(\alpha-1)}{\alpha}} \\ &= \frac{(1-m\alpha)[Y+(\alpha-1)(p_0+(1-x)p)]}{(1-m)(Y+(\alpha-1)p_0)} \geq 1 \end{aligned} \tag{82}$$

Hence we have $d < b$ and $d'' < b''$.

## 2.8 Plastic unloading : displacement analysis

The non-associated plastic flow rule for the reverse plasticity defined by

$$\frac{\dot{\epsilon}_r^{p''}}{\dot{\epsilon}_\theta^{p''}} = -m\beta \tag{83}$$

can be used for the evaluation of the displacement in the reverse plastic zone, $a'' \leq r'' \leq d''$.

Substituting the elastic solutions provided by equations ( 22), ( 23) into the reverse plastic flow rule ( 83) leads to

$$\begin{aligned} \dot{\epsilon}_r'' + m\beta\dot{\epsilon}_\theta'' &= \frac{1-\nu^2(2-m)}{E}\{[1-\frac{m\beta\nu}{1-\nu(2-m)}]\dot{\sigma}_r'' \\ &\quad -[m\beta(1+\nu-m\nu)-\frac{m\nu}{1-\nu(2-m)}]\dot{\sigma}_\theta''\} \end{aligned} \tag{84}$$

The differential relation ( 84) can be integrated subject to the condition for the initial reverse yielding to occur. The total stress-strain relation is found to be

$$\begin{aligned} \epsilon_r' + m\beta\epsilon_\theta' &= \frac{1-\nu^2(2-m)}{E}\{[1-\frac{m\beta\nu}{1-\nu(2-m)}]\sigma_r'' \\ &\quad -[m\beta(1+\nu-m\nu)-\frac{m\nu}{1-\nu(2-m)}]\sigma_\theta'' \\ &\quad -\frac{Y}{\alpha-1}[1+m\beta(1+\nu-m\nu)-\frac{m\nu(1+\beta)}{1-\nu(2-m)}] \\ &\quad +\frac{(1-m)(Y+(\alpha-1)p_0)}{(\alpha-1)(m+\alpha)}[\alpha(1-\frac{m\nu\beta}{1-\nu(2-m)}) \\ &\quad -m\beta(1+\nu-m\nu)-\frac{m\nu}{1-\nu(2-m)}](\frac{b}{r})^{\frac{m(\alpha-1)}{\alpha}}\} \end{aligned} \tag{85}$$

The logarithmic strain components measured from the fully loaded state are

$$\epsilon_r' = \ln(\frac{dr''}{dr}) \tag{86}$$

$$\epsilon_\theta' = \ln\frac{r''}{r} \tag{87}$$

Substituting equation ( 73),( 74) into ( 85) results in the differential equation

$$\ln[(\frac{r''}{r})^{m\beta}\frac{dr''}{dr}] = -\lambda(\frac{r''}{d''})^{m(\alpha-1)} - \kappa(\frac{d}{r})^{\frac{m(\alpha-1)}{\alpha}} \tag{88}$$

where

$$\begin{aligned}\lambda &= \frac{[1-\nu^2(2-m)](1-m)(Y+(\alpha-1)p_0)}{(\alpha-1)(1-m\alpha)E}\{1-\frac{m\beta\nu}{1-\nu(2-m)}- \\ &[m\beta(1+\nu-m\nu)-\frac{m\nu}{1-\nu(2-m)}]\alpha\}(\frac{b}{d})^{\frac{m(\alpha-1)}{\alpha}}\end{aligned} \tag{89}$$

$$\begin{aligned}\kappa &= \frac{[1-\nu^2(2-m)](1-m)(Y+(\alpha-1)p_0)}{(\alpha-1)(m-\alpha)E}\{\alpha[1-\frac{m\beta\nu}{1-\nu(2-m)}] \\ &+m\beta(1+\nu-m\nu)-\frac{m\nu}{1-\nu(2-m)}\}(\frac{b}{d})^{\frac{m(\alpha-1)}{\alpha}}\end{aligned} \tag{90}$$

By means of the transformation

$$x = (\frac{d}{r})^{\frac{m(\alpha-1)}{\alpha}} \tag{91}$$

$$y = (\frac{r''}{d''})^{m(\alpha-1)} \tag{92}$$

Equation ( 88) can be integrated over the interval $[d'', r'']$ to give the solution

$$\begin{aligned}&\alpha\int_1^{(\frac{d}{r})^{\frac{m(\alpha-1)}{\alpha}}} x^{-\frac{\alpha(1+m\beta)}{m(\alpha-1)}-1}e^{\kappa x}dx \\ -(\frac{d''}{d})^{1-m\beta}&\int_1^{(\frac{r''}{d''})^{m(\alpha-1)}} y^{\frac{1+m\beta-m(\alpha-1)}{m(\alpha-1)}}e^{\lambda y}dy \;=\; 0\end{aligned} \tag{93}$$

putting $r = a, r'' = a''$ and with the aid of a series expansion, equation ( 93) can be integrated to give

$$\alpha\Lambda_2(\kappa, \frac{d}{a}) + (\frac{d''}{d})^{1+m\beta}\Lambda_3(\lambda, \frac{a''}{d''}) = 0 \tag{94}$$

where

$$\Lambda_2(x, y) = \sum_{n=0}^{\infty} A_n^2 \tag{95}$$

in which

$$A_n^2 = \begin{cases} \frac{x^n m(\alpha-1)}{n!\alpha} \ln y & \text{if } n = \frac{\alpha(1+m\beta)}{m(\alpha-1)} \\ \frac{x^n}{n!(n-\frac{\alpha(1+m\beta)}{m(\alpha-1)})}\{y^{\frac{m(\alpha-1)}{\alpha}(n-\frac{\alpha(1+m\beta)}{m(\alpha-1)})} - 1\} & \text{otherwise} \end{cases}$$

and

$$A_3(x,y) = \sum_{n=0}^{\infty} \frac{x^n}{n!(n-\frac{1+m\beta}{m(\alpha-1)})}\{y^{m(\alpha-1)(n+\frac{1+m\beta}{m(\alpha-1)})} - 1\} \tag{96}$$

By combining equations ( 39),( 78),( 80) and ( 94) we can obtain an equation for $\frac{a}{d}$. As the value of $a$ is known from the loading solution, the outer radius of the reverse plastic zone $d''$. $d$ will be specified if we know the unloading pressure. Alternatively, we can first specify $\frac{b}{a}$ and $\frac{d}{a}$ and then equation ( 80) and equation ( 94) can be used to determine $\frac{d}{d''}$ and $\frac{a''}{d''}$ respectively. With the known values of $\frac{d}{a}$, $\frac{a''}{d''}$ and $\frac{d}{d''}$, the cavity contraction ratio $\frac{a''}{a}$ can be easily evaluated. Finally, equation ( 39) and equation ( 78) can be used to calculate the loading cavity pressure and the unloading cavity pressure respectively. Following this procedure, the whole unloading pressure-contraction curve can be obtained.

When the elastic deformation in the plastic zone is neglected, equation ( 94) becomes:

$$(\frac{d''}{d})^{1+m\beta} = \frac{1-(\frac{a}{d})^{1+m\beta}}{1-(\frac{a''}{d''})^{1+m\beta}} \tag{97}$$

Consequently, the equation for $\frac{a}{d}$ may be shown to be

$$\{\frac{1-(\frac{a}{d})^{1+m\beta}}{1-\{\frac{\alpha(1+m\alpha)[Y+(\alpha-1)(p_0+(1-\alpha)p)]}{(m+\alpha)(Y+(\alpha-1)(p_0+p))}\}^{\frac{1+m\beta}{m(\alpha-1)}}(\frac{a}{d})^{-\frac{1+m\beta}{\alpha}}}\} =$$

$$\{1+\frac{(1+\alpha)(Y+(\alpha-1)(p_0+p))}{2\alpha(1+m\alpha)G}(\frac{a}{d})^{\frac{m(\alpha-1)}{\alpha}}\}^{-(1+m\beta)} \tag{98}$$

## 2.9 Results

A selection of results is now presented in order to indicate the effects of various key parameters on the behaviour of cavity expansion and contraction. Solutions for the

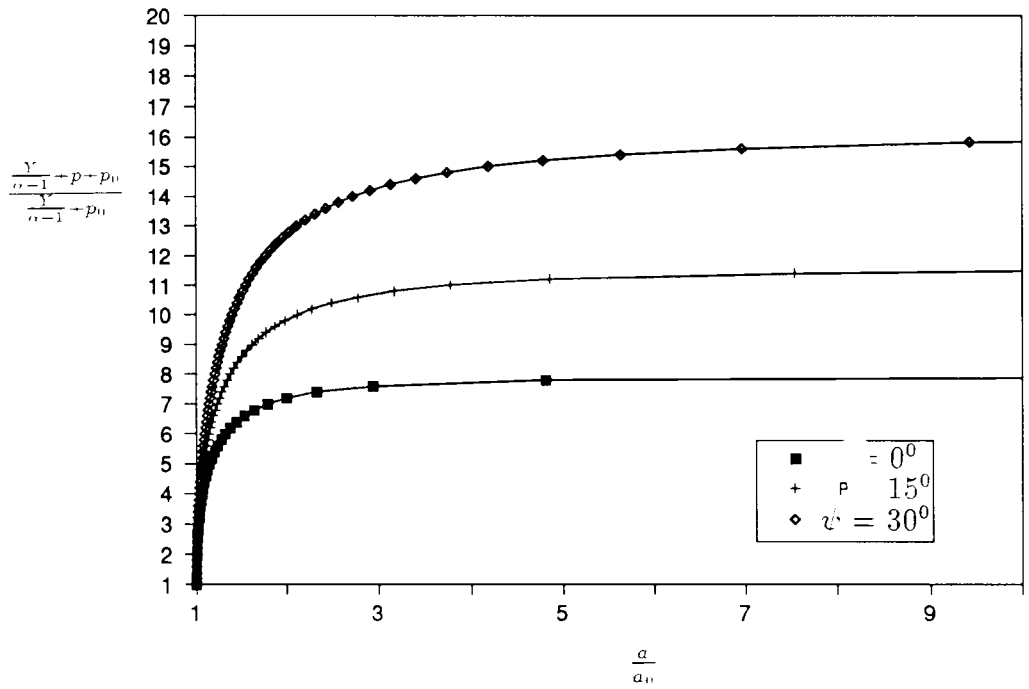


Figure 1: A typical pressure expansion curve for cylindrical cavity

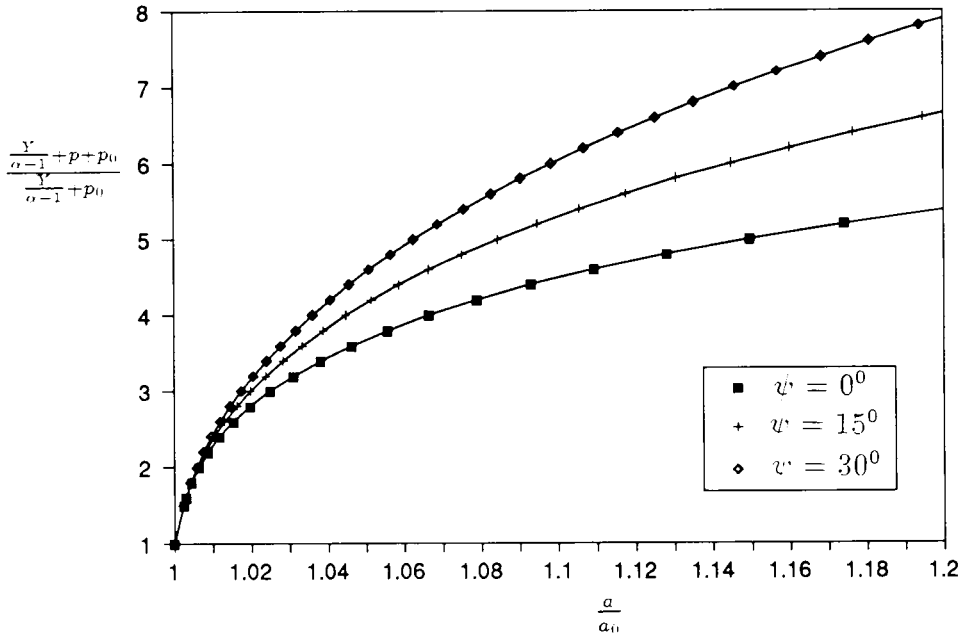


Figure 2: The initial portion of a typical pressure expansion curve for cylindrical cavity

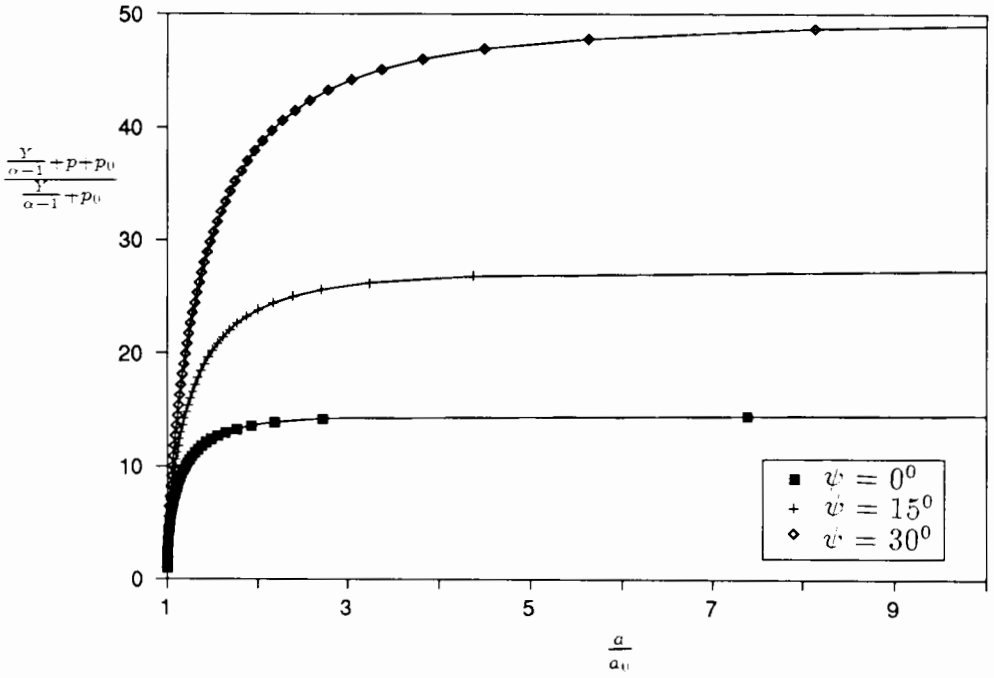


Figure 3: A typical pressure expansion curve for spherical cavity

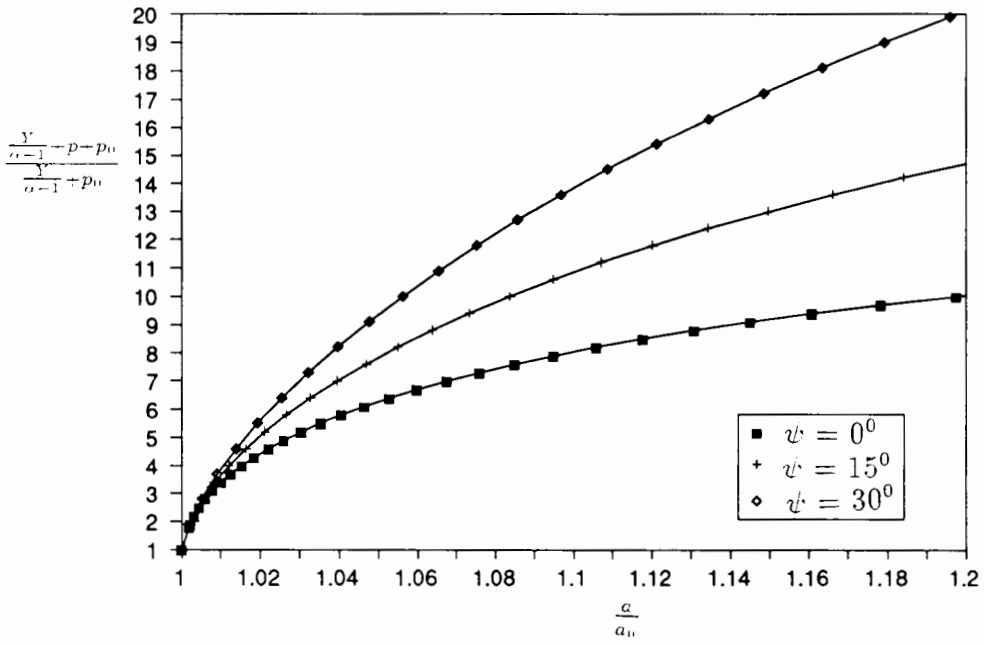


Figure 4: The initial portion of a typical pressure expansion curve for spherical cavity

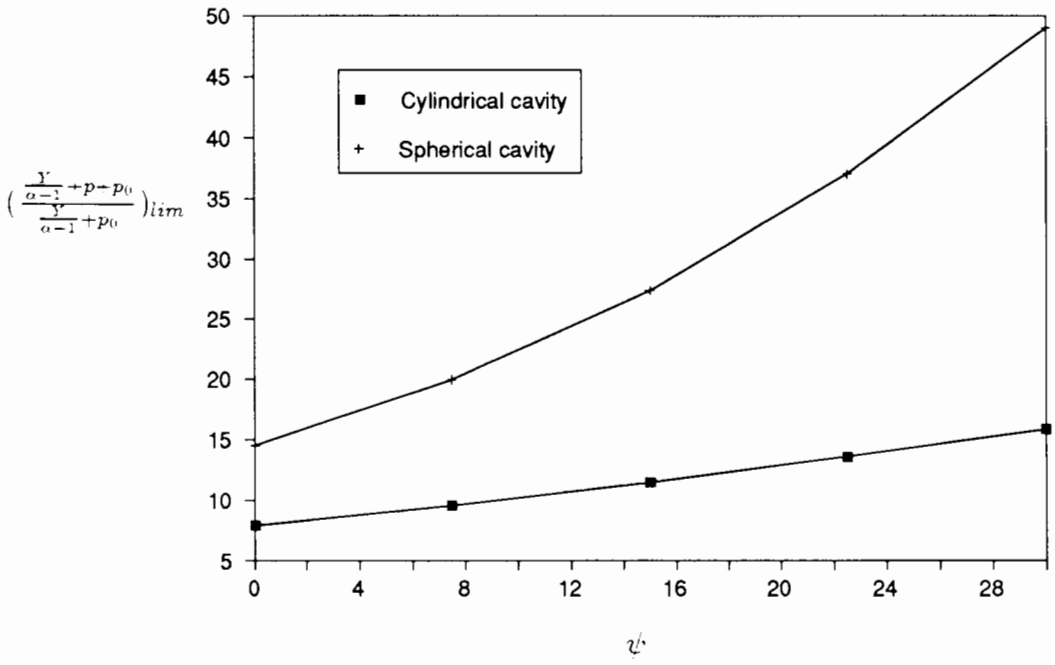


Figure 5: Variation of limit pressure with dilation angle

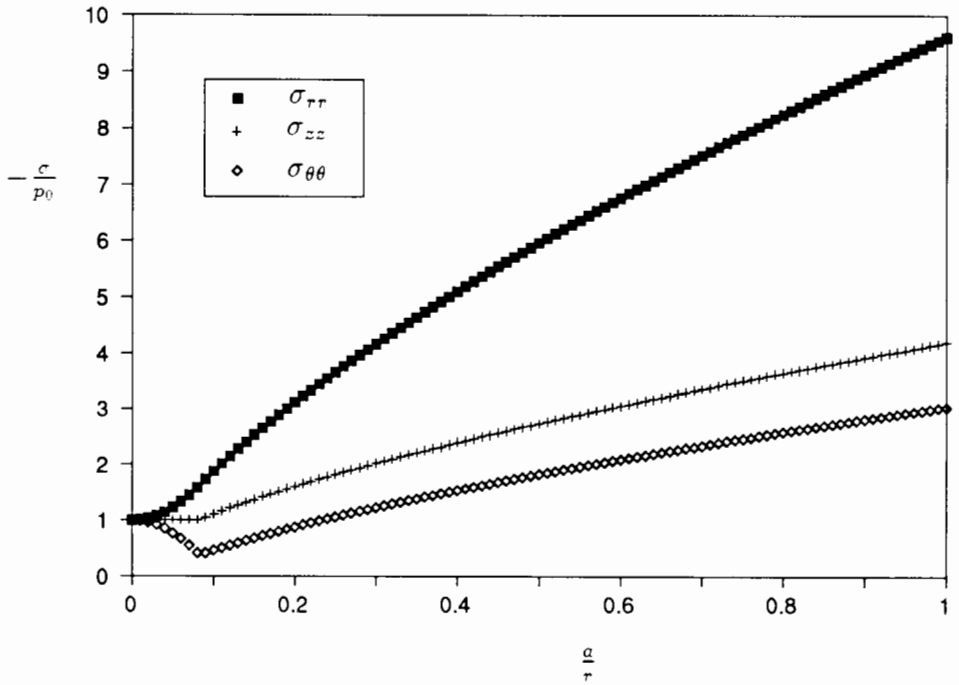


Figure 6: Stress distribution for cylindrical cavity expansion with $\psi = 0^0$

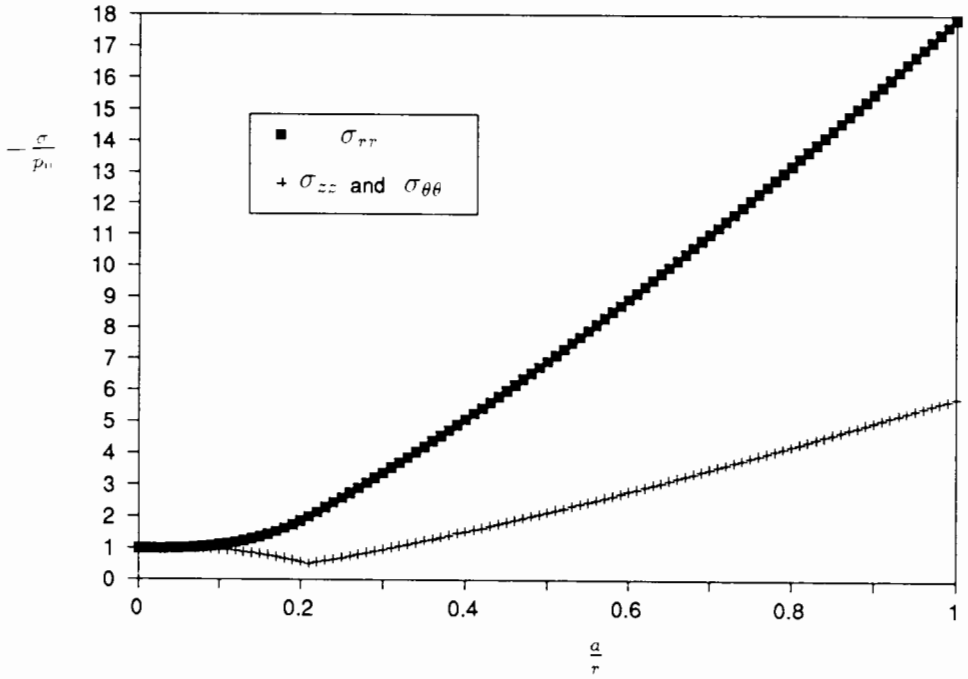


Figure 7: Stress distribution for spherical cavity expansion with $\psi = 0^0$

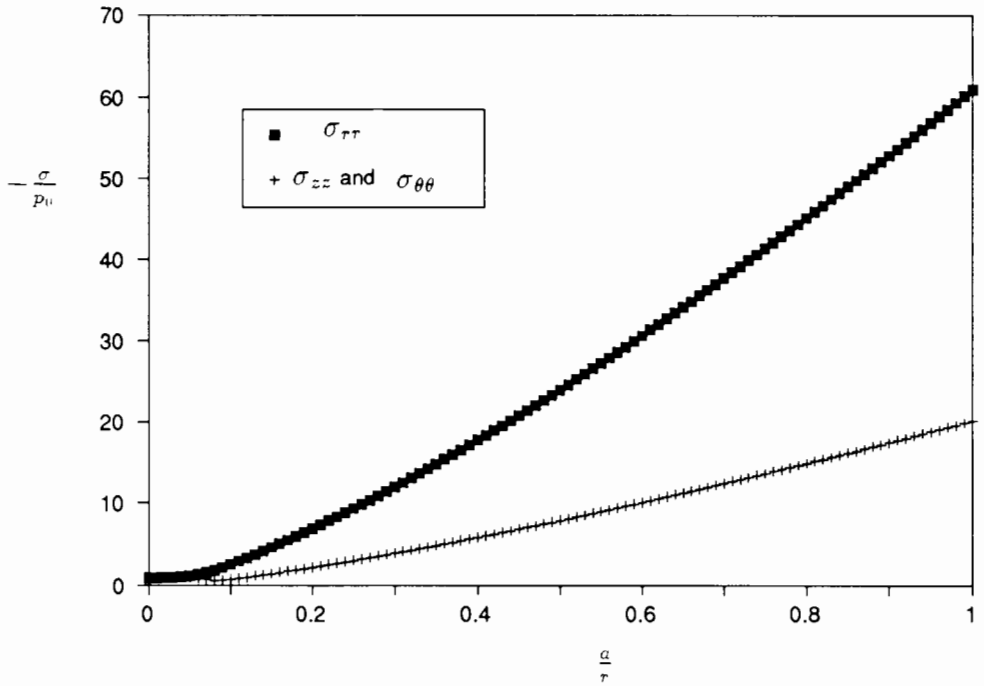


Figure 8: Stress distribution for spherical cavity expansion with $\psi = 30^0$

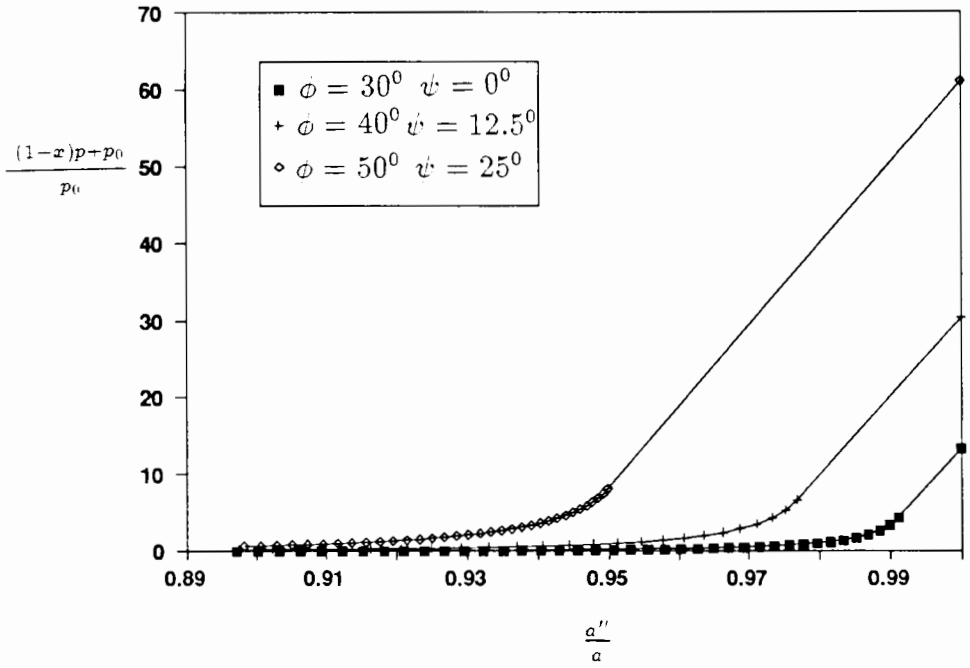


Figure 9: Typical pressure contraction curves for cylindrical cavity on linear plot

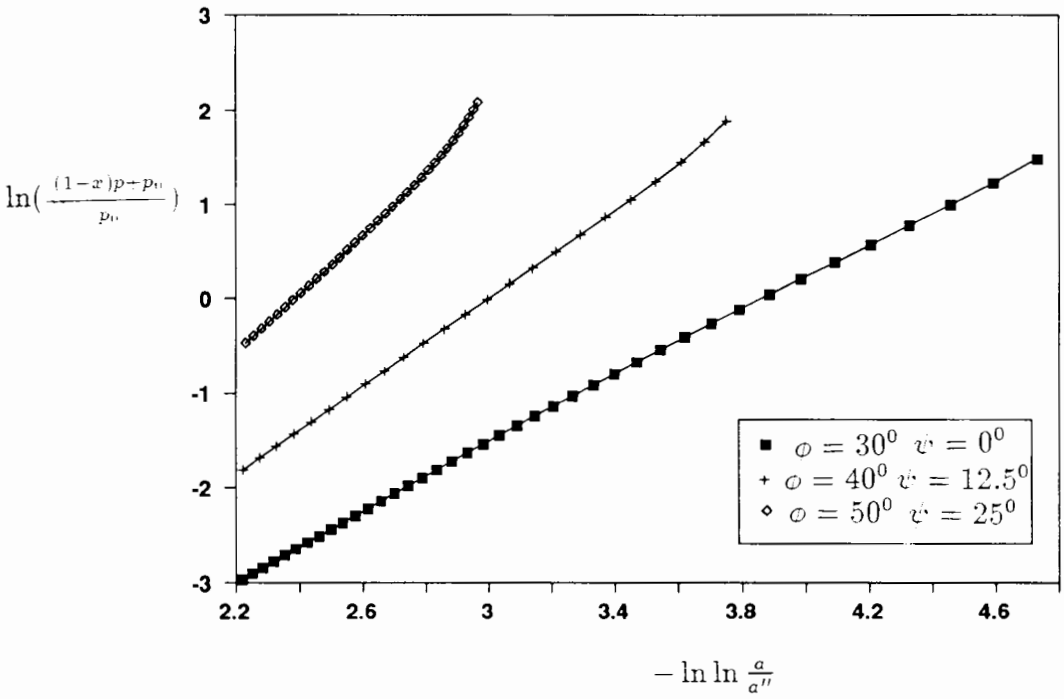


Figure 10: Typical plastic pressure contraction curves for cylindrical cavity on logarithmic plot

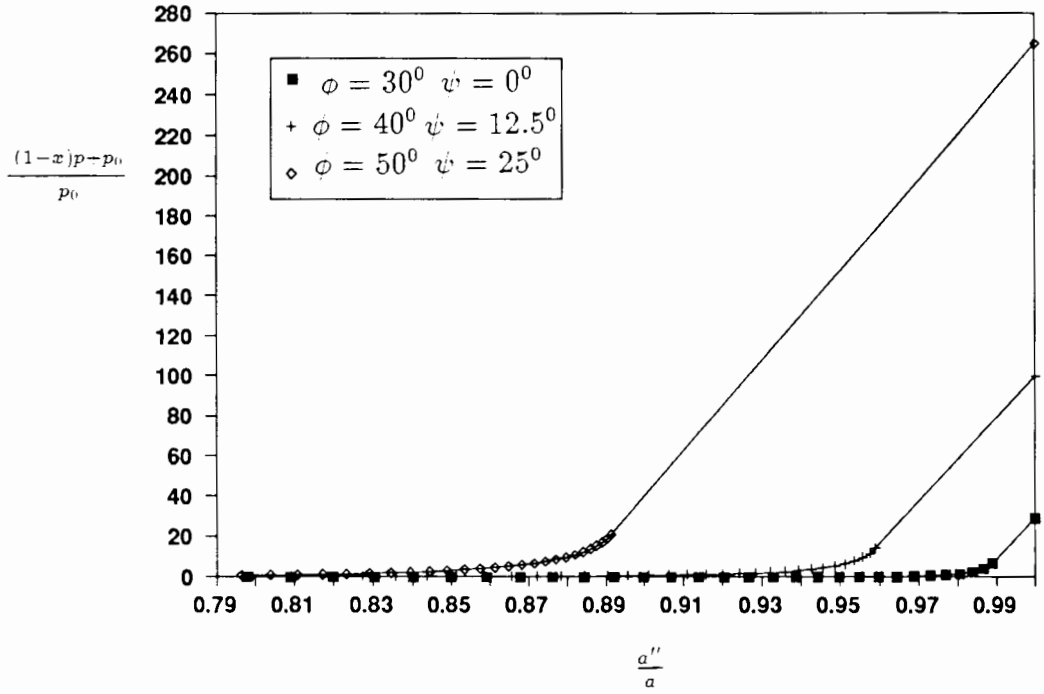


Figure 11: Typical pressure contraction curves for spherical cavity on linear plot

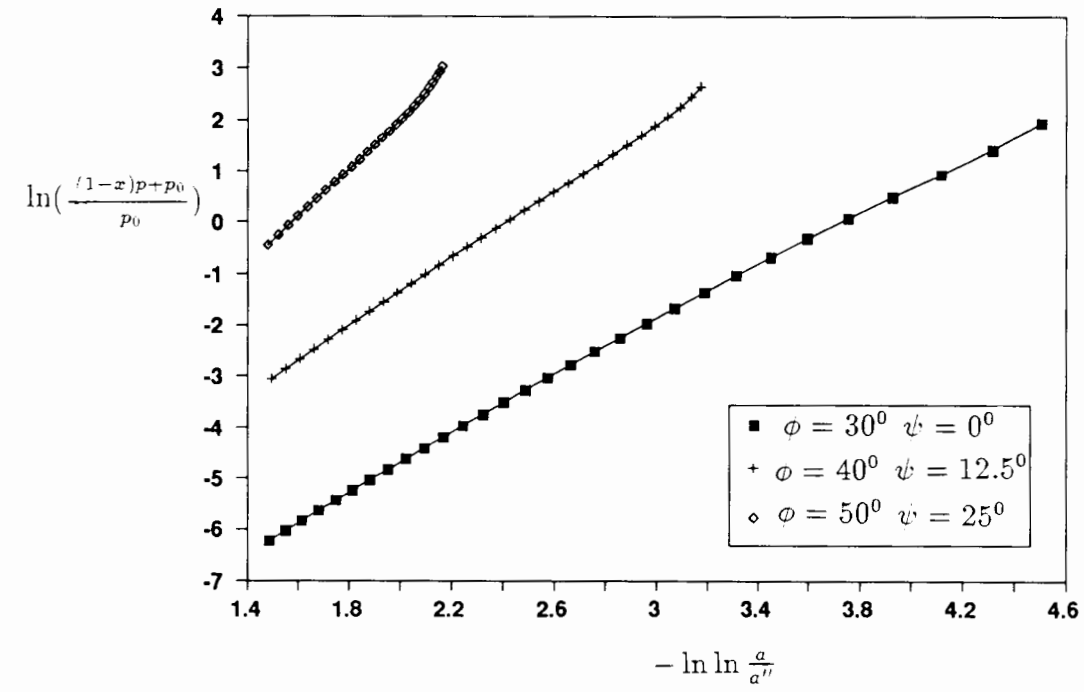


Figure 12: Typical plastic pressure contraction curves for spherical cavity on logarithmic plot

pressure-expansion relationship, defined by equation ( 56), have been evaluated for materials with Poisson's ratio $\nu = 0.3$, friction angle $\phi$ of $30^0$ and various values of dilation angle $\psi$. The general stiffness index for cohesive-frictional materials $\frac{E}{p_0+\frac{Y}{(\alpha-1)}}$ has been set to be 260. These results are presented graphically in Figure 1 and Figure 3 for a cylindrical cavity and Figure 2 and Figure 4 for a spherical cavity in two different scales. Figure 5 presents the variation of the limit pressure with dilation angle, which are obtained from equation ( 58). The distributions of stresses defined in equations ( 33)-( 38) when the cavity expansion ratio equals ten and $Y = 0.5p_0$ are presented in Figure 6 and Figures 7- 8 for both cylindrical and spherical cavities respectively. Perhaps the most interesting feature of these results is the strong dependence of both the cavity pressure expansion curves and stress distributions on the dilation of the soil.

As far as cavity contraction is concerned, a selection of results for a soil with a value of stiffness index $\frac{E}{\frac{Y}{(\alpha-1)}+p_0}$ of 1300 and a Poisson's ratio of 0.3 is presented. The cohesion of the soil is assumed to be zero (i.e. $\frac{Y}{(\alpha-1)} = 0$) and the unloading is assumed to start after cavity expansion has reached a cavity expansion ratio of 5. A set of values for friction angle and dilation angle of the soil was chosen to investigate the significance of dilatancy of the soil during unloading. Figure 9 and Figure 10 present the cylindrical cavity pressure contraction curves for a soil with different dilation angles on linear and logarithmic plots respectively. The spherical cavity unloading curves for different cases are shown in Figure 11 and Figure 12. It is interesting to note that the plastic unloading curves are approximately straight on a logarithmic plot. This is particularly true for the soil with a low dilation angle. The slope of the plastic unloading curve is generally found to increase with dilation angle. By contrast, the small strain unloading analysis indicates that the plastic loading curve should be a straight line on such a logarithmic plot (Houlsby et al., 1986; Withers et al., 1989). It would therefore appear that the small strain unloading analysis is less suitable for approximating large strain cavity contraction in a dense sand than in a loose sand.

## 2.10 Conclusion

A unified analytical solution is presented for stress and displacement field for the expansion and contraction of both cylindrical and spherical cavities in dilatant soils. The approach using the direct integration of strain rate and the logarithmic strain definition has been used so that large strain effects can be taken into account. The dilatancy of the soil is accounted for by adopting the Mohr-Coulomb yield criterion with a non-associated plastic flow rule. An explicit expression for the pressure-expansion relationship has been obtained for a displacement with arbitrary magnitude. The analytical limit pressure can then be determined as a special case when the cavity radius approaches infinity. Finally, closed form equations for solving residual stress and displacement distributions are derived at any stage of the unloading. Some selected results are presented to highlight the capability of the proposed solutions.

# Chapter 3

# One Dimensional Finite Element Formulation for Cavity Expansion

## 3.1 Introduction

Closed form solutions are presented in Chapter 2 for the expansion of cylindrical and spherical cavities in an infinite, homogeneous and isotropic medium. In the analysis, the soil has been idealised as an elastic and perfectly plastic material. As more realistic soil behaviour and boundary conditions are taken into account, analytical treatment becomes exceedingly difficult to handle and it is normally necessary to adopt a numerical approach.

In this chapter, the basic equations governing one-dimensional cavity expansion in an elasto-plastic material are formulated using the principal of virtual work. These equations are subsequently solved numerically by the finite element method.

## 3.2 Consideration of incompressibility constraints

The correct prediction of failure loads is of major importance in soil mechanics problems. Unfortunately, the literature shows clearly that in conventional finite element computations using the displacement formulation with elastic-plastic soil models, theoretical limit loads are often overpredicted (Sloan, 1981). The reason for this is discussed in several papers. In agreement with others, Sloan and Randolph (1982) state that the problem is

related to the ability of the displacement based finite element to model an incompressible deformation mode. Nordal and Antonsen (1985) show that an overprediction of limit loads is due to a conflict between the plastic flow rule and the finite element discretization. The conflict arises when a plastic deformation mode, as defined by the flow rule, cannot be modelled by the shape functions and the available degrees of freedom for an element.

The incompressibility condition also affects the quality of the stresses calculated using the finite element method. Naylor (1974) and Burd and Houlsby (1990) show that when exact integration is used, and as incompressibility is approached, a reduction in the accuracy of stress calculations occurs, taking the form of stress oscillations across the element. It was found that these inaccuracies are mainly confined to the mean stress terms.

Several methods have been proposed to improve the performance of the displacement method, when used to model an incompressible deformation mode. Examples of these approaches are the Mixed Finite Element Formulation (Fraeijs de Veubeke, 1965; Herrmann, 1965) , Uniform Reduced Integration Element (Naylor, 1974; Zienkiewicz et al., 1971), Reduced-Selective Integration Elements (Doherty et al., 1969; Malkus, 1976) and High Order Elements (Sloan, 1981; Sloan and Randolph, 1982; de Borst and Vermeer, 1984).

The Mixed Finite Element Formulation was discussed by Fraeijs de Veubeke (1965) and Herrmann (1965). Herrmann developed a reduced form of Reissner's variational principle particularly suited to problems of incompressible elasticity and, based on this principle, established the first effective finite element for such cases.

The first example of a Uniform Reduced Integration Element was apparently the plate-shell element presented by Zienkiewicz et al.(1971). The same concept was employed for other applications. In particular, Naylor (1974) advocated the use of the eight-node serendipity element in problems involving incompressibility. The procedure, however, has disadvantages as well as advantages.

The concept of Selective Integration was employed by Doherty et al.(1969) to obtain improved bending behaviour in simple four-node elasticity elements. One-point Gauss

quadrature was used for the shear strain term, and $2\times2$ Gauss quadrature was used to integrate the remaining terms. Although improved behaviour was noted in some configurations, the lack of coordinate invariance opened the approach to criticism. Malkus (1976) proved the equivalence of a class of mixed models to reduced selective integration single-field elements in linear elasticity theory, for plane strain and three dimensional analysis. However, the equivalence breaks down in the case of axisymmetry. In addition, for both Uniform and Selective Integration Elements, there is a danger of exciting "zero energy modes" which can communicate to form a singular, or nearly singular, global stiffness. In the singular case, no solution is possible.

After a comprehensive study, Sloan and Randolph (1982) showed that if the total number of the degrees of freedom are held constant, then the total number of constraints can be reduced by using High Order Elements. A satisfactory finite element solution can thus be obtained for nearly incompressible behaviour without having to resort to the use of reduced integration. Although this approach works well, it suffers from the drawback that for some problems very high order elements must be developed, with penalties on development time and to a lesser extent on computing time.

Little effort has been devoted in the past to the effects of changes of the displacement interpolation on the quality of limit pressure predictions, and the stresses calculated using displacement finite element methods. As Nordal and Antonsen (1985) pointed out, the shape functions may have significant influence on finite element predictions when elastic-plastic models are used in the analysis. This is because in the elastic-plastic finite element analysis, overshoot of limit loads sometimes occurs due to a conflict between the plastic flow rule and the finite element discretization.

The effects of changes in the displacement interpolation on the finite element prediction of limit pressures and stresses are studied in this chapter. Analyses of cylindrical and spherical cavity expansion problems have been used to highlight the suitability of the numerical formulation.

## 3.3 Finite element formulation

In the analysis of cylindrical cavity expansion, the expansion is assumed to occur under conditions of plane strain and axial symmetry in a medium of either finite or infinite extent. In the numerical analysis, the cavity expansion is assumed to start from a small rather than zero radius to avoid numerical difficulties. In order to model this problem of infinite extent using a mesh of finite dimensions, an outer infinite spring element is introduced (Yeung, 1988).

In order to carry out the analysis for both cylindrical and spherical cavity expansions at the same time, the following notation which is defined in Chapter 2 has been retained:

$$m = \begin{cases} 1 & \text{for the cylindrical case} \\ 2 & \text{for the spherical case} \end{cases}$$

An Eulerian definition of strain rate is adopted, in which the Eulerian strains at each Gauss point within the element are accumulated as the calculation proceeds. The strain rate vector is defined as:

$$\dot{\epsilon} = \begin{Bmatrix} \dot{\epsilon_r} \\ \dot{\epsilon_z} \\ \dot{\epsilon_\theta} \end{Bmatrix} = [L]u \tag{99}$$

where

$$[L] = [\frac{\partial}{\partial r}, \frac{(m-1)}{r}, \frac{1}{r}]^T \tag{100}$$

and the velocity in the radial direction is given by $u$.

The stress rate vector is defined as follows:

$$\dot{\sigma} = \begin{Bmatrix} \dot{\sigma_r} \\ \dot{\sigma_z} \\ \dot{\sigma_\theta} \end{Bmatrix} \tag{101}$$

A two-node element was adopted in this study, so that the velocity field around a cavity is represented by values at the connecting nodes. For the element $e_{ij}$, connecting nodes $i$ and $j$, we have:

$$\underline{u} = \left\{ \begin{array}{c} u_i \\ u_j \end{array} \right\} \tag{102}$$

The continuous velocity field in the element $u$ can be approximated by the following equation:

$$u = [N]_{ij}\underline{u} \tag{103}$$

where the shape function matrix is defined:

$$[N]_{ij} = [N_i, N_j] \tag{104}$$

From equations ( 99) and ( 103) the strain rates are related to the nodal velocities by the following equation:

$$\dot{\epsilon} = [L][N]_{ij}\underline{u} = [B]_{ij}\underline{u} \tag{105}$$

where

$$[B]_{ij} = \left[ \begin{array}{cc} \frac{\partial N_i}{\partial r} & \frac{\partial N_j}{\partial r} \\ \frac{N_i(m-1)}{r} & \frac{N_j(m-1)}{r} \\ \frac{N_i}{r} & \frac{N_j}{r} \end{array} \right] \tag{106}$$

From the principle of virtual work, the nodal forces $\mathbf{P}$ in equilibrium with a set of stresses $\sigma$ are:

$$\mathbf{P} = \pi \int_{r_i}^{r_j} [B]_{ij}^T \sigma (2r)^m \, dr \tag{107}$$

If we ignore the effects of element distortion (i.e. limit the analysis to small strain increments), the rate form of the virtual work principle may be written as follows:

$$\dot{\mathbf{P}} = [K]_{ij}\underline{u} \tag{108}$$

where:

$$[K]_{ij} = \pi \int_{r_i}^{r_j} [B]_{ij}^T [D]^{ep} [B]_{ij} (2r)^m \, dr \tag{109}$$

and $[D]^{ep}$ is the elastic-plastic matrix which links a stress increment to a strain increment for the given material. The general expression for $[D]^{ep}$ in an elastic-perfectly plastic analysis may be shown to be:

$$[D]^{ep} = [D]^{e} - \frac{[D]^{e}[b][a]^{T}[D]^{e}}{[a]^{T}[D]^{e}[b]} \tag{110}$$

where

$$a = \frac{\partial f}{\partial \sigma} \tag{111}$$

$$b = \frac{\partial g}{\partial \sigma} \tag{112}$$

in which, $f$ and $g$ denote the yield surface and plastic potential respectively for the given material.

In order to model an infinite medium using an outer infinite spring element, the interface between the last annular element and the spring element should be selected such that the spring element always remains elastic. Hence, the radial stiffness $K_{ss}$, which relates the radial force acting at the interface to the radial displacement at the interface can be computed from the cavity expansion theory in an infinite elastic medium and may be shown to be:

$$K_{ss} = 4m^2\pi G(r_n)^{m-1} \tag{113}$$

where $G$ denotes shear modulus, $r_n$ is radius of the interface between the last annular element and the infinite spring element.

To evaluate the shape function matrix $[N]_{ij}$, some assumptions about the displacement interpolation are needed. Following the conventional approach, in which a linear displacement interpolation along an element is assumed, the two-node element $e_{ij}$ has the following shape function matrix:

$$[N]_{ij} = \left[\frac{r_j - r}{r_j - r_i}, \frac{r - r_i}{r_j - r_i}\right] \tag{114}$$

The above shape function matrix is derived using the conventional linear displacement interpolation, namely:

$$u = C_0 - C_1 r \tag{115}$$

In this chapter, the following novel non-linear displacement interpolation is assumed within each element:

$$u = \frac{C_0}{r^m} - C_1 r \tag{116}$$

where $C_0$ and $C_1$ are constants for a given element.

Based on this displacement interpolation the new shape functions are derived as follows:

$$N_i = \frac{(r_j^{m+1} - r^{m+1}) r_i^m}{(r_j^{m+1} - r_i^{m+1}) r^m} \tag{117}$$

$$N_j = \frac{(r^{m+1} - r_i^{m+1}) r_j^m}{(r_j^{m+1} - r_i^{m+1}) r^m} \tag{118}$$

The rationale behind the new approach is as follows. As the material becomes almost incompressible, the displacements around the cavity in an infinite medium become of the form $u = C/r^m$ where $C$ is constant. The conventional displacement expansion is unable to capture this mode exactly, whereas the new expansion does. Furthermore the new expansion captures exactly the elasticity solution for general cavity expansion in compressible or incompressible materials.

## 3.4 Singularities in the yield surface

Ideal elastic perfectly plastic behaviour has been adopted in this chapter for modelling both clay and sand. The most common constitutive laws used in finite element models to represent cohesive and frictional soils are the Tresca (or von Mises) and Mohr-Coulomb models. These models have been deliberately chosen here mainly for their simplicity. The Tresca and Mohr-Coulomb models, however, contain discontinuous yield surface with 'edges' at which the yield function is not differentiable. These singularities deserve

special treatment as they are particularly important for cavity expansion problems. Several approaches exist for dealing with these singularities. One of the classical approaches is due to Nayak and Zienkienicz (1972) and consists in using only one yield function in combination with a rounding off procedure for points at which two planes of the yield function meet (so-called corner point). Sloan and Booker (1986) adopted a modified surface to round off the corners so that a smooth yield surface may be obtained. Although these approaches prove to be effective to some extent, they are mathematically inconvenient and physically too artificial.

In this chapter, these singularities are dealt with by using the assumption that the total plastic strain rate is the sum of the individual contributions of the two flow rules (Koiter, 1960). This assumption may be simply expressed as:

$$\dot{\epsilon^p} = \lambda_1 b_1 + \lambda_2 b_2 \tag{119}$$

where

$$b_1 = \frac{\partial g_1}{\partial \sigma} \tag{120}$$

$$b_2 = \frac{\partial g_2}{\partial \sigma} \tag{121}$$

and $\lambda_1, \lambda_2$ are scalar multipliers, $g_1, g_2$ are plastic potentials.

If the corner is defined by two yield functions $f_1(\sigma) = 0, f_2(\sigma) = 0$, then on plastic yielding, the stress state will stay on the yield surface, thus,

$$a_1 \dot{\sigma} = 0 \tag{122}$$

$$a_2 \dot{\sigma} = 0 \tag{123}$$

where

$$a_1 = \frac{\partial f_1}{\partial \sigma} \tag{124}$$

$$a_2 = \frac{\partial f_2}{\partial \sigma} \tag{125}$$

The total strain rate may be decomposed into elastic and plastic strain rates:

$$\dot{\epsilon} = \dot{\epsilon^e} + \dot{\epsilon^p} \tag{126}$$

The elastic strain rate is related to the stress rate through Hooke's law:

$$\dot{\sigma} = [D]^{\epsilon}\dot{\epsilon}^{\epsilon} \tag{127}$$

where $[D]^{\epsilon}$ is a matrix of elastic constants.

Substituting equations ( 119)( 126)( 127) into the equations ( 122)( 123) gives:

$$\begin{bmatrix} a_1[D]^{\epsilon}b_1 & a_1[D]^{\epsilon}b_2 \\ a_2[D]^{\epsilon}b_1 & a_2[D]^{\epsilon}b_2 \end{bmatrix} \begin{bmatrix} \lambda_1 \\ \lambda_2 \end{bmatrix} = \begin{bmatrix} a_1[D]^{\epsilon}\dot{\epsilon} \\ a_2[D]^{\epsilon}\dot{\epsilon} \end{bmatrix} \tag{128}$$

Equation ( 128) has a general solution which is of the form:

$$\lambda_1 = h_1\dot{\epsilon} \tag{129}$$

$$\lambda_2 = h_2\dot{\epsilon} \tag{130}$$

where $h_1$ and $h_2$ can be easily derived from equation ( 128).

The above two equations may be substituted into equations ( 119) ( 126)( 127) to obtain a relationship between the stress rate and the total strain rate:

$$\dot{\sigma} = [D]^{ep}\dot{\epsilon} \tag{131}$$

where

$$[D]^{ep} = [D]^{\epsilon} - [D]^{\epsilon}[b_1]h_1 - [D]^{\epsilon}[b_2]h_2 \tag{132}$$

Although the expression of the elastic-plastic stiffness, as defined by equation ( 110) or equation ( 132), seems somewhat complicated, it is in fact very simple, as we can deduce for the Mohr-Coulomb criterion that

$$[D]^{ep} = C_2 \begin{bmatrix} (K+\frac{G}{3})(1+\sin\phi)(1+\sin\psi) & (K-\frac{2G}{3})(1+\sin\phi) & (K+\frac{G}{3})(1+\sin\phi)(1-\sin\psi) \\ (K-\frac{2G}{3})(1+\sin\psi) & (K(1-3\sin\phi\sin\psi)+\frac{4}{3}G) & (K-\frac{2G}{3})(1-\sin\psi) \\ (K+\frac{G}{3})(1-\sin\phi)(1+\sin\psi) & (K-\frac{2G}{3})(1-\sin\phi) & (K+\frac{G}{3})(1-\sin\phi)(1-\sin\psi) \end{bmatrix} \tag{133}$$

in which

$$C_2 = \frac{G}{G + (K+\frac{1}{3}G)\sin\phi\sin\psi} \tag{134}$$

when the stress state lies on the yield surface

$$f = \sigma_3 - \sigma_1 - (\sigma_3 - \sigma_1)\sin\phi - 2c\cos\phi = 0 \tag{135}$$

and

$$[D]^{ep} = C_3 \begin{bmatrix} (1-\sin\phi)(1-\sin\psi) & (1-\sin\phi)(1-\sin\psi) & (1-\sin\phi)(1-\sin\psi) \\ (1-\sin\phi)(1-\sin\psi) & (1-\sin\phi)(1-\sin\psi) & (1-\sin\phi)(1-\sin\psi) \\ (1-\sin\phi)(1-\sin\psi) & (1-\sin\phi)(1-\sin\psi) & (1-\sin\phi)(1-\sin\psi) \end{bmatrix} \tag{136}$$

in which

$$C_3 = \frac{9KG}{12K\sin\phi\sin\psi + G(3-\sin\phi)(3-\sin\psi)} \tag{137}$$

for the case when the stress state lies on the corner defined by the following two yield functions:

$$f_1 = \sigma_3 - \sigma_1 - (\sigma_3 + \sigma_1)\sin\phi - 2c\cos\phi = 0 \tag{138}$$

$$f_2 = \sigma_2 - \sigma_1 - (\sigma_2 + \sigma_1)\sin\phi - 2c\cos\phi = 0 \tag{139}$$

where $\phi, \psi$ and $c$ denote friction angle, dilation angle and cohesion of a soil respectively and the condition $\sigma_1 \leq \sigma_2 \leq \sigma_3 \leq 0$ is assumed to be satisfied.

The expression of the elastic-plastic stiffness for the Tresca plasticity can be easily obtained by putting $\phi = 0, \psi = 0$ in equations ( 133) and ( 136).

## 3.5 Global solution scheme

In order to give a complete description of some basic procedures in the non-linear finite element analysis, a discussion on the solution scheme is given in this section and this follows closely the discussion given by Burd (1986). In general, many different approaches have been proposed and these may be divided into two main categories.

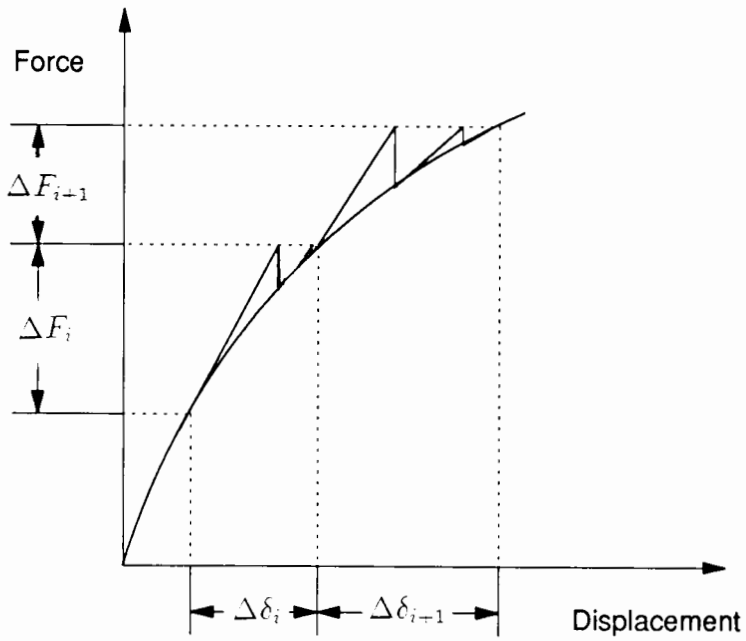


Figure 13: Newton-Raphson solution scheme (after Burd, 1986)

The simplest solution algorithm is the Euler scheme in which the exact curve is approximated by a series of straight lines having a slope equal to that of the exact curve at the start of the increment. More refined variants of this sort have also been used successfully. Carter et al.(1977) modified the basic scheme by using the slope of the exact curve at the mid-point of the increment. Another variation employs the stiffness at the start of the load increment but provides a correction procedure for the out-of-balance nodal forces at the next increment (Sloan, 1981).

An alternative to the Euler based schemes is the Newton-Raphson set of algorithms, the basic form of which is illustrated in Figure 13. An approximation to the exact curve is again made based on the slope at the start of the increment but the approximation is then refined using an iterative procedure in which the stiffness is updated at each iteration. This can lead to excessive computing time because of the need to evaluate and invert the stiffness matrix for each iteration. A possible refinement is to use the stiffness matrix calculated at the start of the increment for all the iterations within that increment, as described by Nayak and Zienkiewicz (1972).

The choice of solution scheme for a non-linear finite element formulation depends

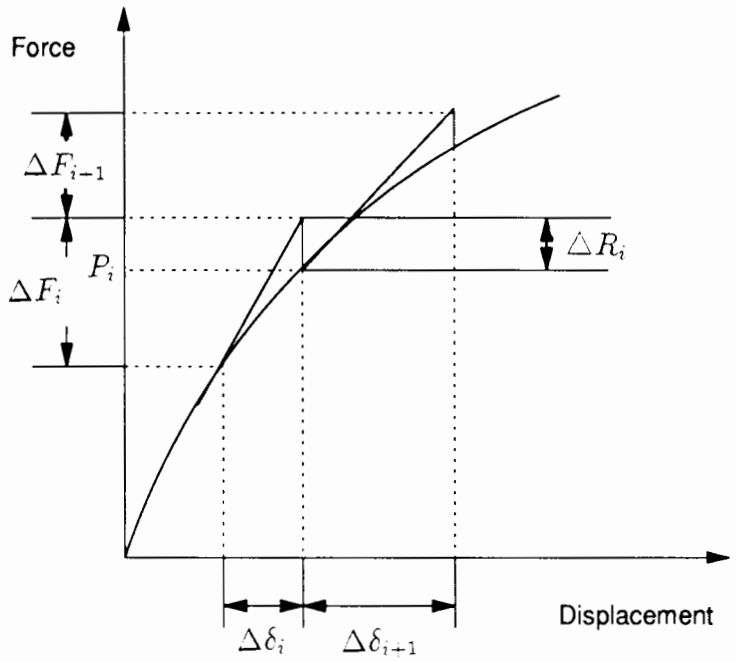


Figure 14: Modified Euler solution scheme (after Burd, 1986)

on the type of non-linearities present and the available computational facilities. In this thesis, the modified Euler scheme described by Sloan (1981) is adopted, partly because it tends to be more robust than the Newton-Raphson scheme and partly because this algorithm has been shown to be efficient and numerically stable in a series of collapse load calculations by Sloan. The particular form of the modified Euler scheme used to obtain all of the finite element solutions presented in this thesis is illustrated diagrammatically in Figure 14 with reference to a single degree of freedom system.

At the start of the $i^{th}$ load step, the individual element stiffness matrices are calculated and assembled for solving a set of incremental nodal displacements $\triangle\delta_i$. The next step is to calculate a set of stress increments $\triangle\sigma$ at each Gauss point, corresponding to the set of incremental nodal displacements $\triangle\delta_i$. The final step in the solution scheme is to calculate the nodal loads equivalent to the updated stresses in the updated geometry, denoted by $P_i$ in Figure 14. These forces are calculated from the virtual work principal. A set of unbalanced nodal loads $\triangle R_i$ are then calculated and applied as an equilibrium correction during the next load increment.

# Chapter 4

# One Dimensional Finite Element Analysis and the Cone-Pressuremeter Test in Sand

## 4.1 Introduction

The cone-pressuremeter test is a relatively new in-situ test in which a pressuremeter is combined with a standard cone. The interpretation of the test is more complex than that of the self-boring pressuremeter, because of the influence of the prior cone penetration. An interpretation method for the test in clay has been proposed (Houlsby and Withers, 1988), but interpretation methods for tests in sand have not yet been developed.

A research programme aimed at understanding the cone pressuremeter test in sand is currently in progress at Oxford University. The programme includes large scale calibration chamber tests (Schnaid, 1990), and also finite element analysis of the test. The latter part of this programme is the subject of this chapter. Whilst a comprehensive analysis of the cone pressuremeter test requires a two-dimensional axisymmetric analysis, significant progress can be made by analysing the test as a one-dimensional cavity expansion, and this chapter concentrates on this approach.

As well as developing methods of interpretation of the test in the field, cavity expansion analysis can be used to aid interpretation of the chamber tests. In particular it is

found that the effects of chamber size on cone and pressuremeter tests in chambers can largely be explained by a cavity expansion process.

## 4.2 Verification of the finite element formulation

Before the finite element formulation is used to carry out the analysis of the cone-pressuremeter, it is necessary to validate the numerical formulation by analysing some test problems, for which closed form solutions are available.

The finite element formulation developed in Chapter 3 can be used to predict the limit pressure for cavity expansion, and stress states around the cavity during any stage of expansion. Analytical solutions of pressure-displacement curve for cylindrical and spherical cavity expansion in undrained Tresca materials were obtained by Gibson and Anderson (1961) and Chadwick (1959). In order to avoid unnecessary complication, large strain theory is used in the plastically deforming region and small strain theory is adopted for the outer elastic zone. As soils are characterized by the fact that the rigidity index is very large and the strain to the initiation of plasticity is then small, the use of small strain theory in the elastic region is acceptable for all realistic soil parameters. The generalisation of the results of Gibson and Anderson (1961) to a dilating material has been presented in Chapter 2 using the non-associated Mohr-Coulomb criterion. To investigate the effects of incompressibility on the quality of limit pressure and stress data calculated by the finite element method, the analytical solution is used to verify the numerical formulation for the special case of the cavity expansion in undrained cohesive materials and purely frictional soils without volume change.

For convenience of comparisons, a relative error parameter is defined as follows:

$$ERR = \frac{(P_l^n - P_l^t)}{P_l^t} \times 100\ (\%) \tag{140}$$

where $P_l^n$ and $P_l^t$ denote the predicted limit pressure by the finite element and analytical solution respectively. In the finite element solution for cavity expansion limit pressures presented in this chapter, an expansion ratio of four is applied to the radius of the cavity. As a simple procedure is used for stress update calculations, which does not include the

stress correction at end of the increment, the use of a very small increment is necessary in the analysis in order to obtain a correct solution. The calculation is performed in 6000 displacement increments for expanding the initial cavity radius by a factor of four. In the calculation of the stiffness matrix, both one point Gauss quadrature and two Gauss point quadrature have been used.

The material properties used for the von Mises and Tresca models are: Poisson's ratio $\nu$=0.49, rigidity index $I_r = G/s_u = 100$, in-situ hydrostatic stress $p_0$=0. The theoretical solution for cavity expansion in undrained Tresca materials may be written in an equation with the following form (Gibson and Anderson, 1961; Chadwick, 1959):

$$P_l = \frac{2-m}{3} s_u \left[1 - \ln I_r - \ln\left(1 - \left(\frac{a_0}{a}\right)^{m-1}\right)\right] \tag{141}$$

where $m = 1$ and $m = 2$ represent the cylindrical cavity and spherical cavity respectively; $\frac{a}{a_0}$ denotes the cavity expansion ratio.

For the cylindrical cavity expansion problem, the solution for the von Mises material can also be obtained from the above equation. This can be achieved by using the plane strain undrained shear strength, which is equal to the triaxial undrained shear strength multiplied by a factor of $\frac{2}{\sqrt{3}}$. For spherical cavity expansion, the von Mises and Tresca solutions are the same.

The material properties used for the Mohr-Coulomb model are: Poisson's ratio $\nu$=0.49, the ratio of shear modulus to in-situ hydrostatic stress $G/p_0$=100, dilation angle $\psi$=0, friction angle $\phi = 30^0$. The theoretical solution for the expansion of both cylindrical cavity and spherical cavity in the Mohr-Coulomb material is given by equation ( 56) in Chapter 2.

For the material models with the above properties, 50 two-node elements are used in conjunction with an outer infinite spring element to model cavity expansion in an infinite soil mass.

Table 4.1 Comparisons of The Relative Error Parameters ERR%

| Element | Integration | Cylindrical cavity | | | Spherical cavity | | |
|---|---|---|---|---|---|---|---|
| type | rule | Tresca | Mises | Coulomb | Tresca | Mises | Coulomb |
| Conventional | 1×1 | -0.072 | -0.144 | +0.094 | -0.161 | -0.242 | -0.616 |
| element | 1×2 | $-38.38^{\ddagger}$ | $-33.87^{\ddagger}$ | $-1.200^{\ddagger}$ | $-114.3^{\ddagger}$ | $-114.24^{\ddagger}$ | $-1.988^{\ddagger}$ |
| Proposed | 1×1 | -0.253 | -0.369 | -0.223 | -0.429 | -0.496 | -0.599 |
| element | 1×2 | -0.180 | -0.241 | -0.070 | -0.349 | -0.429 | -0.372 |

‡ failure of the numerical prediction of stress distributions

In Table 4.1 the values of relative error parameter from the numerical study and analytical solutions for different cases are shown. The results suggest that the conventional two node element with two Gauss point integration predicts the limit pressure with lower accuracy for the Mohr-Coulomb material, and fails to predict the limit pressure for both the von Mises and Tresca materials. This procedure also results in poor estimates of the stress states for all these material models. This is reflected by a strong oscillation of the stress distribution in the soil surrounding the cavity. It is interesting to note that the conventional two node element with one point Gauss quadrature could be used to improve the numerical performance for both limit pressure prediction and stress calculations in some cases. The dependence of the performance of the analysis on the number of Gauss points for the conventional two node element may be due to the effects of the incompressibility constraint. By contrast, the proposed two node element has been used successfully for the prediction of the cavity limit pressure and stress states. The result of the analysis using the proposed element is largely independent of the number of Gauss points used in forming the stiffness matrix. All the results presented in this section are in agreement with the argument put forward in Chapter 3 suggesting that the proposed two node element is superior to the conventional one. This conclusion is justified because the proposed element gives a consistent numerical performance with both one and two Gauss point integration rules.

Although several methods have been used in the past in order to reduce the constraints imposed on the nodal velocities by the incompressibility condition, none has been based on the appropriate choice of displacement interpolation to minimise the constraints. When compared to the conventional one-dimensional two node element, the proposed two node element with a non-linear displacement interpolation gives higher accuracy for both cylindrical and spherical problems which involve nearly incompressible behaviour. The new displacement interpolation function described in this chapter has been developed further by the author to suit two-dimensional axisymmetric elastic-plastic problems. Full discussion of this novel two-dimensional finite element formulation will be given in Chapter 5.

## 4.3 Analysis of the cone-pressuremeter

Expansion of a cylindrical cavity in an infinite soil and in a finite soil cylinder has been used to simulate the cone-pressuremeter test in the field and in a laboratory calibration chamber respectively. In this study, an expansion ratio of four is applied to the radius of the cavity, which may be assumed to model numerically the expansion of the cone pressuremeter membrane following installation of the instrument. The calculation is typically performed in 6000 displacement increments.

Experimental results for a cone-pressuremeter in a large calibration chamber show a well defined limit pressure after a cavity strain of approximately 20% (Schnaid and Houlsby, 1990; Schnaid, 1990). Calculations have been carried out to model as closely as possible the conditions for each test, using measured values of soil shear modulus, and friction and dilation angles estimated using the procedure described by Bolton (1986, 1987). The parameters used in the analysis for a total of 28 tests are listed in Table 4.2, with measured and predicted limit pressures. The tests are classified in the same way as Schnaid (1990), where the pressuremeter probe size is given first, followed by the abbreviation of the cone-pressuremeter (CMPT) and finally the test number.

Table 4.2 Prediction of the cone-pressuremeter limit pressure

| Test | $R_d$ | $\sigma_{v0}$ (kPa) | $\sigma_{h0}$ (kPa) | $\phi$ | $\nu$ | G (MPa) | $p_l^m$ (kPa) | $p_l^n$ (kPa) |
|---|---|---|---|---|---|---|---|---|
| 10CPMT02 | 0.27 | -39.60 | -46.60 | 37.68 | 4.23 | 70.1 | 410 | 567 |
| 10CPMT03 | 0.16 | -64.80 | -34.10 | 34.27 | 0.04 | 61.75 | 325 | 366 |
| 10CPMT04 | 0.17 | -89.80 | -96.60 | 33.94 | -0.46 | 85.34 | 750 | 1023 |
| 10CPMT05 | 0.26 | -139.60 | -71.60 | 36.39 | 2.61 | 84.60 | 630 | 833 |
| 10CPMT06 | 0.21 | -189.80 | -196.60 | 34.27 | -0.04 | 113.61 | 1400 | 2110 |
| 10CPMT07 | 0.26 | -49.60 | -116.60 | 36.39 | 2.61 | 95.34 | 830 | 1365 |
| 10CPMT08 | 0.24 | -289.70 | -146.60 | 34.98 | 0.85 | 105.76 | 1090 | 1599 |
| 10CPMT09 | 0.60 | -88.80 | -96.60 | 45.67 | 14.21 | 176.77 | 1490 | 1510 |
| 10CPMT10 | 0.62 | -138.70 | -71.60 | 46.22 | 14.90 | 165.97 | 1310 | 1140 |
| 10CPMT11 | 0.61 | -88.80 | -96.60 | 45.94 | 14.55 | 179.33 | 1500 | 1521 |
| 10CPMT12 | 0.63 | -138.70 | -71.60 | 46.49 | 15.24 | 167.52 | 1310 | 1148 |
| 10CPMT13 | 0.62 | -48.70 | -116.60 | 46.22 | 14.90 | 188.85 | 1600 | 1850 |
| 10CPMT14 | 0.63 | -288.70 | -146.60 | 44.21 | 12.38 | 230.42 | 2080 | 2198 |
| 10CPMT15 | 0.68 | -63.70 | -34.10 | 50.44 | 20.17 | 105.50 | 640 | 604 |
| 10CPMT16 | 0.60 | -188.70 | -196.60 | 43.50 | 11.50 | 246.27 | 2450 | 2888 |
| 10CPMT17 | 0.89 | -63.10 | -34.10 | 56.98 | 28.36 | 136.01 | 790 | 683 |
| 10CPMT18 | 0.83 | -138.10 | -71.60 | 51.96 | 22.07 | 226.71 | 1540 | 1315 |
| 10CPMT19 | 0.86 | -88.10 | -96.60 | 52.77 | 23.09 | 274.07 | 1890 | 1799 |
| 10CPMT20 | 0.85 | -89.10 | -96.60 | 52.49 | 22.41 | 275.67 | 1930 | 1788 |
| 10CPMT21 | 0.84 | -48.10 | -116.60 | 52.23 | 22.41 | 293.27 | 2120 | 2145 |
| 15CPMT02 | 0.88 | -88.10 | -96.60 | 53.32 | 23.78 | 222.76 | 1420 | 1824 |
| 15CPMT03 | 0.67 | -88.80 | -96.60 | 47.58 | 16.60 | 160.08 | 1160 | 1589 |
| 15CPMT04 | 0.23 | -89.80 | -96.60 | 35.57 | 1.59 | 82.20 | 615 | 1089 |
| 15CPMT05 | 0.84 | -88.10 | -96.60 | 52.23 | 22.41 | 219.60 | 1460 | 1777 |
| 05CPMT01 | 0.84 | -63.10 | -34.10 | 55.43 | 26.41 | 173.91 | 1120 | 674 |
| 05CPMT02 | 0.87 | -138.10 | -71.60 | 53.05 | 23.43 | 281.63 | 1930 | 1342 |
| 05CPMT03 | 0.64 | -138.70 | -71.60 | 46.76 | 15.58 | 181.56 | 1460 | 1153 |
| 05CPMT04 | 0.65 | -88.80 | -96.60 | 47.03 | 15.92 | 229.67 | 2050 | 1566 |

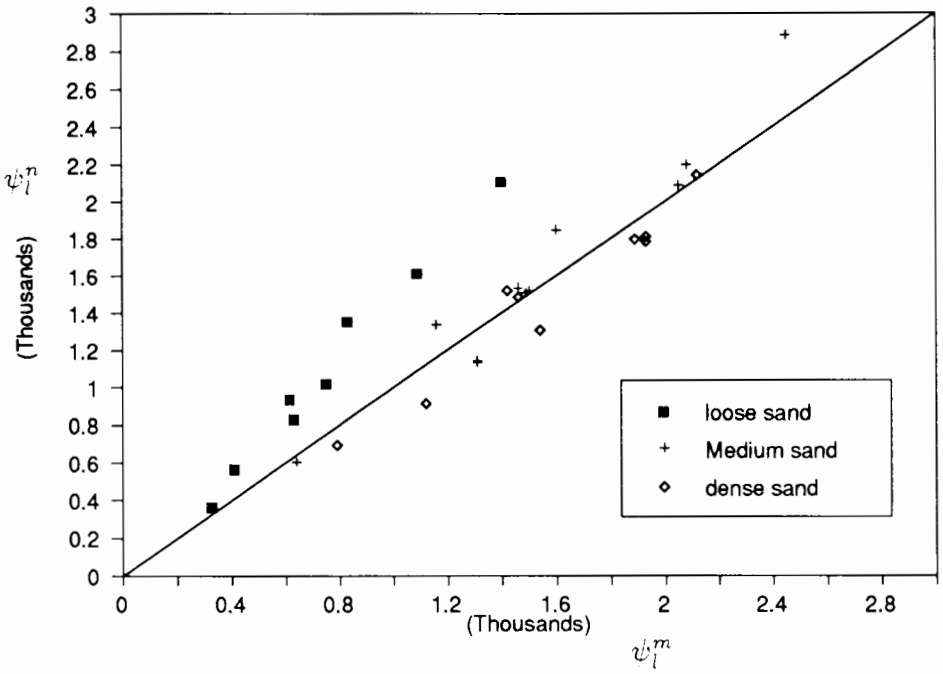


Figure 15: Comparison between measured and calculated limit pressures

For example, 10CPMT02 means a $10cm^2$ cone-pressuremeter test, test number 2. $R_d$ denotes relative density of the sand and $p_l^m, p_l^n$ represent the measured and predicted limit pressures for the cone-pressuremeter test. $\phi, \nu$ are angles of friction and dilation of the sand and $G$ denotes the shear modulus measured from the unloading-reloading loop of the cone-pressuremeter test.

The calculated limit pressures are compared with the measured ones in Figure 15. The slight underprediction of limit pressures for dense sands is almost certainly because the end effects on the actual pressuremeter of finite length result in a higher limit pressure than for an ideal, infinitely long, cavity. Investigations of the effects of the finite length of the pressuremeter are presented in Chapter 6. The overprediction of limit pressure for loose and to a lesser extent for medium sands is probably due to use of slightly too high a friction angle and stiffness in the calculations. Overall the agreement is remarkably good, considering the simplicity of the theoretical model.

The recent analysis of the cone-pressuremeter test in clay suggests that the difficulties in modelling the disturbance caused by installation of the cone-pressuremeter may be

overcome by using the plastic unloading curve from the pressuremeter test to derive the soil parameters (Houlsby and Withers, 1988). The small strain unloading analysis (Houlsby, Clarke and Wroth, 1986) for the Mohr-Coulomb material shows that the plastic unloading slope in a plot of $\ln v$ against $-\ln(\epsilon_{cm} - \epsilon_c)$ is primarily controlled by the soil strength parameters and to a small extent by soil stiffness, where $v$ is the cavity pressure and $\epsilon_{cm}$ and $\epsilon_c$ denote the maximum and current cavity strain. The slope $S_d$ of the unloading curve in this plot may be approximately expressed as a function of the angles of friction and dilation as follows:

$$S_d = -\frac{N - \frac{1}{N}}{N - \frac{1}{n}} \tag{142}$$

where $N = (1 - \sin\phi)/(1 - \sin\varphi)$ and $n = (1 - \sin\nu)/(1 + \sin\nu)$, in which $\phi$ and $\nu$ denote the plane strain friction angle and dilation angle respectively.

This finding has been supported to some extent by the large strain unloading solution developed in Chapter 2. Comparison of the large strain solution and the small strain solution suggests that the small strain unloading analysis developed by Houlsby et al. (1986) may be used to give an approximate solution for large strain contraction of a cavity in sand. This is particularly true for both loose and medium sands. For dense sands, the large strain solution illustrates that the plastic cavity pressure-contraction curve is not in general a straight line on the logarithmic plot, which may suggest that the small strain solution is less satisfactory in approximating the cavity pressure-contraction relationship for the large strain cavity contraction in dense sands. In general, the small strain solution tends to overestimate the plastic unloading slope by few percent for both loose and medium sands. For dense sands, it is found that the small strain analysis may underestimate the large strain plastic unloading slope by more than 10%. The agreement for dense sands may be improved by ignoring the initial portion of the plastic unloading curve in determining the unloading slope. In agreement with the large strain unloading analysis, results of the present large strain finite element analysis using the Mohr-Coulomb yield criterion further confirm that the slope of large strain unloading can be predicted by the small strain solution with a reasonable accuracy. An example of the results of a numerical analysis is plotted as $\ln \frac{v}{p_0}$ against $-\ln(\epsilon_{cm} - \epsilon_c)$ in Figure 16,

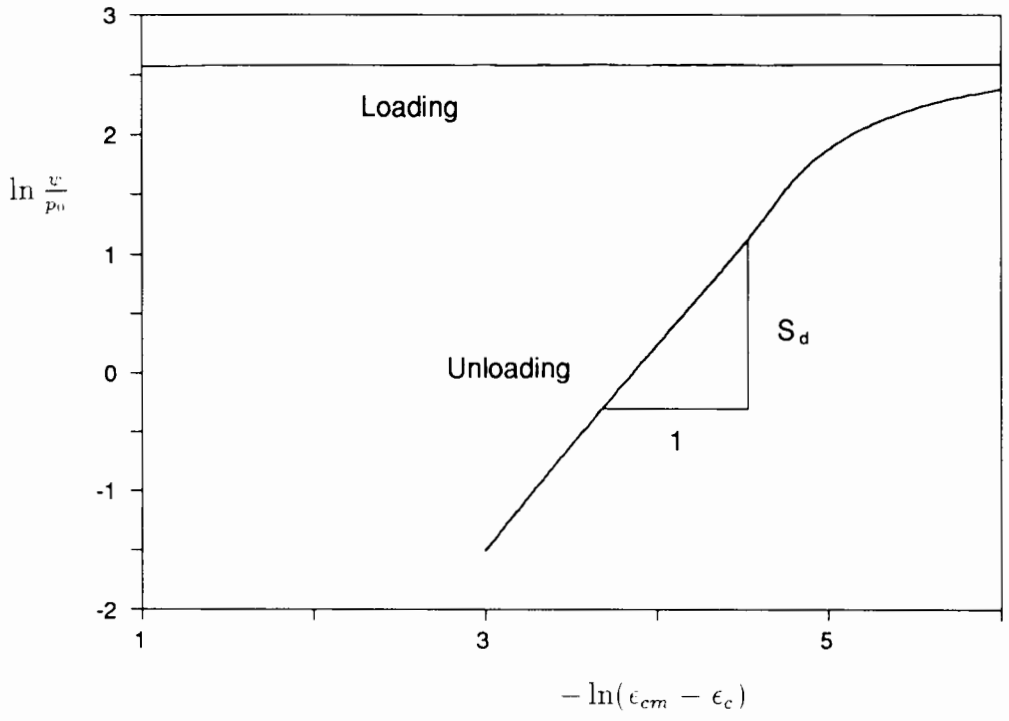


Figure 16: Example of a numerical cavity expansion-contraction curve

showing that a substantial section of the curve is straight in this plot. It is therefore justified to use the simple closed form solution obtained from the small strain theory in highlighting the possibility of deriving strength parameters of a soil from the cone-pressuremeter unloading test results.

Equation (142) is inconvenient in that it involves both the friction and dilation angles. It is convenient to introduce a relationship between these angles, and Rowe's stress dilatancy relationship (Rowe, 1962), which can be written:

$$\sin \nu = \frac{\sin \phi - \sin \phi_{cv}}{1 - \sin \phi \sin \phi_{cv}} \tag{143}$$

is well established empirically, and allows the dilation angle to be eliminated from equation (142), introducing instead the $\phi_{cv}$ value which can be easily determined by independent tests. The result is:

$$\sin \phi = (\sin \phi_{cv} + \frac{1 - \sin \phi_{cv}}{S_d}) - \sqrt{(\sin \phi_{cv} - \frac{1 - \sin \phi_{cv}}{S_d})^2 - 1} \tag{144}$$

The above equation may be used to obtain the soil strength parameters from the in-situ cone-pressuremeter tests in sand. This relationship for different values of critical

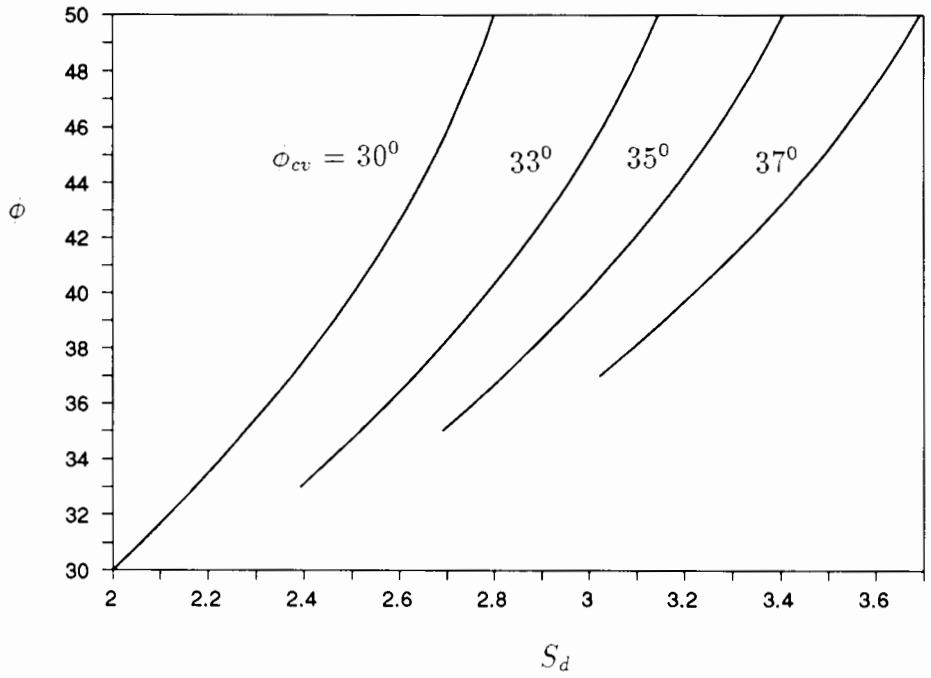


Figure 17: Relationship between friction angle and plastic unloading slope

state friction angle is plotted in Figure 17.

The above relationship has been developed using the assumption that the cone-pressuremeter test can be explained as a cylindrical cavity expansion process. This assumption may be justified either by testing the above proposed correlation using field test data or by comparing the cavity expansion analysis in a finite cylinder with the large calibration chamber test data. The latter approach has been used because of the lack of field data for the cone-pressuremeter test. The numerical analysis has been carried out by using some best estimates of the soil parameters for the chamber tests.

A typical experimental cone-pressuremeter expansion and contraction curve carried out at Oxford by Schnaid is shown in Figure 18 (Schnaid and Houlsby, 1990). A clearly linear unloading curve is defined, which was found generally to be the case for tests on loose sand. For medium and dense sands the slope of the unloading curve on this plot is much less well defined. Although the shape of the theoretical and experimental unloading curves are similar, it is found unfortunately that the $S_d$ values do not compare well. In general the calculated $S_d$ values are significantly higher than those measured, and in any case (apart from for loose sand) there is a significant scatter in the observed $S_d$ values.

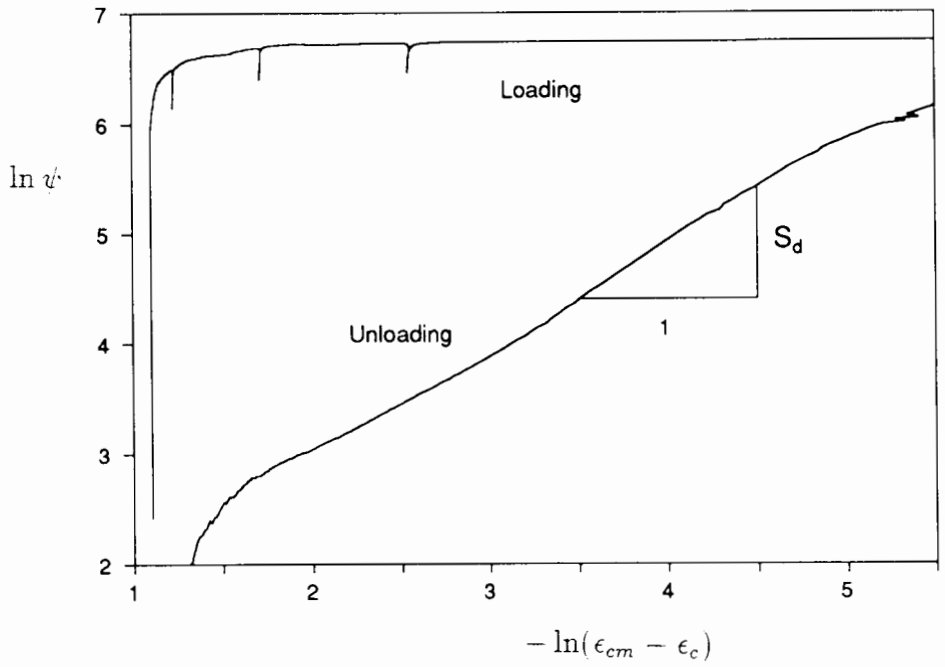


Figure 18: Example of a cone-pressuremeter loading-unloading curve from a chamber test

The disagreement of the calculated $S_d$ values and the measured $S_d$ values may be partly due to the unrealistic modelling of stress-strain behaviour of a soil during unloading. The explanation of these topics deserves further careful investigation.

## 4.4 Estimate of the chamber size effect

One of the aspects of the calibration chamber tests which needs further research is the quantitative estimate of the effects of chamber size on the calibration results. It is usually thought that calibration chamber tests in loose and medium sands represent field conditions reasonably well, but dense tests are significantly effected by the proximity of the chamber boundary (Lunne and Parkin, 1982). Hence, corrections have to be made before applying chamber test results to field conditions.

Based on the assumption that the cone-pressuremeter test can be explained as a cylindrical cavity expansion process, it may be reasonable to suggest that the chamber size effects can be accounted for by considering the difference between the analysis of cavity expansion in an infinite medium and in a finite cylinder. First of all, some insight

into this problem can be gained from cone penetrometer test results. By analysing an extensive database of approximately 400 chamber tests on cone penetrometers carried out in Norway, Italy and the U.K., approximate relationships between the ratio of tip resistance $q_{t50}$ measured in a calibration tank of 50 cone diameters to the $q_{tC_d}$ value in smaller tanks of different diameter ratios $C_d$ have been obtained for different ranges of sand density. In addition, the cone-pressuremeter tests in a large calibration chamber carried out by Schnaid (1990) at Oxford provide some useful experimental data regarding to the chamber size effect on the cone-pressuremeter limit pressure $p_l$. Schnaid's results suggest that the chamber size has a very significant effect on the observed pressuremeter limit pressure for both medium and dense sands. No significant difference of the magnitude of the chamber size effect is observed for medium and dense sands. In other words, the chamber size effects for the tests on medium sand and the tests on dense sand are very similar. No general conclusion for loose sand can be drawn, mainly because few tests have been carried out on loose sand.

A comparison is made between the magnitude of the effect predicted by cavity expansion analysis, and the observed chamber diameter effect on the cone and the cone-pressuremeter tests. This comparison is based on the hypothesis that cone penetration resistance and the cone-pressuremeter limit pressuremeter are controlled, at least in part, by a cavity expansion process. In the calculations, an isotropic initial stress state is assumed. The values of the stiffness index ($\frac{G}{\sigma_{h0}}$) of 500, 1000 and 3000 are used to represent loose, medium and dense sands respectively. Similarly, the friction angle $\phi$ is given the values of $33^0, 42^0$ and $53^0$ for loose, medium and dense sands respectively. In addition, the critical state friction angle is assumed to equal $33^0$ and dilation angle $\psi$ is obtained from Rowe's stress-dilatancy equation.

Figure 19 shows the comparison of these ratios with the ratios calculated for the cylindrical cavity expansion limit pressure, using large strain analysis. The calculations show that a chamber diameter effect would be expected even for loose sands, with an increase in the magnitude of the effect for medium and dense sands. Because of the many different factors which can affect chamber tests (sand density, stiffness, and particle size as well as cone and chamber size), it is difficult to separate out the effect solely of the

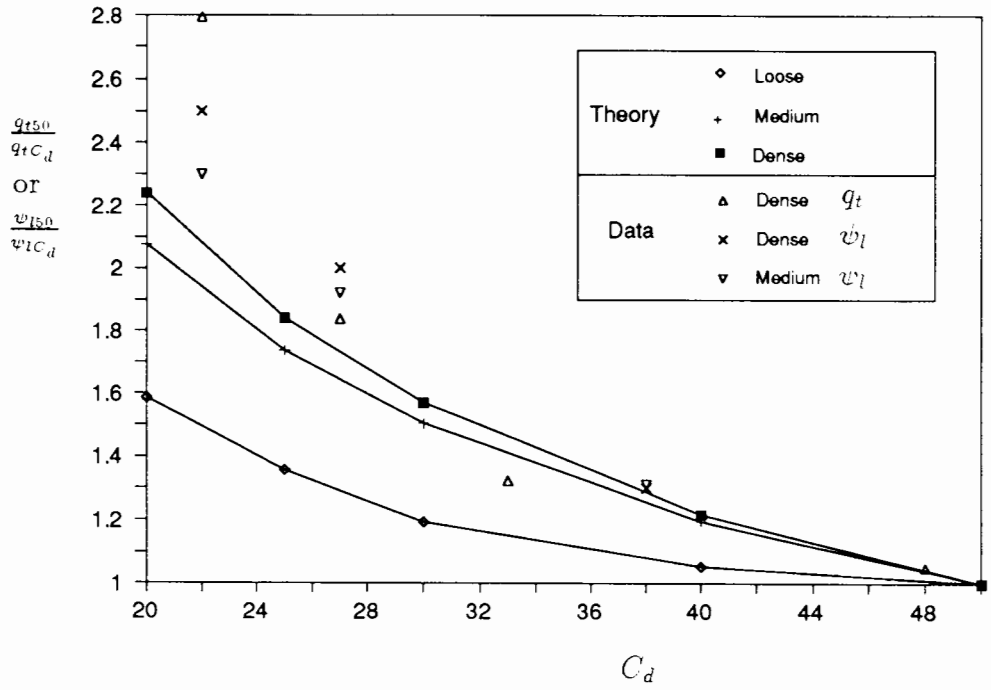


Figure 19: Comparisons between the numerical predictions and test results of chamber size effect

chamber to cone size. However, the experimental results seem to indicate only a very small effect for chamber to cone diameter ratios greater than 20 for loose sand, but a more significant effect for medium and dense sands. The experimental points for medium and dense sands shown in Figure 19 are approximate only and deduced from a large number of rather scattered test data.

For medium and dense sands the boundary effects of small chambers seem to be slightly greater than indicated by the calculations. These comparisons do, however, give some confidence that cavity expansion analysis could be used to improve the interpretation of cone and pressuremeter tests in calibration chambers. A similar approach was successfully used by Jewell, Fahey and Wroth (1980).

## 4.5 Conclusions

A relatively simple approach based on cavity expansion theory has been developed to perform an analysis of the cone-pressuremeter test both in the field and in a calibration

chamber. The proposed method uses large strain theory with a novel finite element formulation which is able to minimize the excessive constraints caused by the incompressibility and constant dilation rate conditions.

Calculations of limit pressures agree well with observed values in a large calibration chamber, except that for loose sands the limit pressure is overestimated, probably due to the use of a too high friction angle.

In field conditions, a semi-analytical correlation between the soil strength parameters $(\varphi, \nu)$ and the cone-pressuremeter plastic unloading slope $S_d$ has been proposed based on analyses using a large strain cavity expansion model. The application of this correlation to field problems must be considered with caution because verification of the proposed correlation using field test data is still required. Quantitative agreement between analyses and laboratory test results is not good.

Together with an extensive database of more than 400 tests, the proposed numerical method has been used to quantify the chamber size effects. The comparison between the analysis and test data is encouraging, indicating that the assumption that both penetration pressures and the cone-pressuremeter limit pressures are controlled by a cavity expansion process can at least in part explain observed chamber size effects.

# Chapter 5

# Large Strain Finite Element Formulation for Two Dimensional Axisymmetric Problems

## 5.1 Introduction

In deriving shear strength from pressuremeter tests in clay, the rate of installation and expansion is generally considered to be sufficiently fast to give rise to undrained conditions. The constant dilation rate condition is commonly assumed for interpreting self-boring pressuremeter tests in cohesionless soils. In both of these conditions, the soil behaves as either incompressible or with a constant volume change rate. These features must be considered in developing the finite element formulation.

When analysing the cone-pressuremeter test, where a large displacement may need to be reached during the test, it is important to take into account large strain effects in the formulation of finite element equations in order to obtain a correct solution. For this case, where large displacement and large soil rotations are involved, care should be taken in choosing the stress rate definition.

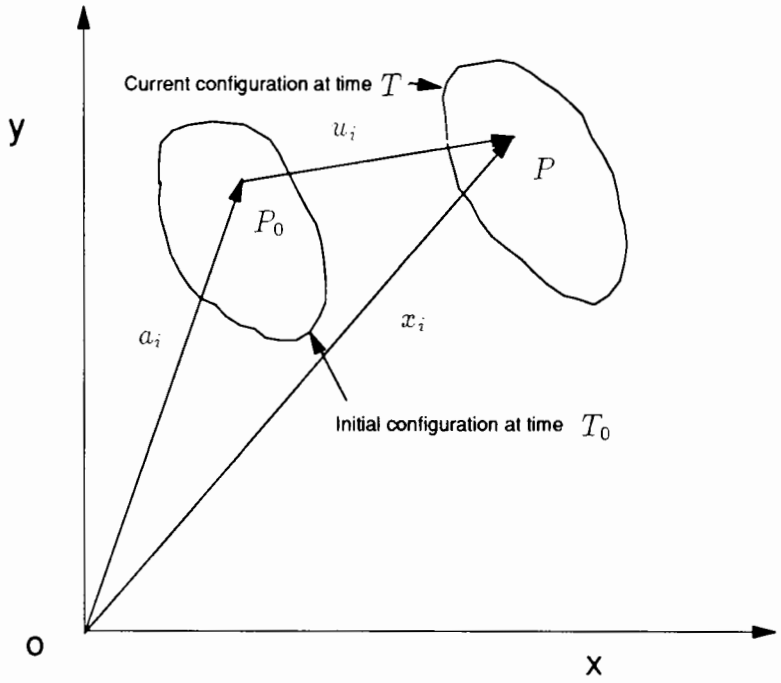


Figure 20: Description of kinematics

## 5.2 Consideration of large displacement analysis

### 5.2.1 Description of kinematics

In the infinitesimal theory of elastic-plastic deformations, it is possible to define strain in a unique and unambiguous way. This is not true when the deformations are large, however, since a variety of co-ordinate systems may be used which will inevitably result in different strain definitions. In continuum mechanics, the deformation of a body subjected to large displacements is usually described by either a Lagrangean or an Eulerian reference system.

Consider a body subjected to large displacements as illustrated in Figure 20. The motion begins at time $t = T_0$ and ends at time $t = T$. At a given time $T_0$, the position of a typical material point, $P_0$, in the deforming body is described by the co-ordinate vector, $a_i$, relative to some fixed reference. At time $T$, the same material point has moved to position $P$, which is described by the vector, $x_i$, in the same reference frame.

In the Lagrangean description, the co-ordinate vector $x_i$ is related to $a_i$ in an equation of the form:

$$x_i = x_i(a_i, t) \tag{145}$$

and this approach lends itself to a description of the deformation in terms of the Green-Lagrange strain, which is given by the expression:

$$E_{ij} = \frac{1}{2}\left[\frac{\partial x_k}{\partial a_i}\frac{\partial x_k}{\partial a_j} - \delta_{ij}\right] \tag{146}$$

where $\delta_{ij}$ is the Kronecker delta.

An alternative to the Lagrangean approach is the Eulerian description which, although currently less popular than the Lagrangean formulation, can sometimes lead to simpler forms of the finite element equations. The basis of the Eulerian approach is to consider the velocity of a material point, $u_i$ , in the current configuration, to be related to the co-ordinate of the material point, $x$, and the time $t$ in a relationship of the form:

$$u_i = u_i(x_i, t) \tag{147}$$

The deformation of the material is described by the rate of deformation tensor defined as:

$$d_{ij} = \frac{\partial u_i}{\partial x_j} \tag{148}$$

These two kinematical descriptions have both been used in finite element analysis of large strain problems (Hibbitt et al., 1970; Carter et al., 1977; Osias and Swedlow, 1974; McMeeking and Rice, 1975). The choice of kinematic description depends mainly on the form of the material behaviour that is being modelled, but may be influenced by the ease with which the appropriate material properties can been measured and, to a certain extent, on personal preference. The Lagrangean approach is best suited to those problems where the constitutive law may be written in terms of the total deformation of the material and therefore lends itself to the description of materials with a natural reference state. The Eulerian description, however, is well suited to the analysis of material for which the constitutive laws are conveniently expressed in terms of stress and strain rates, as is

often the case in Soil Mechanics. It is for this reason that the Eulerian description has been adopted in this thesis for developing finite element formulations.

### 5.2.2 Objective stress rates

For a mathematical description of material behaviour to be consistent within the framework of continuum mechanics, it is necessary that the stress rate used in the constitutive equation should be 'objective'. This condition requires that the stress rate must vanish under conditions of rigid body motion.

It may be shown (Prager, 1961) that the definition of 'objectivity' is not sufficiently restrictive to give a unique definition of stress rate. As a result, several different 'objective' stress rates have been proposed (Jaumann, 1911; Truesdell, 1953; Oldroyd, 1950). Amongst these, the Jaumann definition has been almost universally adopted for use in large strain computations in recent years. This popularity stems from the desirable feature of the Jaumann definition that vanishing of the stress rate implies stationary behaviour of the stress invariants.

In spite of the fact that the Jaumann stress rate may give rise to physically unrealistic solutions to problems where shear strains become very large (Dienes, 1979), the original form of the Jaumann stress rate, as defined by:

$$\overset{\circ}{\sigma}_{ij} = \dot{\sigma}_{ij} - \sigma_{ik}\dot{\omega}_{jk} - \sigma_{jk}\dot{\omega}_{ik} \tag{149}$$

has been adopted in this study, since the shear strains expected in the analysis are not sufficiently large to justify the additional complexity of any modification. The superior dot denotes the Cauchy stress rate, and $\dot{\omega}_{ij}$ is the skew-symmetric spin tensor:

$$\dot{\omega}_{ij} = \frac{1}{2}\left(\frac{\partial \dot{u}_i}{\partial x_j} - \frac{\partial \dot{u}_j}{\partial x_i}\right) \tag{150}$$

## 5.3 Incompressibility constraint

A particularly comprehensive analysis of the difficulties associated with finite element calculations in the fully plastic range was given by Nagtegaal et al.(1974). Having identified

the detrimental effect of incompressibility constraints, they proposed a criterion which must be satisfied if the finite element analysis is to yield a satisfactory solution. This criterion, which is based on a limiting mesh consisting of an infinite number of elements of identical type, requires that the number of degrees-of-freedom in an element must be greater than the number of constraints imposed by the incompressibility condition. They further showed that for plane strain problems, only a few of the classical lower order elements are able to meet this requirement, while for axisymmetric problems the situation appeared to be much worse, as none of the common lower order elements would be able to predict collapse loads accurately. To obviate this problem, they proposed an approach in which the volumetric strain rates and the nodal velocities are admitted as independent variables and different geometric expansions are used for each of these variables. Later this approach was applied to undrained Soil Mechanics problems by Toh and Sloan (1980).

As an extension to the analysis for the limiting mesh, Sloan and Randolph (1982) also analysed the necessary conditions for a mesh consisting of a finite number of elements to be suitable for collapse load calculations. This analysis has shown that the suitability of any finite element mesh is governed by the number of degrees-of-freedom per constraint for an element. When the number of degrees-of-freedom per constraint for an element is greater than unity, most meshes generated will be suitable for limit load calculations. The reverse is true when the number of degrees-of-freedom per constraint is less than unity. When the number of degrees-of-freedom per constraint is equal to unity, it has been demonstrated that at least half of the boundary degrees-of-freedom must be left unrestrained in order to satisfy the criterion. They have shown that this criterion can be satisfied by the use of higher order elements. This is because as the order of an element is increased, the number of degrees-of-freedom per element increases faster than the number of incompressibility constraints. According to Sloan (1981), the lowest order of triangular element suitable for this approach for axisymmetric problems is the cubic strain element. Although this approach works well, it suffers from the drawback that due to the large bandwidth in the stiffness matrix caused by higher order elements, some sophisticated techniques (e.g. the frontal equations solver) must be employed, with penalties on higher

costs.

An alternative approach which has been widely used to obviate the problems caused by the incompressibility constraints is the so-called Reduced Integration Method (Zienkiewicz et al., 1971: Malkus and Hughes, 1978). The idea of this approach is to use a limited number of sampling points in evaluating the element matrices and load vectors. One major effect of this method is to decrease the number of incompressibility constraints on the nodal velocities. This is clearly seen by noting that the maximum number of constraints per element must be less than, or equal to, the total number of integration points used in forming the element stiffness matrices. A theoretical justification for using Reduced Integration in a nearly incompressible displacement formulation has been given by Malkus and Hughes (1978). They proved that displacement formulations with Reduced Integration are in certain cases equivalent to mixed formulations (i.e. formulations in which the finite element discretization is based on the use of mixed variable types). This equivalence typically holds in plane strain and three dimensional analysis, however, it breaks down for the case of axisymmetry. In addition, it has been shown (de Borst and Vermeer, 1984) that in problems in which, besides the kinematic constraints of incompressibility, many geometric constraints are present (e.g. the deep cone penetration with a rigid, rough shaft, and a rough tip), the Reduced Integration approach may result in inaccurate solutions.

A further effect that can be used to advantage, but has received little attention in the past, is that the number of incompressibility constraints may be reduced by choosing appropriate displacement interpolation functions. An example of this type of approach for one-dimensional problems is given in Chapter 3.

In this chapter, the theoretical criterion originally developed by Nagtegaal et al.(1974) has been used to assess the suitability of a particular displacement interpolation function when it is to be used with any constitutive law which attempts to enforce the constant volume condition at failure. After a detailed theoretical study of the influence of the displacement interpolation function on the number of the incompressibility constraints, a novel displacement interpolation function with a six-noded triangular element is found to be able to satisfy the *Nagtegaal* criterion in axisymmetry. Based on the proposed

displacement interpolation function and the concept of isoparametric elements, two alternative new displacement finite element formulations are developed.

## 5.4 Suitability of the proposed displacement interpolation function

According to the criterion of Nagtegaal et al.(1974), it is necessary to determine the number of degrees-of-freedom per constraint for the limiting case of a very fine mesh in order to ascertain whether a particular element assemblage is suitable for accurate elastic-plastic analysis. The number of degrees-of-freedom per constraint is defined as the ratio of degrees-of-freedom to constraints for an element. A general procedure for determining this ratio for any given element type has been described in detail by Sloan and Randolph (1982).

Following this procedure, the conventional six-noded triangular element is used to demonstrate that an analysis of axisymmetric constraint problems is more difficult than that of plane strain problems. It is then shown how the conventional six-noded triangular element can be modified for an elastic-plastic analysis under axisymmetric loading.

Consider a body, loaded under plane strain or axisymmetric conditions, which is discretized arbitrarily using elements of identical type. The number of degrees-of-freedom per element is:

$$m_e = \frac{1}{\pi} \sum_{i=1}^{n} \theta_i^e \tag{151}$$

where $\theta_i^e$ denotes internal angle for node $i$ of element $e$; $n$ is the number of nodes per element.

Equation ( 151) was first derived by Nagtegaal et al.(1974) and thought to be only correct for straight-sided elements. Later Sloan and Randolph (1982) showed that the equation is also true for a grid with curved boundaries provided a relatively fine mesh discretization is used.

Figure 21 shows a conventional six-noded triangular element with straight sides. The

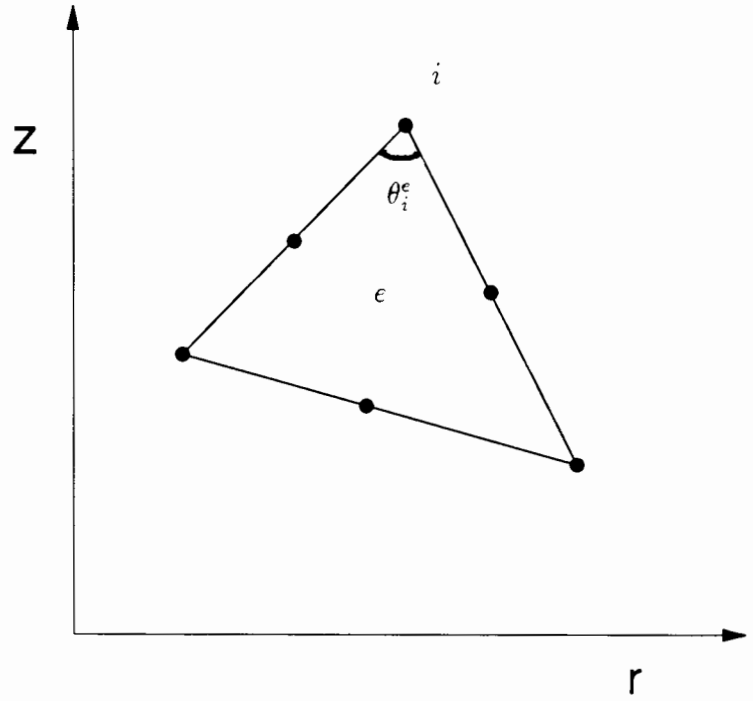


Figure 21: A six-noded triangle element

displacement increments within each element are usually expressed as:

$$\dot{u} = \dot{r} = c_1 + c_2 r + c_3 z + c_4 r^2 + c_5 rz + c_6 z^2 \tag{152}$$

$$\dot{v} = \dot{z} = c_7 + c_8 r + c_9 z + c_{10} r^2 + c_{11} rz + c_{12} z^2 \tag{153}$$

where $\dot{u}$ and $\dot{v}$ denote velocities in $r$ and $z$ directions respectively; and the $c_1, \ldots, c_{12}$ are unknown coefficients which are functions of nodal velocities and coordinates only.

For plane strain conditions, the incompressibility condition is given by:

$$\frac{\partial \dot{u}}{\partial r} + \frac{\partial \dot{v}}{\partial z} = 0 \tag{154}$$

Differentiating equations ( 152)-( 153) and inserting into equation ( 154) results in:

$$(c_2 + c_9) + (2c_4 + c_{11})r + (2c_{12} + c_5)z = 0 \tag{155}$$

In evaluating the element stiffness matrix, the incompressibility condition, represented by equation ( 155), needs to be satisfied at all Gauss sampling points. For the six-noded triangular element, three and six points Gaussian quadrature is often used for plane strain

and axisymmetric loading respectively. This order of numerical integration corresponds to what is commonly denoted by the term 'Full-Integration' (Laursen and Gellert, 1978). In general, the constant volume condition which requires equation ( 155) to be satisfied at three or more integration points for plane strain finite element calculations only imposes a maximum of three independent constraints on the $c_i$, namely:

$$2c_{12} - c_5 = 2c_4 - c_{11} = c_2 - c_9 = 0 \tag{156}$$

Using equations ( 151) and ( 156), it is now possible to ascertain whether the conventional six-noded triangular element is suitable for plane strain elastic-plastic analysis. For this element $m_\epsilon$ is equal to four in equation ( 151) and hence, as the finite element mesh is refined, the number of degrees-of-freedom per element tends to approach four. From equation ( 156) we can see that for plane strain problems the incompressibility condition imposes three independent constraints upon the nodal velocities per element. Therefore, in the limit, the number of degrees-of-freedom per constraint is equal to $\frac{4}{3}$, which is greater than unity. Hence the conventional six-noded triangular element is deemed to be generally suitable for plane strain elastic-plastic analysis.

For the case of an axisymmetric analysis, the constant volume condition is given by:

$$\frac{\partial \dot{u}}{\partial r} + \frac{\dot{u}}{r} + \frac{\partial \dot{v}}{\partial z} = 0 \tag{157}$$

Substituting equations ( 152) and ( 153) into equation ( 157) results in the following incompressibility condition:

$$(2c_2 - c_9) + (3c_4 - c_{11})r + (2c_5 + 2c_{12})z - c_1\frac{1}{r} + c_3\frac{z}{r} + c_6\frac{z^2}{r} = 0 \tag{158}$$

If six point integration (conventionally referred to as 'Full-Integration') is used then the constant volume condition, represented by equation ( 158), imposes six independent constraints on the nodal velocities:

$$2c_2 + c_9 = 3c_4 + c_{11} = 2c_5 + 2c_{12} = c_1 = c_3 = c_6 = 0 \tag{159}$$

For axisymmetric conditions, equations ( 151) and ( 159) reveal that the limiting ratio of degrees-of-freedom to constraints is equal to $\frac{2}{3}$ which is less than unity. As a result, the element is thought to be generally unsuitable for finite element analyses of axisymmetric problems of elastic-plastic deformation.

Comparing the constant volume condition equation ( 154) for plane strain and equation ( 157) for axisymmetric conditions, it may be seen that the three additional constraints imposed in the axisymmetric formulation are caused by the additional hoop strain term. These additional constraints may be removed if the formulation is based on the generalized radial coordinate $R$ and its velocities $\dot{R}$ which satisfy the following condition:

$$\frac{\partial \dot{R}}{\partial R} = \frac{\partial \dot{u}}{\partial r} + \frac{\dot{u}}{r} = \frac{\partial \dot{r}}{\partial r} + \frac{\dot{r}}{r} \tag{160}$$

The incompressibility condition, equation ( 157), for axisymmetric cases may now be cast in the same form as the incompressibility condition equation ( 154) for plane strain:

$$\frac{\partial \dot{R}}{\partial R} + \frac{\partial \dot{z}}{\partial z} = 0 \tag{161}$$

If the formulation is based on the use of a quadratic expansion for the velocities, then:

$$\dot{R} = c_1 + c_2 R + c_3 z + c_4 R^2 + c_5 Rz + c_6 z^2 \tag{162}$$

$$\dot{z} = c_7 + c_8 R + c_9 z + c_{10} R^2 + c_{11} Rz + c_{12} z^2 \tag{163}$$

If equations ( 162) and ( 163) are substituted into equation ( 161) then it may easily be shown that the number of incompressibility constraints is three, rather than the six that are obtained using the conventional displacement formulation. Equation ( 160) can be solved to give solutions for $R$ and $\dot{R}$ as follows:

$$R = r^2 \tag{164}$$

$$\dot{R} = 2\dot{r}r = 2\dot{u}r \tag{165}$$

In conclusion, the above analysis suggests that under plane strain conditions, the conventional six-noded triangular element can be used to furnish accurate solutions for

elastic-plastic analysis, provided it is used in a mesh which is sufficiently fine, as this element provides more degrees of freedom than the constraints imposed by the incompressibility condition. However, for axisymmetric loading the conventional six-noded triangular element fails to satisfy the criterion of Nagtegaal et al.(1974), and is unsuitable for elastic-plastic analysis. It has been shown that the six-noded triangular with the modified displacement interpolation function, as defined by equations ( 162)-( 165), can be used to meet the requirement that the limiting number of degrees-of-freedom per constraint must exceed unity in axisymmetric conditions.

The analysis presented so far is limited to the use of straight-sided six-noded triangles for finite element calculations based on any constitutive model which enforces the constant volume condition. However, it is evident that similar problems of over-constraint caused by constant dilation rate conditions will arise when using the conventional displacement formulations together with frictional-dilational plasticity models. The arguments for determining the suitability of an element for nearly incompressibility analysis may also be adopted to assess the suitability of an element for dilational materials (Sloan, 1981). Although an extension of the theory to a dilational material is not presented in this thesis, numerical examples will be given later to investigate the performance of the proposed six-noded element used for elastic-plastic axisymmetric analysis of a Matsuoka material.

Although the assumption of straight-sided triangular elements is reasonable for many problems, it is not true in some cases (e.g. large displacement analysis). It is therefore necessary to study the effect of curved-sided triangular elements on the analysis for the suitability of straight-sided elements presented in this section. The detailed discussion of this effect will be given in a later section.

## 5.5 Finite element formulation based on modified primary variables

The new velocity expansion function, as defined by equations ( 162)-( 165), has been proved to be suitable for general elastic-plastic analysis under axisymmetric conditions.

Based on this expansion, two alternative approaches may be used to form an isoparametric displacement finite element formulation. Firstly, in order to implement the new velocity expansion, we can adopt the velocity of the generalized radial coordinate, $\dot{R}$, as an independent variable and the conventional axial velocity $\dot{z}$ as another basic variable. Then application of the principle of virtual displacement to an element in the original coordinates $(r, z)$ may be expressed purely in terms of the variables defined in the generalized coordinates $(R, z)$. It should be noted that the new formulation based on the generalised coordinates is valid for elements of an arbitrary order but it is illustrated with reference to the six-noded triangle in this thesis. As a result, a finite element formulation based on the generalized coordinates $(R, z)$ can be formed simply by applying the principle of virtual displacement. In the second approach, the primary variables $[\dot{u}, \dot{v}]^T$ are left unchanged but modifications are made to the element shape functions.

This section is devoted to a description of the first of these two approaches.

### The Strain Rate - Velocity Relationship

Figure 22 shows an isoparametric six-noded triangular element, $\epsilon$, plotted in the original coordinate $(r, z)$, the generalized coordinates $(R, z)$ and the area coordinates $(\alpha, \beta)$ which correspond to the element $\epsilon$ in the generalized coordinates.

The velocity field vector, $\mathbf{u_m}$, is defined :

$$\mathbf{u_m} = [\dot{R}, \dot{z}]^T = [2\dot{u}r, \dot{v}]^T \tag{166}$$

the strain rate vector may be written in terms of the velocity vector :

$$\dot{\epsilon} = [\dot{\epsilon_{rr}}, \dot{\epsilon_{zz}}, \dot{\epsilon_{\theta\theta}}, \dot{\gamma_{rz}}, 2\dot{\omega}]^T = \mathbf{L}\mathbf{u_m} \tag{167}$$

where the linear operator matrix $\mathbf{L}$ is defined:

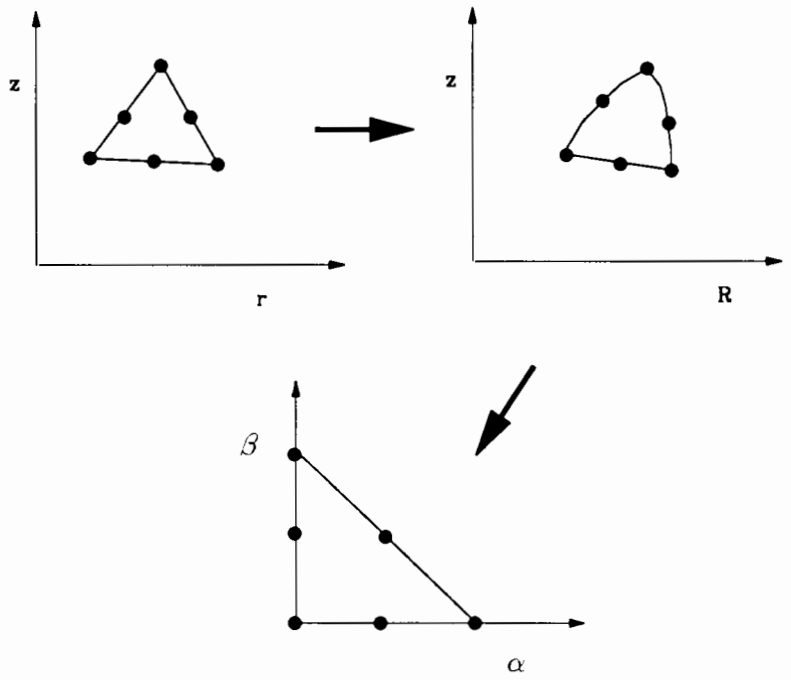


Figure 22: Mapping of an isoparametric six-noded triangular element

$$\mathbf{L} = \begin{bmatrix} \frac{\partial}{\partial R} - \frac{1}{2R} & 0 \\ 0 & \frac{\partial}{\partial z} \\ \frac{1}{2R} & 0 \\ \frac{1}{2\sqrt{R}}\frac{\partial}{\partial z} & 2\sqrt{R}\frac{\partial}{\partial R} \\ \frac{1}{2\sqrt{R}}\frac{\partial}{\partial z} & -2\sqrt{R}\frac{\partial}{\partial R} \end{bmatrix} \tag{168}$$

**The Strain Rate - Nodal Velocity Matrices**

The nodal velocity vector, $\mathbf{a_m^e}$, is defined :

$$\mathbf{a_m^e} = [2\dot{u}_1 r_1, \dot{v}_1 \ldots 2\dot{u}_6 r_6, \dot{v}_6]^T \tag{169}$$

The nodal velocity vector is related to the velocity field vector by :

$$\mathbf{u_m} = \mathbf{N}\mathbf{a_m^e} \tag{170}$$

where $\mathbf{N}$, the shape function matrix, contains the conventional quadratic shape functions written in the area coordinates:

$$\mathbf{N} = \begin{bmatrix} N_1 & 0 & N_2 & 0 & \dots & N_6 & 0 \\ 0 & N_1 & 0 & N_2 & \dots & 0 & N_6 \end{bmatrix} \tag{171}$$

where

$$N_1 = 2(\alpha + \beta - 1)(\alpha + \beta - \frac{1}{2}) \tag{172}$$

$$N_2 = 2\alpha(\alpha - \frac{1}{2}) \tag{173}$$

$$N_3 = 2\beta(\beta - \frac{1}{2}) \tag{174}$$

$$N_4 = -4\alpha(\alpha + \beta - 1) \tag{175}$$

$$N_5 = 4\alpha\beta \tag{176}$$

$$N_6 = -4\beta(\alpha + \beta - 1) \tag{177}$$

The strain rate vector is given by:

$$\dot{\epsilon} = \mathbf{L}\mathbf{u}_\mathbf{m} = \mathbf{L}\mathbf{N}\mathbf{a}^\mathbf{e}_\mathbf{m} = \mathbf{B}\mathbf{a}^\mathbf{e}_\mathbf{m} \tag{178}$$

where

$$\mathbf{B} = \mathbf{L}\mathbf{N} = \begin{bmatrix} \frac{\partial N_1}{\partial R} - \frac{N_1}{2R} & 0 & \dots & \frac{\partial N_6}{\partial R} - \frac{N_6}{2R} & 0 \\ 0 & \frac{\partial N_1}{\partial z} & \dots & 0 & \frac{\partial N_6}{\partial z} \\ \frac{N_1}{2R} & 0 & \dots & \frac{N_6}{2R} & 0 \\ \frac{\partial N_1}{2\sqrt{R}\partial z} & 2\sqrt{R}\frac{\partial N_1}{\partial R} & \dots & \frac{\partial N_6}{2\sqrt{R}\partial z} & 2\sqrt{R}\frac{\partial N_6}{\partial R} \\ \frac{\partial N_1}{2\sqrt{R}\partial z} & 2\sqrt{R}\frac{\partial N_1}{\partial R} & \dots & \frac{\partial N_6}{2\sqrt{R}\partial z} & 2\sqrt{R}\frac{\partial N_6}{\partial R} \end{bmatrix} \tag{179}$$

### The Nodal Force - Nodal Velocity Relationship

The application of the principle of virtual displacement to an element in the original coordinates $(r, z)$ can be used to give the following nodal force - nodal velocity relationship, which may be expressed in terms of the variables in the generalized coordinates $(R, z)$ as follows:

$$\mathbf{P}_{\mathbf{m}}^{\mathbf{e}} = \pi \int \int_{V^e} \mathbf{B}^{\mathbf{T}} \sigma dR dz \tag{180}$$

Equation ( 180) can be transformed using the reference coordinates $(\alpha, \beta)$ into:

$$\mathbf{P}_{\mathbf{m}}^{\mathbf{e}} = \pi \int \int_{V^e} \mathbf{B}^{\mathbf{T}} \sigma det J d\alpha d\beta \tag{181}$$

The rate form of the above equation may be shown to be:

$$\dot{\mathbf{P}}_{\mathbf{m}}^{\mathbf{e}} = \pi \int \int_{V^e} \mathbf{B}^{\mathbf{T}} \dot{\sigma} det J d\alpha d\beta + \pi \int \int_{V^e} (\mathbf{B}^{\mathbf{T}} \dot{det} J) \sigma d\alpha d\beta \tag{182}$$

where

$$\dot{\mathbf{P}}_{\mathbf{m}}^{\mathbf{e}} = [(\pi p_h, 2\pi r p_v)_1 ... (\pi p_h, 2\pi r p_v)_6]^T \tag{183}$$

in which $p_h$ and $p_v$ are nodal force increments per unit length in radial and axial directions respectively.

The relationship between the Jaumann stress rate and the total strain rate may be expressed as:

$$\hat{\sigma} = [D]^{ep} \dot{\epsilon} \tag{184}$$

where the elastic-plastic matrix $[D]^{ep}$ was defined in Chapter 3 for the case of perfect plasticity.

By using the definition of the Jaumann stress rate, which can be written in the following form for axisymmetry:

$$\hat{\sigma} = \dot{\sigma} - [R]\dot{\epsilon} \tag{185}$$

where

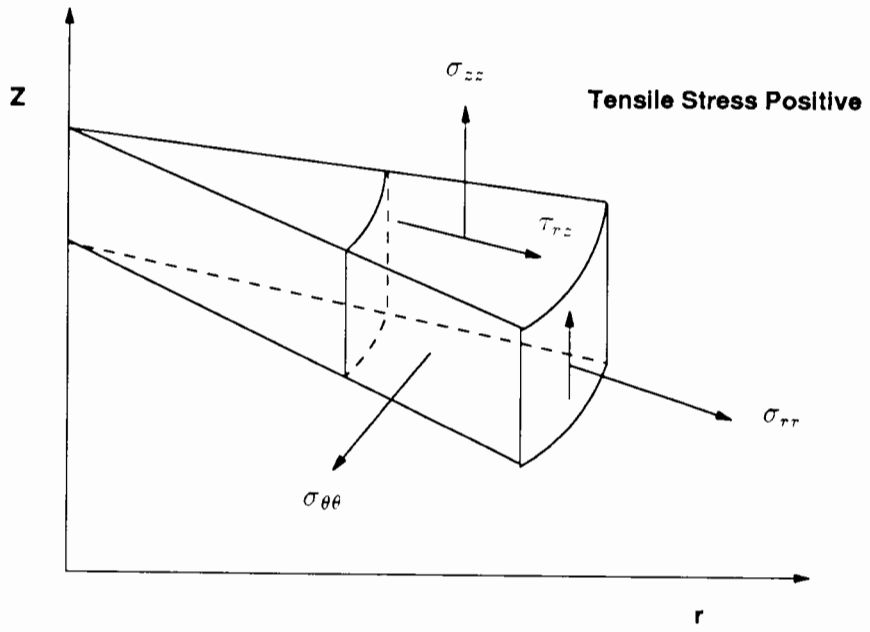


Figure 23: Definition of stresses in axisymmetric geometry

$$[R] = \begin{bmatrix} 0 & 0 & 0 & 0 & \tau_{rz} \\ 0 & 0 & 0 & 0 & -\tau_{rz} \\ 0 & 0 & 0 & 0 & 0 \\ 0 & 0 & 0 & 0 & \frac{\sigma_{zz}-\sigma_{rr}}{2} \\ 0 & 0 & 0 & 0 & 0 \end{bmatrix} \tag{186}$$

and

$$\sigma = [\sigma_{rr}, \sigma_{zz}, \sigma_{\theta\theta}, \tau_{rz}, 0]^T \tag{187}$$

the equation relating the Cauchy stress rate to the total strain rate may be obtained as:

$$\dot{\sigma} = ([D]^{ep} - [R])\dot{\epsilon} \tag{188}$$

The Cauchy stresses for the axisymmetric problem are defined graphically in Figure 23.

Substituting the above stress-strain relationship into equation ( 182) leads to:

$$\dot{\mathbf{P}}^{\mathbf{e}}_{\mathbf{m}} = \mathbf{K}\mathbf{a}^{\mathbf{e}}_{\mathbf{m}} \tag{189}$$

where

$$\mathbf{K} = \pi \int\int_{V^e} \mathbf{B}^{\mathbf{T}}([D]^{ep} - [R])\mathbf{B} detJ d\alpha d\beta - \pi \int\int_{V^e} \mathbf{C} d\alpha d\beta \tag{190}$$

in which

$$\mathbf{C}\mathbf{a}^{\mathbf{e}}_{\mathbf{m}} = (\mathbf{B}^{\mathbf{T}}\dot{\mathbf{detJ}})\sigma \tag{191}$$

By expanding the above equation, we may obtain:

$$\mathbf{C} = \begin{bmatrix} C_{1,1} & C_{1,2} & \dots & C_{1,12} \\ C_{2,1} & C_{2,2} & \dots & C_{2,12} \\ & & & \\ & & & \\ & & & \\ C_{12,1} & C_{12,2} & \dots & C_{12,12} \end{bmatrix} \tag{192}$$

in which

$$C_{2i-1,2j-1} = \frac{(\sigma_{rr} - \sigma_{\theta\theta})N_i(N_j - R\frac{\partial N_j}{\partial R})}{2R^2} detJ - \frac{\tau_{rz}N_j}{4\sqrt{R^3}}\frac{\partial N_i}{\partial z} detJ - \frac{\tau_{rz}}{2\sqrt{R}} detJ_{ij} \tag{193}$$

$$C_{2i-1,2j} = \sigma_{rr} detJ_{ij} + \frac{(\sigma_{\theta\theta} - \sigma_{rr})N_i}{2R}\frac{\partial N_j}{\partial z} detJ \tag{194}$$

$$C_{2i,2j-1} = -\sigma_{zz} detJ_{ij} + \frac{\tau_{rz}N_j}{\sqrt{R}}\frac{\partial N_i}{\partial R} detJ \tag{195}$$

$$C_{2i,2j} = 2\sqrt{R}\tau_{rz} detJ_{ij} \tag{196}$$

and

$$detJ_{ij} = \begin{matrix} \frac{\partial N_i}{\partial \alpha} & \frac{\partial N_j}{\partial \alpha} \\ \frac{\partial N_i}{\partial \beta} & \frac{\partial N_j}{\partial \beta} \end{matrix}, \tag{197}$$

The Jacobian determinant $detJ$ in equation (181) is defined by:

$$detJ = \begin{matrix} \frac{\partial R}{\partial \alpha} & \frac{\partial R}{\partial \beta} \\ \frac{\partial z}{\partial \alpha} & \frac{\partial z}{\partial \beta} \end{matrix} \tag{198}$$

For isoparametric formulations, the coordinate and velocity polynomial expansions are of the same order, namely:

$$R = \sum N_j R_j \tag{199}$$

$$z = \sum N_j z_j \tag{200}$$

where $(R_j, z_j)$ denotes generalised coordinates of node $j$.

By using the above equations, the Jacobian determinant may be determined by:

$$detJ = \begin{vmatrix} \sum \frac{\partial N_j}{\partial \alpha} R_j & \sum \frac{\partial N_j}{\partial \beta} R_j \\ \sum \frac{\partial N_j}{\partial \alpha} z_j & \sum \frac{\partial N_j}{\partial \beta} z_j \end{vmatrix} \tag{201}$$

Once the Jacobian determinant is computed, the derivatives defined in matrices **B** and **C** may be determined as follows:

$$\frac{\partial N_i}{\partial R} = \begin{vmatrix} \frac{\partial N_i}{\partial \alpha} & \frac{\partial z}{\partial \alpha} \\ \frac{\partial N_i}{\partial \beta} & \frac{\partial z}{\partial \beta} \end{vmatrix} / detJ \tag{202}$$

$$\frac{\partial N_i}{\partial z} = \begin{vmatrix} \frac{\partial R}{\partial \alpha} & \frac{\partial N_i}{\partial \alpha} \\ \frac{\partial R}{\partial \beta} & \frac{\partial N_i}{\partial \beta} \end{vmatrix} / detJ \tag{203}$$

### The Nodal Force Vectors

Expressions for each of the three nodal force vectors, are now given for axisymmetric elastic-plastic analyses performed with the new six-noded triangular element.

Residual Stresses

The element nodal force vector, as a result of residual stresses $\sigma_0$, is determined in the following manner beginning with equation ( 180):

$$\mathbf{P}^{\mathbf{e}}_{\mathbf{m}\sigma_{\mathbf{0}}} = \pi \int \int_{(\alpha,\beta)} B^T \sigma_0 det J d\alpha d\beta \tag{204}$$

Body Forces

The body forces per unit volume in the radial and axial directions are defined as $b_r$ and $b_z$ respectively. The corresponding nodal force vector is evaluated by applying the virtual work principle to an element in the original coordinates,

$$\mathbf{P}^{\mathbf{e}}_{\mathbf{mb}} = \pi \int \int_{(\alpha,\beta)} \mathbf{N}^{\mathbf{T}}_{\mathbf{m}} \mathbf{b} det J d\alpha d\beta \tag{205}$$

where

$$\mathbf{N_m} = \begin{bmatrix} \frac{N_1}{2r} & 0 & \dots & \frac{N_6}{2r} & 0 \\ 0 & N_1 & \dots & 0 & N_6 \end{bmatrix} \tag{206}$$

and

$$\mathbf{b} = [b_r, b_z]^T \tag{207}$$

Surface Tractions

The integral representing the nodal force vector as a result of the surface traction is not a volume integral, but rather a surface integral.

Figure 24 shows a distributed pressure defined by two components $q$ and $p$ acting on one of the edges of an element. For an infinitesimal section along the loaded boundary, $dl$, inclined at an angle $\theta$ to the positive $r$ direction, the applied surface pressures can be

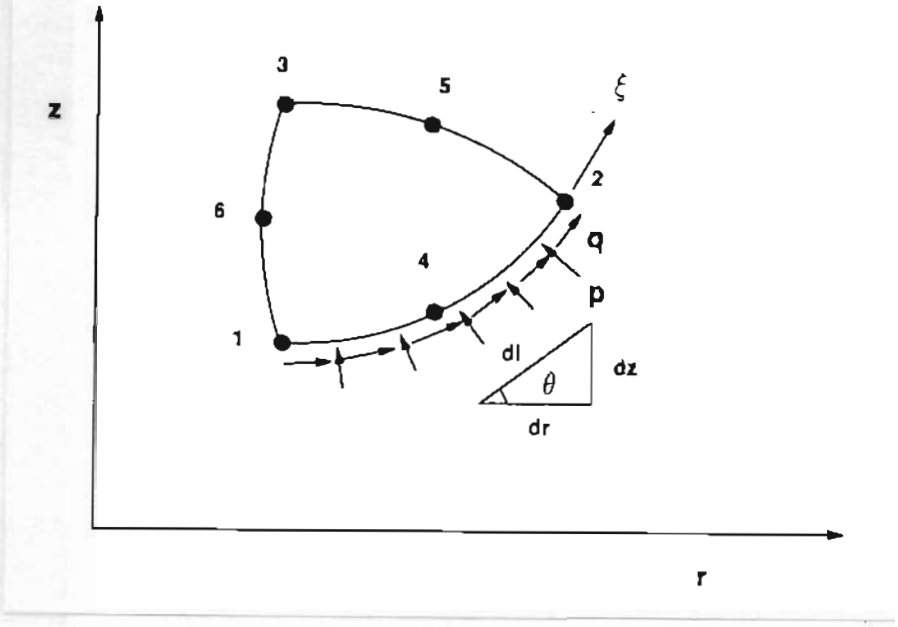


Figure 24: Calculation of distributed surface loadings

resolved into two surface traction $s_r$ and $s_z$ which are in the direction of the coordinate axes $r$ and $z$,

$$s_r dl = q dl \cos\theta - p dl \sin\theta \tag{208}$$

$$s_z dl = q dl \sin\theta + p dl \cos\theta \tag{209}$$

The above equations may also be written in terms of the generalized coordinates $R$ and $z$ by:

$$\begin{bmatrix} s_r \\ s_z \end{bmatrix} dl = \begin{bmatrix} \frac{q}{2r} dR - p dz \\ q dz + \frac{p}{2r} dR \end{bmatrix} \tag{210}$$

By using the virtual work principle, the equivalent nodal force vector can be shown to be:

$$\mathbf{P}^{e}_{ms} = \pi \int_{\xi} \mathbf{N}^{\mathbf{T}}_{mm} \begin{bmatrix} \frac{q}{2r}\frac{\partial R}{\partial \xi} - p\frac{\partial z}{\partial \xi} \\ q\frac{\partial z}{\partial \xi} + \frac{p}{2r}\frac{\partial R}{\partial \xi} \end{bmatrix} d\xi \tag{211}$$

where

$$\mathbf{N_{mm}} = \begin{bmatrix} N_1 & 0 & N_2 & 0 & N_4 & 0 \\ 0 & 2N_1 r & 0 & 2N_2 r & 0 & 2N_4 r \end{bmatrix} \tag{212}$$

in which $\alpha = \frac{1}{2}(\xi - 1)$.

## 5.6 Finite element formulation based on modified shape functions

An alternative procedure for implementing a finite element formulation based on the velocity expansions given in equations ( 162) and ( 163) is described in this section. In this approach, the conventional primary variables are retained but modifications are made to the shape functions.

**The Strain Rate - Velocity Relationship**

The velocity field vector $\mathbf{u}$ is defined in the conventional way:

$$\mathbf{u} = [\dot{r}, \dot{z}]^T = [\dot{u}, \dot{v}]^T \tag{213}$$

The strain rate vector is written in terms of the velocity vector:

$$\dot{\epsilon} = [\dot{\epsilon}_{rr}, \dot{\epsilon}_{zz}, \dot{\epsilon}_{\theta\theta}, \dot{\gamma}_{rz}, 2\dot{\omega}]^T = \mathbf{L_n u} \tag{214}$$

where the linear operator matrix $\mathbf{L_n}$ is

$$\mathbf{L_n} = \begin{bmatrix} \frac{\partial}{\partial r} & 0 \\ 0 & \frac{\partial}{\partial z} \\ \frac{1}{r} & 0 \\ \frac{\partial}{\partial z} & \frac{\partial}{\partial r} \\ \frac{\partial}{\partial z} & -\frac{\partial}{\partial r} \end{bmatrix} \tag{215}$$

**The Strain Rate - Nodal Velocity Matrices**

In this approach, the conventional nodal velocity vector $\mathbf{a^e}$ is used:

$$\mathbf{a^e} = [\dot{u}_1, \dot{v}_1, \ldots, \dot{u}_6, \dot{v}_6]^T \tag{216}$$

The proposed velocity expansion function defined by equations ( 162)-( 165) is used to relate the velocity field vector $\mathbf{u}$ to nodal velocity vector $\mathbf{a^e}$ as follows:

$$\mathbf{u} = \mathbf{N_n a^e} \tag{217}$$

where the new shape function matrix $\mathbf{N_n}$ is defined by

$$\mathbf{N_n} = \begin{bmatrix} \bar{N}_1 & 0 & \ldots & \bar{N}_6 & 0 \\ 0 & N_1 & \ldots & 0 & N_6 \end{bmatrix} \tag{218}$$

and

$$\bar{N}_i = \frac{N_i r_i}{r} \tag{219}$$

in which the functions $N_1, N_2, \ldots, N_6$ are given by equations ( 172)-( 177).

Substituting equation ( 217) into ( 214) results in:

$$\dot{\epsilon} = \mathbf{L_n u} = \mathbf{L_n N_n a^e} = \mathbf{B_n a^e} \tag{220}$$

where

$$\mathbf{B_n} = \mathbf{L_n N_n} = \begin{bmatrix} \frac{\partial \bar{N}_1}{\partial r} & 0 & \ldots & \frac{\partial \bar{N}_6}{\partial r} & 0 \\ 0 & \frac{\partial N_1}{\partial z} & \ldots & 0 & \frac{\partial N_6}{\partial z} \\ \frac{\bar{N}_1}{r} & 0 & \ldots & \frac{\bar{N}_6}{r} & 0 \\ \frac{\partial \bar{N}_1}{\partial z} & \frac{\partial N_1}{\partial r} & \ldots & \frac{\partial \bar{N}_6}{\partial z} & \frac{\partial N_6}{\partial r} \\ \frac{\partial \bar{N}_1}{\partial z} & -\frac{\partial N_1}{\partial r} & \ldots & \frac{\partial \bar{N}_6}{\partial z} & -\frac{\partial N_6}{\partial r} \end{bmatrix} \tag{221}$$

and

$$\frac{\partial \bar{N}_i}{\partial r} = -r_i \frac{N_i}{R} + 2r \frac{\partial N_i}{\partial R} \tag{222}$$

$$\frac{\bar{N}_i}{r} = r_i \frac{N_i}{R} \tag{223}$$

$$\frac{\partial \bar{N}_i}{\partial z} = \frac{r_i}{r} \frac{\partial N_i}{\partial z} \tag{224}$$

in which $\frac{\partial N_i}{\partial R}$ and $\frac{\partial N_i}{\partial z}$ are defined by equations ( 202)-( 203).

**The Nodal Force - Nodal velocity Relationship**

Following the same procedure used earlier, the virtual work principle can be used to give the following nodal force - nodal velocity relationship:

$$\dot{\mathbf{P}}^{\mathbf{e}} = \mathbf{K_n} \mathbf{a}^{\mathbf{e}} \tag{225}$$

where the nodal force vector is defined by:

$$\dot{\mathbf{P}}^{\mathbf{e}} = [(2\pi r p_h, 2\pi r p_v)_1 ... (2\pi r p_h, 2\pi r p_v)_6]^T \tag{226}$$

in which $p_h$ and $p_v$ represent nodal force increments per unit length in radial and axial directions respectively; The element stiffness matrix $\mathbf{K_n}$ is defined as :

$$\mathbf{K_n} = \pi \int \int_{V^e} \mathbf{B_n^T} ([D]^{ep} + [R]) \mathbf{B_n} det J \, d\alpha d\beta + \pi \int \int_{V^e} \mathbf{C}^n \, d\alpha d\beta \tag{227}$$

where matrix $\mathbf{C}^n$, which is defined by

$$\mathbf{C}^n \mathbf{a}^{\mathbf{e}} = (\mathbf{B_n^T} \dot{\mathbf{det J}}) \sigma \tag{228}$$

may be shown to be

$$\mathbf{C}^n = \begin{bmatrix} C^n_{1,1} & C^n_{1,2} & \dots & C^n_{1,12} \\ C^n_{2,1} & C^n_{2,2} & \dots & C^n_{2,12} \\ & & & \\ & & & \\ & & & \\ C^n_{12,1} & C^n_{12,2} & \dots & C^n_{12,12} \end{bmatrix} \tag{229}$$

in which

$$C^n_{2i-1,2j-1} = \frac{2N_iN_j\sqrt{R_iR_j}detJ}{R^2}(\sigma_{rr}-\sigma_{\theta\theta}) - 2\sqrt{\frac{R_iR_j}{R}}detJ_{ij}\tau_{rz} - \frac{\sqrt{R_iR_j}N_jdetJ}{R^{\frac{3}{2}}} \times\frac{\partial N_i}{\partial z}\tau_{rz} + \frac{2N_i\sqrt{R_iR_j}}{R}(\sigma_{\theta\theta}-\sigma_{rr})(\frac{\partial N_j}{\partial\alpha}\frac{\partial z}{\partial\beta} - \frac{\partial N_j}{\partial\beta}\frac{\partial z}{\partial\alpha}) \tag{230}$$

$$C^n_{2i-1,2j} = 2\sigma_{rr}\sqrt{R_i}detJ_{ij} + \frac{(\sigma_{\theta\theta}-\sigma_{rr})N_i\sqrt{R_i}}{R}(\frac{\partial N_j}{\partial\beta}\frac{\partial R}{\partial\alpha} - \frac{\partial N_j}{\partial\alpha}\frac{\partial R}{\partial\beta}) \tag{231}$$

$$C^n_{2i,2j-1} = \frac{2\tau_{rz}N_jdetJ}{\sqrt{R}}\frac{\partial N_i}{\partial R}\sqrt{R_j} - 2\sigma_{zz}\sqrt{R_j}detJ_{ij} \tag{232}$$

$$C^n_{2i,2j} = 2\sqrt{R}\tau_{rz}detJ_{ij} \tag{233}$$

and $detJ_{ij}$ and the Jacobian determinant $detJ$ are as defined by equations ( 197) and ( 198) in the previous section.

### The Nodal Force Vectors

In contrast to the formulation presented in the previous section, different velocity and nodal force vectors are used in this section. Hence, it is necessary to derive expressions for the nodal force vectors caused by some common loadings.

Residual Stresses

By using the equation ( 225), we may write the element nodal force vector as a result of residual stresses $\sigma_0$ as follows:

$$\mathbf{P}^{\mathbf{e}}_{\sigma_0} = \pi \int \int_{(\alpha,\beta)} \mathbf{B}^{\mathbf{T}}_{\mathbf{n}} \sigma_0 det J d\alpha d\beta \tag{234}$$

Body Force

The application of virtual work principle to an element may be used to give:

$$\mathbf{P}^{\mathbf{e}}_{\mathbf{b}} = \pi \int \int_{(\alpha,\beta)} \mathbf{N}^{\mathbf{T}}_{\mathbf{n}} \mathbf{b} det J d\alpha d\beta \tag{235}$$

where the body force vector $\mathbf{b}$ is defined by equation ( 207).

Surface Tractions

Applying the virtual displacement principle to the element shown in Figure 24, the equivalent nodal force vector may be shown to be:

$$\mathbf{P}^{\mathbf{e}}_{\mathbf{s}} = 2\pi \int_{\xi} \mathbf{N}^{\mathbf{T}}_{\mathbf{n}} r \begin{bmatrix} \frac{q}{2r}\frac{\partial R}{\partial \xi} - p\frac{\partial z}{\partial \xi} \\ q\frac{\partial z}{\partial \xi} + \frac{p}{2r}\frac{\partial R}{\partial \xi} \end{bmatrix} d\xi \tag{236}$$

where

$$\mathbf{N_n} = \begin{bmatrix} \bar{N}_1 & 0 & \bar{N}_2 & 0 & \bar{N}_4 & 0 \\ 0 & N_1 & 0 & N_2 & 0 & N_4 \end{bmatrix} \tag{237}$$

in which the relationship between $\alpha$ and $\xi$ is the same as defined earlier for the formulation based on modified primary variables.

## 5.7 Finite element discretization and effects of element shape

The two key ideas of the finite element method are: ($a$) discretization of the region being analysed into finite elements and ($b$) the use of interpolating polynomials to describe the variation of a field variable within an element (see, for example, Zienkiewicz, 1977). The

development of a rational displacement interpolation function has been discussed in the preceding section.

As far as discretization is concerned, there are two ways which may be used for finite element calculations using the new six-noded triangular element described in this thesis. First of all, the region being analysed defined in the original coordinates $(r, z)$ can be discretized into many six-noded triangular elements and then these triangles can be mapped into the generalized coordinates $(R, z)$ element by element. Alternatively, we can first map the whole region from the original coordinates into the generalized coordinates and then generate an element mesh in the configuration of the region being analysed in the generalized coordinates. Because of the mapping, the use of the first approach for discretization produces triangular elements with curved sides in the generalized coordinates, whilst the second approach may generate straight-sided triangles in the generalized coordinates, which correspond to curve-sided elements in the original coordinates. As the element stiffness matrix, as defined by equation ( 190) or ( 227), can be calculated using an element geometry defined in the generalized coordinates $(R, z)$, the second approach, which may be used to produce straight-sided elements in the generalized coordinates, is preferable. The second approach is also more convenient for practical use, especially when a suitable mesh generator is available.

In previous sections, the suitability of the new six-noded triangular element was assessed by assuming that all triangles had straight sides. Although this assumption is satisfactory for many problems, it is necessary to employ elements with irregular shapes in some cases (e.g. the first approach of discretization; the second approach of discretization for a large displacement analysis). In order to assess the effect of element shapes used for calculations, the suitability of the new six-noded triangular element with curved sides used in elastic-plastic analyses under axisymmetric conditions was investigated.

For a mesh of six-noded triangles for which the sides are not necessarily straight, the generalized area coordinates $(\alpha, \beta)$ are no longer coincident with the global coordinates $(R, z)$. Use of the proposed velocity expansion function (equation ( 162)-( 165)) may be made to give the velocity at any point within an element in the following form:

$$\dot{R} = c_1 - c_2\alpha - c_3\beta - c_4\alpha^2 - c_5\alpha\beta - c_6\beta^2 \tag{238}$$

$$\dot{z} = c_7 - c_8\alpha - c_9\beta - c_{10}\alpha^2 - c_{11}\alpha\beta - c_{12}\beta^2 \tag{239}$$

using the chain rule:

$$\frac{\partial \dot{R}}{\partial R} = \frac{\partial \dot{R}}{\partial \alpha}\frac{\partial \alpha}{\partial R} - \frac{\partial \dot{R}}{\partial \beta}\frac{\partial \beta}{\partial R} \tag{240}$$

and

$$\frac{\partial \dot{z}}{\partial z} = \frac{\partial \dot{z}}{\partial \alpha}\frac{\partial \alpha}{\partial z} - \frac{\partial \dot{z}}{\partial \beta}\frac{\partial \beta}{\partial z} \tag{241}$$

Differentiating equations ( 238) and ( 239), inserting in equations ( 240) and ( 241), and utilizing the axisymmetric incompressibility condition defined by equation ( 161) results in:

$$\begin{aligned}(c_2 + 2c_4\alpha - c_5\beta)\frac{\partial \alpha}{\partial R} - (c_3 + c_5\alpha - 2c_6\beta)\frac{\partial \beta}{\partial R} \quad + \\ (c_8 - 2c_{10}\alpha - c_{11}\beta)\frac{\partial \alpha}{\partial z} - (c_9 + c_{11}\alpha - 2c_{12}\beta)\frac{\partial \beta}{\partial z} \quad = \quad 0\end{aligned} \tag{242}$$

By using the definition of the Jacobian, we have:

$$\begin{bmatrix} \frac{\partial \alpha}{\partial R} & \frac{\partial \alpha}{\partial z} \\ \frac{\partial \beta}{\partial R} & \frac{\partial \beta}{\partial z} \end{bmatrix} = \frac{1}{detJ}\begin{bmatrix} \frac{\partial z}{\partial \beta} & -\frac{\partial R}{\partial \beta} \\ -\frac{\partial z}{\partial \alpha} & \frac{\partial R}{\partial \alpha} \end{bmatrix} \tag{243}$$

where Jacobian determinant $detJ$ is defined by equation ( 201).

Substituting the above equation into equation ( 242) furnishes:

$$\begin{aligned}(c_2 + 2c_4\alpha + c_5\beta)\frac{\partial z}{\partial \beta} - (c_3 + c_5\alpha - 2c_6\beta)\frac{\partial z}{\partial \alpha} \quad - \\ (c_8 + 2c_{10}\alpha + c_{11}\beta)\frac{\partial R}{\partial \beta} - (c_9 - c_{11}\alpha + 2c_{12}\beta)\frac{\partial R}{\partial \alpha} \quad = \quad 0\end{aligned} \tag{244}$$

For isoparametric formulations, the geometry expansion and velocity expansion are of the same order. The location of any point within a six-noded triangular element is thus defined by:

$$R = b_1 - b_2\alpha - b_3\beta - b_4\alpha^2 - b_5\alpha\beta - b_6\beta^2 \tag{245}$$

$$z = b_7 - b_8\alpha - b_9\beta - b_{10}\alpha^2 - b_{11}\alpha\beta - b_{12}\beta^2 \tag{246}$$

where $b_1, b_2, \ldots, b_{12}$ are functions of generalized nodal coordinates only.

Differentiating equations ( 245) and ( 246) and inserting equation ( 244) gives the following incompressibility condition:

$$\bar{c}_1 - \bar{c}_2\alpha - \bar{c}_3\beta - \bar{c}_4\alpha^2 - \bar{c}_5\alpha\beta - \bar{c}_6\beta^2 = 0 \tag{247}$$

where

$$\bar{c}_1 = c_2b_9 - c_3b_8 - c_8b_3 + c_9b_2 \tag{248}$$

$$\bar{c}_2 = c_2b_{11} - 2c_4b_9 - 2c_3b_{10} - c_5b_{11} - c_8b_5 - 2c_{10}b_3 + 2c_{10}b_4 - c_{11}b_2 \tag{249}$$

$$\bar{c}_3 = c_5b_9 + 2c_2b_{12} - c_3b_{11} - 2c_6b_8 - 2c_8b_{10} - c_{11}b_3 + c_9b_5 + 2c_{12}b_2 \tag{250}$$

$$\bar{c}_4 = 2c_4b_{11} - 2c_5b_{10} - 2c_{10}b_5 + 2c_{11}b_4 \tag{251}$$

$$\bar{c}_5 = 4c_4b_{11} - 4c_6b_{10} - 4c_{10}b_6 - 4c_{12}b_4 \tag{252}$$

$$\bar{c}_6 = 2c_5b_{12} - 2c_6b_{11} - 2c_{11}b_6 - 2c_{12}b_5 \tag{253}$$

Before we can assess the number of constraints imposed by the incompressibility condition equation ( 247) on nodal velocities, the appropriate order of Quadrature for the new six-noded triangular element used for axisymmetric problems needs to be discussed. The best order of Quadrature is usually decided after numerical testing, since the profits and pitfalls of a particular rule are hard to forsee. Often it is best to use as low an order as possible without precipitating a numerical disaster because a rule using fewer points results in lower computational cost.

There is a lower limit on the number of sampling points because the Quadrature rule must be competent enough to integrate the element volume exactly. The argument begins with the observation that as a mesh is refined and a constant strain condition comes to prevail in each element, which implies a constant strain energy density for

elastic materials, the strain energy for an elastic structure is correctly assessed if the volume of the structure is correctly computed. For the new six-noded triangular element of finite size used for axisymmetric problems, we need to find a rule which can correctly integrate the element volume, as defined by:

$$V^e = 2\pi \int\int_{(r,z)} r dr dz = \pi \int\int_{(R,z)} dR dz = \pi \int\int_{(\alpha,\beta)} det J d\alpha\beta \tag{254}$$

From equations ( 201) and ( 172)-( 177) we may note that the Jacobian determinant $detJ$ contains $\alpha^2$ and $\beta^2$, so a three-point rule is needed. It can easily be proved that for the conventional six-noded triangular element used for plane strain problems a three-point integration rule is needed to assess the element volume correctly.

For the conventional six-noded triangular elements used for axisymmetric configurations, the element volume may be defined in the form:

$$\bar{V}^e = 2\pi \int\int_{(r,z)} r dr dz = 2\pi \int\int_{(\bar{\alpha},\bar{\beta})} r det\bar{J} d\bar{\alpha} d\bar{\beta} \tag{255}$$

note here $\bar{\alpha}, \bar{\beta}$ denote the conventional area coordinates of the element defined in the coordinates $(r, z)$. For an isoparametric element, $r det\bar{J}$ may be proved to contain $\bar{\alpha}^4$ and $\bar{\beta}^4$, so a six-point rule is needed to assess the element volume correctly. This order of the Quadrature rule corresponds to the so-called 'Full-Integration'.

If a three-point rule is used, the incompressibility condition, represented by equation ( 247), needs to be satisfied at three independent locations within the element. Adopting matrix notation, the constant volume requirement may be written in the matrix form:

$$\begin{bmatrix} 1 & \alpha_1 & \beta_1 & \alpha_1^2 & \alpha_1\beta_1 & \beta_1^2 \\ 1 & \alpha_2 & \beta_2 & \alpha_2^2 & \alpha_2\beta_2 & \beta_2^2 \\ 1 & \alpha_3 & \beta_3 & \alpha_3^2 & \alpha_3\beta_3 & \beta_3^3 \end{bmatrix} \begin{pmatrix} \bar{c}_1 \\ \bar{c}_2 \\ \bar{c}_3 \\ \bar{c}_4 \\ \bar{c}_5 \\ \bar{c}_6 \end{pmatrix} = 0 \tag{256}$$

In general, the above matrix is of rank three (Sloan, 1981) and hence there are a maximum of three independent constraints on the $\bar{c}_i$. For the new six-noded triangles with curved

sides used in axisymmetric conditions, the three-point integration rule implies that for the limiting case of a very fine mesh the number of degrees of freedom per constraint is equal to $\frac{4}{3}$. It is interesting to note that if a higher order Quadrature scheme is used, for example a six-point rule, then the left hand side of equation ( 256) will have rank six, which will increase the number of constraints per element from three to six.

In summary, it is suggested that the new six-noded triangle is not only suitable for use in axisymmetric grids where all the element sides are straight, but is also satisfactory for use in axisymmetric configurations where all triangles sides are curved provided a three-point rule is used. It has been shown that a three-point rule used in the new six-noded triangles under axisymmetric loading is able to assess the elastic strain energy correctly.

In order to make the finite element formulation developed in the previous sections complete, the next section is devoted to a description of the constitutive models and their implementations. With respect to the constitutive models, a special effort is made by the Author to develop a new method of implementing the Matsuoka model so that the dilation of the soil can be properly accounted for. This development is described in Section 5.8.2. By comparison, the theory of the von Mises plasticity is relatively well understood. The formulation of the von Mises plasticity model described by Burd (1986) and Teh (1987) has been retained and repeated in the next section purely for the sake of entirety.

## 5.8 Constitutive laws

An ideal elastic-perfectly plastic model has been adopted for both clay and sand, since most of the analyses of pressuremeter tests are developed by assuming perfectly plastic behaviour of soils. The most common constitutive laws used in finite element models to represent cohesive and frictional soils are the Tresca and Mohr-Coulomb models. These constitutive laws, however, contain discontinuous yield surfaces with edges at which the yield function is not differentiable. Although these singularities are not often approached for plane strain conditions, they are important for a number of problems involving axisymmetric loading (Sloan, 1981). In order to implement the material model correctly, two

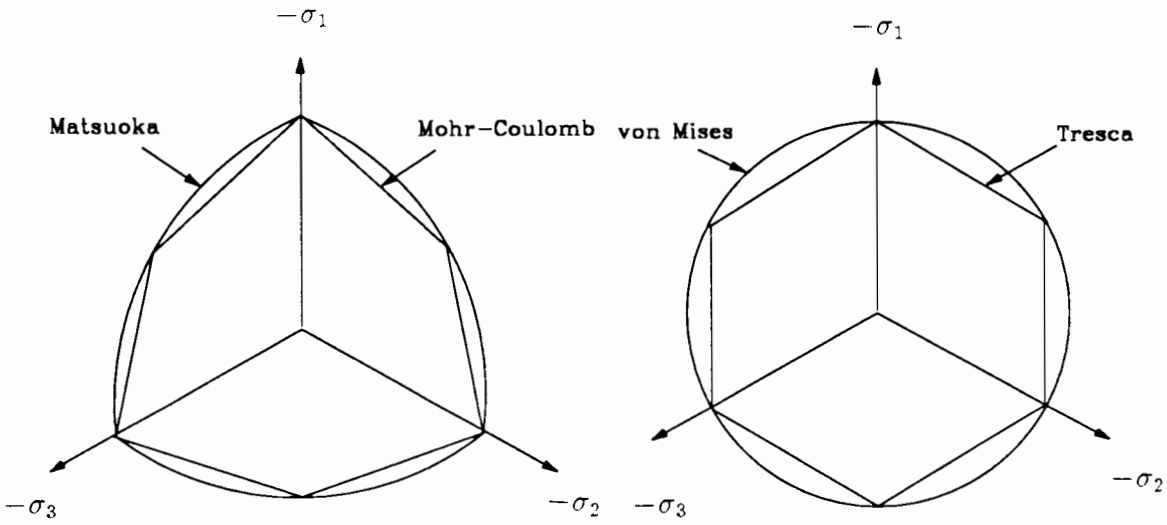


Figure 25: Relationship between different yield surfaces (after Burd, 1986)

possible methods may be used. The first option is to apply the method of dealing with corners of yield surfaces described in Chapter 3 to two dimensional cases. Alternatively, we can adopt the von Mises and Matsuoka plasticity models to model clay and sand respectively in the two dimensional analysis. Both von Mises and Matsuoka models have the advantage over the Tresca and Mohr-Coulomb models that they are everywhere differentiable (except at the origin for the case of the Matsuoka yield function) and are more realistic for modelling soil behaviour (Wroth and Houlsby, 1985). For these reasons, the latter approach has been adopted. The relationship between these two sets of yield surfaces is illustrated in Figure 25, which shows sections through the yield loci in the '$\pi$' plane for the special case when they coincide at the 'corners' of the Tresca and Mohr-Coulomb surfaces.

In order to compare the results of plane strain analyses based on these two sets of constitutive laws, it is necessary to find relationships between the material properties used in the corresponding models. The plane strain undrained shear strength $s_{ups}$, plane strain friction angle, $\phi_{ps}$ and plane strain dilation angle $\psi_{ps}$ will be used to obtain these relationships, and are defined:

$$s_{ups} = \frac{\sigma_1 - \sigma_3}{2} \tag{257}$$

$$\sin \phi_{ps} = \frac{\sigma_1 - \sigma_3}{\sigma_1 - \sigma_3} \tag{258}$$

$$\sin \psi_{ps} = \frac{\dot{\epsilon}_1 - \dot{\epsilon}_3}{\dot{\epsilon}_1 - \dot{\epsilon}_3} \tag{259}$$

where $\sigma_1$ and $\sigma_3$ are the major and minor in-plane principal stresses respectively. In this section, values of $s_{ups}$ and $\phi_{ps}$ defined above are related to the equivalent values of triaxial compression shear strength $s_{utc}$, friction angle, $\varphi_{tc}$ and dilation angle $\psi_{tc}$, that are used in the von Mises and Matsuoka models. These relationships will be derived for the case of plane strain in following sections.

### 5.8.1 von Mises plasticity

The von Mises yield function is defined as:

$$f(\sigma) = (\sigma_{rr} - \sigma_{zz})^2 - (\sigma_{zz} - \sigma_{\theta\theta})^2 - (\sigma_{\theta\theta} - \sigma_{rr})^2 + 6\tau_{rz}^2 - 8s_{utc}^2 \tag{260}$$

An alternative form of the equation is:

$$f(\sigma) = (\sigma_1 - \sigma_3)^2 + (\sigma_1 - \sigma_2)^2 - (\sigma_2 - \sigma_3)^2 - 8s_{utc}^2 \tag{261}$$

The plastic strain rates are derived from an associated flow rule which gives zero plastic volumetric strain and is therefore suitable for the modelling of undrained clay behaviour. Using equation ( 110), the plastic material stiffness matrix may be derived as:

$$[D]^p = -\frac{3G}{4s_{utc}^2} \begin{bmatrix} S_{rr}^2 & S_{rr}S_{zz} & S_{rr}S_{\theta\theta} & S_{rr}\tau_{rz} & 0 \\ S_{zz}S_{rr} & S_{zz}^2 & S_{zz}S_{\theta\theta} & S_{zz}\tau_{rz} & 0 \\ S_{\theta\theta}S_{rr} & S_{\theta\theta}S_{zz} & S_{\theta\theta}^2 & S_{\theta\theta}\tau_{rz} & 0 \\ S_{rr}\tau_{rz} & \tau_{rz}S_{zz} & \tau_{rz}S_{\theta\theta} & \tau_{rz}^2 & 0 \\ 0 & 0 & 0 & 0 & 0 \end{bmatrix} \tag{262}$$

where $S_{rr}$, $S_{\theta\theta}$ and $S_{zz}$ are the deviatoric stresses, which are defined by equations (284)-(285).

The associated flow rule may be used to show that, in the limit that the elastic strain rates are negligible in comparison with the plastic strain rates. The intermediate stress may be expressed by:

$$\sigma_2 = \frac{\sigma_1 - \sigma_3}{2} \tag{263}$$

By substituting this equation into the von Mises yield surface and using equation ( 257), the following relationship may be obtained,

$$s_{ups} = \frac{2}{\sqrt{3}} s_{utc} \tag{264}$$

### 5.8.2 Matsuoka plasticity

The Matsuoka yield function (Matsuoka, 1976) may be written as a function of the principal stresses:

$$f(\sigma) = \frac{(\sigma_1 - \sigma_2)^2}{\sigma_1\sigma_2} + \frac{(\sigma_2 - \sigma_3)^2}{\sigma_2\sigma_3} + \frac{(\sigma_3 - \sigma_1)^2}{\sigma_3\sigma_1} - 8\tan^2\phi_{tc} \tag{265}$$

where $\phi_{tc}$ is the triaxial compression friction angle. An alternative expression for the yield surface may be written in terms of stress invariants:

$$f(\sigma) = I_1 I_2 - I_3\varsigma \tag{266}$$

where $\varsigma = 9 - 8\tan^2\phi_{tc}$ and

$$I_1 = \sigma_1 - \sigma_2 + \sigma_3 \tag{267}$$

$$I_2 = \sigma_1\sigma_2 + \sigma_2\sigma_3 - \sigma_3\sigma_1 \tag{268}$$

$$I_3 = \sigma_1\sigma_2\sigma_3 \tag{269}$$

Two methods may be used to derive an approach by which a plasticity formulation may be developed, based on the Matsuoka yield function, in such a way that the dilation

and friction angles may be specified independently of each other. In the first approach as described by Burd (1986), a procedure is used to interpolate between plastic strain rates corresponding to two limits of behaviour. These two limits are known to be the case of the fully associated flow rule and the case in which the flow rule is associated in '$\pi$' plane but with zero plastic volumetric strain rate.

Following the classic way of dealing with the Mohr-Coulomb plasticity, in this study, an alternative approach is developed in which the plastic strain rates are derived from the flow rule:

$$\dot{\epsilon}^{p}_{ij} = \lambda \frac{\partial g}{\partial \sigma_{ij}} \tag{270}$$

where $g$ is the plastic potential as defined by:

$$g(\sigma_{ij}) = I_1^{\star} I_2^{\star} - I_3^{\star} \varsigma^{\star} \tag{271}$$

and

$$\varsigma^{\star} = 9 - 8 \tan^2 \psi_{tc} \tag{272}$$

$$I_1^{\star} = \sigma_1^{\star} + \sigma_2^{\star} + \sigma_3^{\star} \tag{273}$$

$$I_2^{\star} = \sigma_1^{\star}\sigma_2^{\star} + \sigma_2^{\star}\sigma_3^{\star} + \sigma_3^{\star}\sigma_1^{\star} \tag{274}$$

$$I_3^{\star} = \sigma_1^{\star}\sigma_2^{\star}\sigma_3^{\star} \tag{275}$$

$$\sigma_{ij}^{\star} = \sigma_{ij} + k\delta_{ij} \tag{276}$$

This plastic potential function is of a similar form to the Matsuoka yield function, but the triaxial friction angle is replaced by the triaxial dilation angle $\psi_{tc}$, and the apex of the surface is moved from the origin to the point in principal stress space with the coordinates $(-k, -k, -k)$. The parameter $k$ is calculated on the basis that the plastic potential and the yield function must coincide at the current stress state. This condition is used to derive a cubic equation in $k$ from which the required root may easily be selected.

**Relationships between triaxial and plane strain parameters**

It is of interest to consider the relationships between $\phi_{tc}$ and $\psi_{tc}$ and the parameters defined in equations ( 258) and ( 259) for the case where the proposed plasticity model is used under conditions of plane strain. Firstly, it is instructive to consider the two limiting cases, i.e. the full association and the zero dilation, for which it is possible to derive closed form expressions for these relationships.

In order to find the relationship between triaxial compression and plane strain friction angle for the case of full association (where the yield function and plastic potential are identical), it is necessary to consider the limiting case for which the elastic strain rates are negligible in comparison with the plastic strain rates. This implies that the intermediate plastic strain is zero. An expression for the intermediate plastic strain rate may be derived from equation ( 270) which, if set to zero, gives the relationship:

$$\sigma_2 = \sqrt{\sigma_1 \sigma_3} \tag{277}$$

where $\sigma_2$ is the out of plane principal stress. If equation ( 258) and equation ( 277) are substituted into the Matsuoka yield function then the following relationship is obtained:

$$2 \sec^2 \phi_{tc} = \sec \phi_{ps} + \sec^2 \phi_{ps} \tag{278}$$

The case of zero plastic volumetric strain rate is obtained in the limit when $k$ tends to infinity. In this limit case in the limit that the elastic rates are negligible in comparison with the plastic strain rates and $\sigma_2$ may be shown to be:

$$\sigma_2 = \frac{1}{2}(\sigma_1 + \sigma_3) \tag{279}$$

The triaxial and plane strain friction angles in this case may be shown to be related by the expression:

$$\tan^2 \phi_{tc} = \frac{3}{4} \tan^2 \phi_{ps} \tag{280}$$

A general relationship between the Mohr-Coulomb and the Matsuoka constants when the dilation angle lies between zero and the friction angle may again be obtained by

considering the limiting case for the Matsuoka model in which the intermediate plastic strain rate is zero. The intermediate plastic strain rate may be derived from equation ( 270), which, if equated to zero, gives the following equation:

$$(\sigma_2^* - \frac{\sigma_1^* \sigma_3^*}{\sigma_2^*})(\sigma_1^* - \sigma_3^*) = 0 \tag{281}$$

Table 5.1 Relationships between the triaxial and plane strain parameters

| $\varphi_{ps}$ | $\psi_{tc}$ | $\varphi_{tc}$ | $\psi_{ps}$ |
|---|---|---|---|
| $30^0$ | $0.05^0$ | $26.56^0$ | $0.06^0$ |
| | $4.78^0$ | $26.48^0$ | $5.52^0$ |
| | $10.01^0$ | $26.42^0$ | $11.54^0$ |
| | $15.84^0$ | $26.34^0$ | $18.21^0$ |
| | $19.72^0$ | $26.31^0$ | $22.62^0$ |
| | $26.29^0$ | $26.29^0$ | $30.00^0$ |
| $40^0$ | $0.06^0$ | $36.00^0$ | $0.07^0$ |
| | $6.15^0$ | $35.83^0$ | $7.10^0$ |
| | $12.94^0$ | $35.67^0$ | $14.90^0$ |
| | $20.66^0$ | $35.52^0$ | $23.69^0$ |
| | $25.96^0$ | $35.45^0$ | $29.63^0$ |
| | $35.39^0$ | $35.39^0$ | $40.00^0$ |
| $50^0$ | $0.03^0$ | $45.90^0$ | $0.04^0$ |
| | $6.36^0$ | $45.68^0$ | $7.33^0$ |
| | $12.85^0$ | $45.46^0$ | $14.79^0$ |
| | $19.63^0$ | $45.25^0$ | $22.52^0$ |
| | $33.36^0$ | $44.93^0$ | $37.79^0$ |
| | $44.82^0$ | $44.82^0$ | $50.00^0$ |

Since in this general case it is not possible to obtain an expression that can be used to eliminate $\sigma_2$ from the Matsuoka yield function, a numerical method must be used to calculate combinations of the parameters $\varphi_{tc}, \psi_{tc}$ used in the Matsuoka model and $\varphi_{ps}, \psi_{ps}$

defined in equations ( 258) and ( 259). Some selected comparisons between the triaxial and the plane parameters calculated in this way are listed in Table 5.1.

## 5.9 Calculation of strain rates from nodal velocities

The basic non-linear finite element equations normally need to be solved by an incremental approach using sufficiently small load increments. After each step, the Gauss point stresses are evaluated by using incremental stress-strain relationship, and this requires the determination of the strain rate at each Gauss point. In this thesis, the approach making use of the averaged geometry of finite element meshes during the load increment is used to derive strain rates for given nodal displacements. This method has been successfully used by Carter et al (1977) and Teh (1987).

To provide a complete understanding of the numerical implementation of the plasticity models, a description of the procedure of stress update calculation is given in the next section and this is mainly based on the formulation described in Chapters 4 and 5 of the thesis by Burd (1986) for plane strain problems. Fundamentally, there is no difference in the procedure of the stress update calculations used in the plane strain and axisymmetric cases. This means that the stress update routines used for the plane strain finite element analysis may be used for the stress update calculation in axisymmetric analysis.

## 5.10 Stress update calculation

### 5.10.1 Integration of stress-strain laws

In the calculation of the updated Gauss point stresses, several cases of constitutive behaviour need to be considered and these are dealt with in turn. In addition, it is necessary to evaluate yield surface intersections for the case when the material changes state during the calculation step.

In this study, all stress increments are initially assumed elastic, regardless of the initial state. If the resulting final stress point lies outside the yield surface, the stress update

calculation is repeated using the appropriate elastic-plastic constitutive relationship, thus the possibility of elastic unloading is taken into account (Davis et al., 1974).

The mean pressure $p$, and volumetric strain rate $\dot{v}$ are defined as:

$$p = \frac{1}{3}(\sigma_{rr} - \sigma_{zz} - \sigma_{\theta\theta}) \tag{282}$$

$$\dot{v} = \dot{\epsilon_{rr}} - \dot{\epsilon_{zz}} - \dot{\epsilon_{\theta\theta}} \tag{283}$$

where the superior dot denotes a derivative with respect to a fixed Cartesian reference frame. Deviatoric stresses $S_{rr}, S_{zz}$ and deviatoric strain rates $\dot{\epsilon_{rr}}, \dot{\epsilon_{zz}}$ are defined by:

$$S_{rr} = \sigma_{rr} - p \tag{284}$$

$$S_{zz} = \sigma_{zz} - p \tag{285}$$

$$\dot{\epsilon_{rr}} = \dot{\epsilon_{rr}} - \frac{\dot{v}}{3} \tag{286}$$

$$\dot{\epsilon_{zz}} = \dot{\epsilon_{zz}} - \frac{\dot{v}}{3} \tag{287}$$

In all of the solutions described in this section, the material deformation is defined by the strain rates derived by the approach described in the last section, in which the calculation increment is taken to occur during the time interval $[0, 1]$.

### Elastic behaviour with Jaumann rotation terms

The mean pressure at time $t$ is given by:

$$p = p_0 - K\dot{v}t \tag{288}$$

where $p_0$ is the mean pressure at time $t = 0$ and $K$ is the bulk modulus. The constitutive equation relates strain rates to Jaumann stress rates which, for elastic behaviour gives the following relationship between the deviatoric components:

$$\hat{S_{rr}} = 2G\dot{e_{rr}} \tag{289}$$

$$\hat{S_{zz}} = 2G\dot{\epsilon_{zz}} \tag{290}$$

$$\hat{\tau_{rz}} = G\dot{\gamma_{rz}} \tag{291}$$

where $G$ is the shear modulus.

The deviatoric forms of the Jaumann stress rates given in equation ( 149) are:

$$\hat{S_{rr}} = \dot{S_{rr}} - 2\tau_{rz}\dot{\omega_{rz}} \tag{292}$$

$$\hat{S_{zz}} = \dot{S_{zz}} - 2\tau_{rz}\dot{\omega_{rz}} \tag{293}$$

$$\hat{\tau_{rz}} = \dot{\tau_{rz}} + \dot{\omega_{rz}}(S_{rr} - S_{zz}) \tag{294}$$

Equations ( 292)-( 294) may be solved using the constitutive equations ( 289)-( 291) to give a solution for the stresses (Houlsby, 1987):

$$\begin{aligned} S_{rr} = {} & \frac{S_{rr0} - S_{zz0}}{2} - \frac{S_{rr0} - S_{zz0}}{2}\cos 2\dot{\omega}t - G[\dot{\epsilon_{rr}} - \dot{\epsilon_{zz}} + (\dot{\epsilon_{rr}} - \dot{\epsilon_{zz}})\frac{\sin 2\dot{\omega}t}{2\dot{\omega}} \\ & -\dot{\gamma_{rz}}(\frac{1 - \cos 2\dot{\omega}t}{2\dot{\omega}})] - \tau_{rz0}\sin 2\dot{\omega}t \end{aligned} \tag{295}$$

$$\begin{aligned} S_{zz} = {} & \frac{S_{rr0} - S_{zz0}}{2} - \frac{S_{rr0} - S_{zz0}}{2}\cos 2\dot{\omega}t + G[\dot{\epsilon_{rr}} + \dot{\epsilon_{zz}} + (\dot{\epsilon_{rr}} - \dot{\epsilon_{zz}})\frac{\sin 2\dot{\omega}t}{2\dot{\omega}} \\ & -\dot{\gamma_{rz}}(\frac{1 - \cos 2\dot{\omega}t}{2\dot{\omega}})] - \tau_{rz0}\sin 2\dot{\omega}t \end{aligned} \tag{296}$$

$$\begin{aligned} \tau_{rz} = {} & \tau_{rz0}\cos 2\dot{\omega}t + G\dot{\gamma_{rz}}\frac{\sin 2\dot{\omega}t}{2\dot{\omega}} - \frac{1}{2}(S_{rr0} - S_{zz0})\sin 2\dot{\omega}t \\ & -G(\dot{\epsilon_{rr}} - \dot{\epsilon_{zz}})(\frac{1 - \cos 2\dot{\omega}t}{2\dot{\omega}}) \end{aligned} \tag{297}$$

where $S_{rr0}, S_{zz0}, \tau_{rz0}$ are the values at the start of the calculation step and $\dot{\omega}$ is used to denote $\dot{\omega_{rz}}$ for simplicity. When the rotation rate is very small, the use of equations

( 295)-( 297) leads to significant 'round off' errors since the evaluation of these expressions involves dividing by the rotation rate. In this case, expanded equations in which the rotation terms appear only in the numerator should be used to avoid this difficulty. If an expansion is used in which only the first order rotation terms are retained, then the above equations reduce to:

$$S_{rr} = S_{rr0} - G[\dot{\epsilon}_{rr} - \dot{\epsilon}_{zz} - (\dot{\epsilon}_{rr} - \dot{\epsilon}_{zz})t - \dot{\gamma}_{rz}\dot{\omega}t^2] - 2\tau_{rz0}\dot{\omega}t \tag{298}$$

$$S_{zz} = S_{zz0} - G[\dot{\epsilon}_{rr} - \dot{\epsilon}_{zz} - (\dot{\epsilon}_{rr} - \dot{\epsilon}_{zz})t - \dot{\gamma}_{rz}\dot{\omega}t^2] - 2\tau_{rz0}\dot{\omega}t \tag{299}$$

$$\tau_{rz} = \tau_{rz0} - G\dot{\gamma}_{rz}t - (S_{rr0} - S_{zz0})\dot{\omega}t - G(\dot{\epsilon}_{rr} - \dot{\epsilon}_{zz})\dot{\omega}t^2 \tag{300}$$

**von Mises plasticity, Jaumann terms excluded**

A closed form solution exists for the case of von Mises plasticity when the Jaumann terms are not included (Krieg and Krieg, 1977).

The volumetric behaviour is always elastic and the mean pressure may be derived from equation ( 288) . The solution for the deviatoric stresses is:

$$S_{rr} = \frac{S_{rr0}}{\eta} + \frac{\zeta}{\eta}2G\dot{\epsilon}_{rr} \tag{301}$$

$$S_{zz} = \frac{S_{zz0}}{\eta} + \frac{\zeta}{\eta}2G\dot{\epsilon}_{zz} \tag{302}$$

$$\tau_{rz} = \frac{\tau_{rz0}}{\eta} + \frac{\zeta}{\eta}G\dot{\gamma}_{rz} \tag{303}$$

where

$$\zeta = (\frac{\alpha}{\beta})sinh(\frac{\beta}{\alpha}t) + (\frac{\alpha}{\beta})\chi cosh(\frac{\beta}{\alpha}t) - (\frac{\alpha}{\beta})\chi \tag{304}$$

$$\eta = cosh(\frac{\beta}{\alpha}t) + \chi sinh(\frac{\beta}{\alpha}t) \tag{305}$$

$$\alpha = \frac{2}{\sqrt{3}} s_{utc} \tag{306}$$

$$\beta^2 = 4G^2\left[\dot{\epsilon_{rr}}^2 + \dot{\epsilon_{rr}}\dot{\epsilon_{zz}} - \dot{\epsilon_{zz}}^2 - \frac{\dot{\gamma}_{rz}^2}{4}\right] \tag{307}$$

$$2\alpha\beta\chi = 2G\left[S_{rr0}(2\dot{\epsilon_{rr}} - \dot{\epsilon_{zz}}) - S_{zz0}(2\dot{\epsilon_{zz}} - \dot{\epsilon_{rr}}) - \tau_{rz0}\dot{\gamma}_{rz}\right] \tag{308}$$

and $S_{rr0}, S_{zz0}, \tau_{rz0}$ are the values of the stresses at the start of the calculation increment.

#### von Mises plasticity, including Jaumann rotation terms

It is necessary to use a numerical method to integrate the constitutive laws for the case of von Mises plasticity when rotation effects are present. The algorithm used in this thesis is based on a Runge-Kutta integration scheme in which the updated stresses are evaluated by dividing the calculation step into a number of sub-increments. In order to improve the efficiency of this calculation, a procedure is used in which the size of the sub-increment is varied automatically in order to perform the integration at each of the Gauss points to a specified accuracy. In this algorithm, which is described by Sloan (1987), an estimate is made of the errors occurring at each sub-increment. The magnitude of the error is then used to determine the size of the following sub-increment, or if the error is unacceptable, the size of the sub-increment is reduced, and the calculation repeated.

#### Matsuoka plasticity

Since no closed form solution exists for the stress update calculation in which the constitutive law is based on the Matsuoka yield function, the error-control algorithm described above is used to perform stress update for Matsuoka plasticity for both cases of small strain and large strain.

### 5.10.2 Determination of yield surface intersection

For the case when material becomes plastic during the calculation step, it is necessary to determine the point in the increment at which yield surface intersection occurs. This

can be found by substituting the elastic stresses solution into the yield equation.

### von Mises plasticity

The elastic equations may be substituted into the von Mises yield function to give an equation that defines the time, $t$, at which intersection with the von Mises yield surface occurs:

$$A_1 t^2 + A_2 t - A_3 \frac{1 - \cos 2\dot{\omega} t}{\dot{\omega}^2} + A_4 \frac{\sin 2\dot{\omega} t}{\dot{\omega}} + A_5 = 0 \tag{309}$$

where

$$A_1 = 12G^2(\dot{\epsilon_{rr}} + \dot{\epsilon_{zz}})^2 \tag{310}$$

$$A_2 = 12G(S_{rr0} - S_{zz0})(\dot{\epsilon_{rr}} - \dot{\epsilon_{zz}}) \tag{311}$$

$$A_3 = 2\dot{\omega}G[2\tau_{rz0}(\dot{\epsilon_{rr}} - \dot{\epsilon_{zz}}) - \dot{\gamma_{rz}}(S_{rr0} - S_{zz0})] - 2G^2[\dot{\gamma_{rz}} + (\dot{\epsilon_{rr}} - \dot{\epsilon_{zz}})^2] \tag{312}$$

$$A_4 = 2G[2\tau_{rz0}\dot{\gamma_{rz}} + (S_{rr0} - S_{zz0})(\dot{\epsilon_{rr}} - \dot{\epsilon_{zz}})] \tag{313}$$

$$A_5 = 4[S_{rr0}^2 + S_{rr0}S_{zz0} + S_{zz0}^2 + \tau_{rz0}^2 - \frac{4}{3}s_{utc}^2] \tag{314}$$

For the case of the small rotation, equation ( 309) reduces to:

$$(A_1 + 2A_3)t^2 + (A_2 + 2A_4)t - A_5 = 0 \tag{315}$$

The above equation may be used to calculate the time $t$ at which the yield surface intersection occurs for the case where the rotation rate is very small. The general solution for equation ( 309) may be obtained using a Newton-Raphson iterative scheme. The small rotation solution may be used as an initial estimate when using a numerical iteration scheme.

### Matsuoka plasticity

The Matsuoka yield function may be rearranged into the following form:

$$\varsigma I_3' + pI_2'(\varsigma - 3) - p^3(\varsigma - 9) = 0 \tag{316}$$

where $\varsigma$ is defined in equation ( 266), $p$ is the mean pressure and $I_2', I_3'$ are deviatoric stress invariants.

From the elastic equations derived for the case when rotation effects are absent, we have:

$$I_3' = a_0 - a_1(2Gt) - a_2(2Gt)^2 - a_3(2Gt)^3 \tag{317}$$

$$pI_2' = b_0 - b_1(2Gt) - b_2(2Gt)^2 - b_3(2Gt)^3 \tag{318}$$

$$p^3 = c_0 + c_1(2Gt) + c_2(2Gt)^2 + c_3(2Gt)^3 \tag{319}$$

where

$$a_0 = \frac{S_{a0}}{4}\left[4\tau_{rz0}^2 + S_{b0}^2 - S_{a0}^2\right] \tag{320}$$

$$a_1 = \dot{\epsilon}_a\tau_{rz0}^2 + \dot{\gamma}_{rz}\tau_{rz0}S_{a0} - \frac{S_{a0}}{2}\left[\dot{\epsilon}_a S_{a0} - \dot{\epsilon}_b S_{b0}\right] - \frac{\dot{\epsilon}_a}{4}\left[S_{a0}^2 - S_{b0}^2\right] \tag{321}$$

$$a_2 = S_{a0}\frac{\dot{\gamma}_{rz}}{4} + \dot{\gamma}_{rz}\tau_{rz0}\dot{\epsilon}_a - \frac{\dot{\epsilon}_a}{2}\left[\dot{\epsilon}_a S_{a0} - \dot{\epsilon}_b S_{b0}\right] - \frac{S_{a0}}{4}\left[\dot{\epsilon}_a{}^2 - \dot{\epsilon}_b{}^2\right] \tag{322}$$

$$a_3 = -\frac{\dot{\epsilon}_a}{4}\left[\dot{\epsilon}_a{}^2 - \dot{\epsilon}_b{}^2 - \dot{\gamma}_{rz}{}^2\right] \tag{323}$$

$$b_0 = -p_0\left[\frac{3S_{a0}^2 + S_{b0}^2 - 4\tau_{rz0}^2}{4}\right] \tag{324}$$

$$b_1 = -\frac{K\dot{v}}{2G}\left[\frac{3S_{a0}^2 - S_{b0}^2 + 4\tau_{rz0}^2}{4}\right] - p_0\left[\frac{3\dot{\epsilon}_a S_{a0} - \dot{\epsilon}_b S_{b0}}{2} + \dot{\gamma}_{rz}\tau_{rz0}\right] \tag{325}$$

$$b_2 = -\frac{K\dot{v}}{2G}\left[\frac{3\dot{\epsilon}_a S_{a0} - \dot{\epsilon}_b S_{b0}}{2} - \dot{\gamma}_{rz}\tau_{rz0}\right] - \frac{p_0}{4}\left[3\dot{\epsilon}_a{}^2 - \dot{\epsilon}_b{}^2 - \dot{\gamma}_{rz}{}^2\right] \tag{326}$$

$$b_3 = -\frac{K\dot{v}}{2G}\left[\frac{3\dot{\epsilon}_a{}^2 - \dot{\epsilon}_b{}^2 + \dot{\gamma}_{rz}{}^2}{4}\right] \tag{327}$$

$$c_0 = p_0^3 \tag{328}$$

$$c_1 = 3p_0^2\frac{K\dot{v}}{2G} \tag{329}$$

$$c_2 = 3p_0\left[\frac{K\dot{v}}{2G}\right]^2 \tag{330}$$

$$c_3 = \left[\frac{K\dot{v}}{2G}\right]^3 \tag{331}$$

and

$$S_{a0} = S_{rr0} + S_{zz0} \tag{332}$$

$$S_{b0} = S_{rr0} - S_{zz0} \tag{333}$$

$$\dot{\epsilon}_a = \dot{\epsilon}_{rr} - \dot{\epsilon}_{zz} \tag{334}$$

$$\dot{\epsilon}_b = \dot{\epsilon}_{rr} - \dot{\epsilon}_{zz} \tag{335}$$

The deviatoric strain rates $\dot{\epsilon}_{rr}, \dot{\epsilon}_{zz}$ and stress components $S_{rr0}, S_{zz0}, \tau_{rz0}$ are as defined before, $p_0$ is the value of the mean stress at the start of the increment.

The cubic equation ( 316) is used to find $t$ when the yield surface intersection occurs for the case of zero rotation. Care is necessary in selecting the appropriate root. For the case of large rotation, the zero rotation solution is used to give an initial estimate of the intersection, which is then refined using a Newton-Raphson iterative scheme.

### 5.10.3 Yield surface correction

When a numerical method is used to update stresses, there is a possibility that the final stress state may lie outside the yield surface. The error associated with such a violation of the yield criterion is cumulative and the offending stress state is normally corrected

back to the current yield surface in order to avoid unacceptable errors in subsequent computations.

Because there is no unique way to scale the stresses, it is usually assumed that the correction is applied along a direction which is normal to the yield surface and yield surface corrections are carried out by keeping the direction of the principal stresses fixed (Carter et al., 1977).

### von Mises plasticity

For the von Mises plasticity, it is possible to derive a set of corrected stresses which guarantee that the stress correction is normal to the current corrected yield surface. The normal correction condition may be written as:

$$\sigma_i^c = \sigma_i + \beta a_i^c \tag{336}$$

where

$$a_i^c = \frac{\partial f}{\partial \sigma_i^c} \tag{337}$$

and $\beta$ is a scale parameter.

By combining this equation and the corrected yield equation as:

$$f(\sigma_i^c) = 0 \tag{338}$$

the corrected stress may be shown to be:

$$\sigma_i^c = p + \frac{\sigma_i - p}{\Omega} \tag{339}$$

where

$$\Omega = \frac{(\sigma_1 - \sigma_3)^2 + (\sigma_3 - \sigma_2)^2 + (\sigma_1 - \sigma_2)^2}{8 s_{utc}} \tag{340}$$

for von Mises plasticity.

### Matsuoka plasticity

For Matsuoka plasticity, however, the correction procedure which ensures the correction is normal to the corrected yield surface may lead to severe mathematical difficulties, unless a Newton-Raphson strategy is used to solve a single non-linear equation defined by equation ( 336).

Bearing in mind that departure from the yield surface is small, an alternative correction procedure which assumes the correction is normal to the current yield surface defined by uncorrected stresses, is adopted here for simplicity. This assumption leads to the following equation:

$$\sigma_i^c = \sigma_i - \beta a_i \tag{341}$$

where

$$a_i = \frac{\partial f}{\partial \sigma_i} \tag{342}$$

The corrected stresses defined by equation ( 341) may be substituted into the Matsuoka yield function to give a cubic equation in the scale multiplier $\beta$:

$$A_3\beta^3 + A_2\beta^2 + A_1\beta + A_0 = 0 \tag{343}$$

where

$$A_0 = \sigma_1(\sigma_2 - \sigma_3)^2 + \sigma_2(\sigma_1 - \sigma_3)^2 - \sigma_3(\sigma_1 - \sigma_2)^2 - 8\sigma_1\sigma_2\sigma_3 \tan^2\phi_{tc} \tag{344}$$

$$\begin{aligned} A_1 = {} & [(\sigma_2 - \sigma_3)^2 - 4\sigma_2\sigma_3 + 2\sigma_1(\sigma_2 + \sigma_3) - 8\sigma_2\sigma_3 \tan^2\phi_{tc}]a_1 + [(\sigma_1 - \sigma_3)^2 - 4\sigma_1\sigma_3 \\ & + 2\sigma_2(\sigma_1 - \sigma_3) - 8\sigma_1\sigma_3 \tan^2\phi_{tc}]a_2 + [(\sigma_2 - \sigma_1)^2 - 4\sigma_2\sigma_1 \\ & - 2\sigma_3(\sigma_1 - \sigma_2) - 8\sigma_1\sigma_2 \tan^2\phi_{tc}]a_3 \end{aligned} \tag{345}$$

$$\begin{aligned} A_2 = {} & [(a_2 - a_3)^2 - 4a_2a_3 + 2a_1(a_2 + a_3) - 8a_2a_3 \tan^2\phi_{tc}]\sigma_1 - [(a_1 - a_3)^2 - 4a_1a_3 \\ & + 2a_2(a_1 + a_3) - 8a_1a_3 \tan^2\phi_{tc}]\sigma_2 + [(a_2 - a_1)^2 - 4a_1a_2 - 2a_3(a_1 + a_2) \\ & - 8a_1a_2 \tan^2\phi_{tc}]\sigma_3 \end{aligned} \tag{346}$$

$$A_3 = a_1(a_2 - a_3)^2 - a_2(a_1 - a_3)^2 - a_3(a_1 - a_2)^2 - 8a_1a_2a_3\tan^2\phi_{tc} \tag{347}$$

and

$$\tan^2\phi_{tc}^{\epsilon} = \frac{(\sigma_2 - \sigma_3)^2}{8\sigma_2\sigma_3} + \frac{(\sigma_1 - \sigma_3)^2}{8\sigma_1\sigma_3} + \frac{(\sigma_1 - \sigma_2)^2}{8\sigma_1\sigma_2} \tag{348}$$

$$a_1 = [(\sigma_2 - \sigma_3)^2 - 4\sigma_2\sigma_3 + 2\sigma_1(\sigma_2 + \sigma_3) - 8\sigma_2\sigma_3\tan^2\phi_{tc}^{\epsilon}] \tag{349}$$

$$a_2 = [(\sigma_1 - \sigma_3)^2 - 4\sigma_1\sigma_3 + 2\sigma_2(\sigma_1 + \sigma_3) - 8\sigma_1\sigma_3\tan^2\phi_{tc}^{\epsilon}] \tag{350}$$

$$a_3 = [(\sigma_2 - \sigma_1)^2 - 4\sigma_1\sigma_2 + 2\sigma_3(\sigma_1 + \sigma_2) - 8\sigma_1\sigma_2\tan^2\phi_{tc}^{\epsilon}] \tag{351}$$

In the case when one or more principal stresses become positive (i.e. tensile), it is not possible to correct the stresses back to the yield surface using the approach described above since an appropriate yield surface defined by uncorrected stresses does not exist. This situation is dealt with by correcting the stresses back to the origin of stress space, a procedure that may be justified by the fact that tensile stresses arise only when the magnitude of the stress is very small.

# Chapter 6

# Two Dimensional Finite Element Parametric Studies of Pressuremeter Tests

## 6.1 Introduction

In the early stage of development of pressuremeters, the results of pressuremeter tests were interpreted by means of empirical expressions to give parameters for design such as allowable bearing capacity factors and moduli for allowable settlement. The first fundamental interpretation of an expansion test was published by Gibson and Anderson (1961) in which the pressuremeter was considered to be infinitely long so that the deformation of the surrounding soil was assumed to be in conditions of axial symmetry and plane strain. The interpretation was developed for both undrained expansion tests in clay and expansion tests in cohesionless soils, for which the soil is assumed to behave elastically until failure occurs at a constant effective stress ratio and with no volume change.

Over the last two decades, both of these analyses have been improved. The undrained expansion test can be interpreted without a prerequisite assumption of stress-strain relationship for the soil being tested (e.g. Palmer, 1972). However this approach has been found to be very sensitive to the disturbance of the soil caused by installation, and the resulting uncertainty about the reference strain. By comparison, it is well accepted that the

original Gibson and Anderson analysis is preferable in deriving undrained shear strength as recommended by Mair and Wood (1987). It is recognised, however, that it often leads to overestimation of undrained strength.

As far as the drained expansion test is concerned, the analysis was modified by Hughes, Wroth and Windle (1977) to account for soil dilation. From the analysis the strength parameters and shear modulus can be derived from the test. The relevance of this new analysis to pressuremeter tests in sand was confirmed by Fahey (1980) by a special series of laboratory tests under carefully controlled conditions.

Although the Gibson and Anderson analysis and Hughes et al's analysis have been widely used to interprete self-boring pressuremeter tests in clay and sand respectively, significant uncertainty remains due to the effects of finite length of pressuremeters and the simple stress-strain relationship assumed in the analysis. There are possible errors due to disturbance created by the insertion of the probe into the ground. The degree of disturbance and its influence on the test results is believed to be large and of unknown magnitude (Jamiolkowski et al., 1985). A possible alternative to self-boring pressuremeters, in which the aim is to install the pressuremeter in the ground with minimal disturbance, is to allow a repeatable amount of ground disturbance prior to the pressuremeter test. The installation of the pressuremeter behind a solid tip, which is driven in or pushed into the ground, should result in such a repeatable disturbance. This is why the cone-pressuremeter has attracted a lot of attention over last few years (Withers et al., 1986). Houlsby and Withers (1988) published an analysis by which undrained shear strength and stiffness can be deduced from the test data. In theory the horizontal stress can also be derived, but this approach was found to give excessive values for the horizontal stress. The assumption of cylindrical cavity expansion theory could well be the major source of the errors in derived soil properties, although a length/diameter ratio of 10 was used for cone-pressuremeter tests.

The literature contains several well-documented reports of tests on clays with the self-boring pressuremeter. Results indicate important disagreement with the results of good laboratory tests or other in-situ tests. Baguelin et al. (1972) reported that the soil strength determined by the pressuremeter is 50% larger than in-situ vane strengths for the

Saint-Andre-de-Cubzak clay. Pressuremeter tests on South Gloucester clay (Eden and Law, 1980) yielded strengths about 85% and 20% larger than the vane and conventional triaxial strengths respectively. Consistently higher undrained strength and modulus values from pressuremeter tests, compared to those from laboratory or other field tests were also reported by Wroth and Hughes (1974), Baguelin et al.(1978), Ghionna et al.(1981), Fahey and Carter (1986) and Lacasse et al. (1990), among others.

In cohesionless soils, friction angles obtained from pressuremeter tests using Hughes et al.'s method are typically larger than those from empirical approaches used with the cone penetrometer (see, for example, Hughes et al., 1977; Bruzzi et al., 1986). This difference may be due to the combined effects of finite length of pressuremeter probes and different soil stress paths generated by pressuremeter tests and cone pentrometer tests.

In this chapter, a series of parametric studies on pressuremeter tests was carried out using the finite element formulation developed in Chapter 5. The main objective of the parametric studies is to quantify the effects on derived soil parameters of pressuremeter geometry and soil stress-strain relationships.

## 6.2 Verification of the finite element formulation

### 6.2.1 A small strain thick cylinder problem

In order to investigate the effects of incompressibility on the quality of stress data calculated using the displacement finite element formulation developed in Chapter 5, the analysis of a small strain thick cylinder problem was carried out. The problem consisted of a thick-walled cylinder, with inner radius $a$ and outer radius $b$, subjected to an internal pressure $P$. To isolate possible errors due to the non-linear solution algorithm, a material with infinite strength has been assumed so as to ensure a purely linear elastic response. The expansion of an infinitely long cylinder was modelled by prescribing a plane strain condition in the vertical direction. The mesh used for calculation is shown in Figure 26. A Poisson's ratio of 0.49 was used to approximate incompressible material behaviour. The expansion of the cylinder was carried out by applying a radial pressure along the

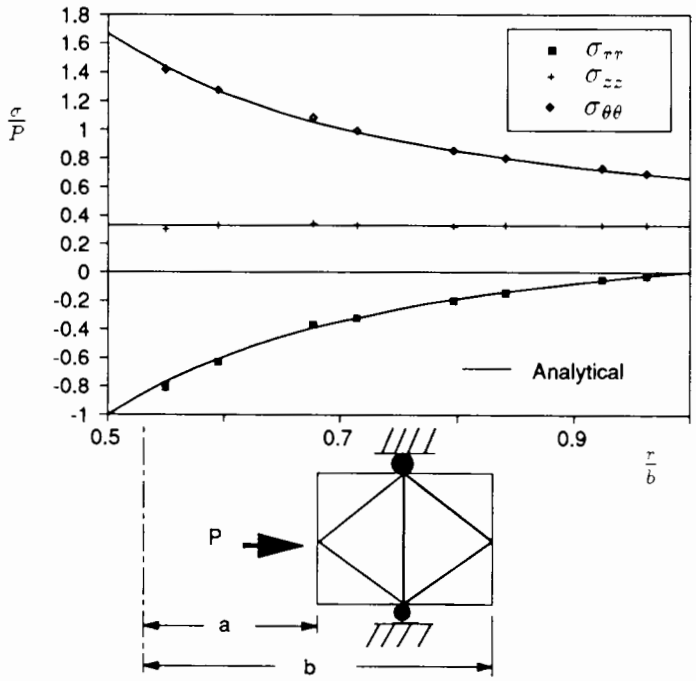


Figure 26: Finite element mesh and results for cylinder expansion

inner boundary of the cylinder.

The computed stresses were normalised by the applied internal pressure $P$ and plotted in Figure 26. The analytical solutions by Hill (1950) are also shown in the same diagram. It is found that the finite element results approximate closely the exact solutions for the perfectly incompressible case.

### 6.2.2 Large strain cavity expansion problems

As a further investigation into the effects of incompressibility constraints on finite element analyses, two large strain cavity expansion problems have been studied. These problems represent severe tests for the finite element formulation since they include the analysis of material that has yielded, as well as including large displacement effects.

#### Cylindrical cavity expansion in infinite von Mises materials

The expansion of a cylindrical cavity in an infinite von Mises material is one of few examples of a large strain elastic-plastic problem with a known closed form solution for the stresses (Sagaseta, 1984).

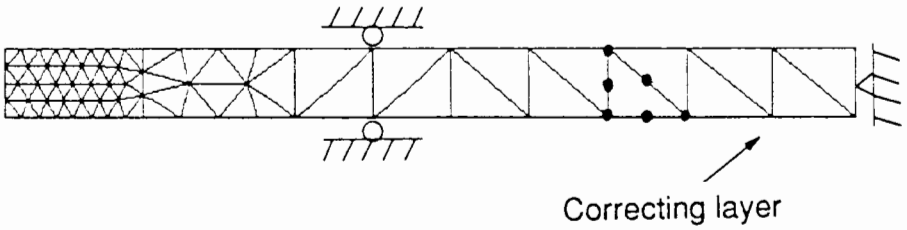


Figure 27: Finite element mesh for cavity expansion

The theoretical analysis assumes a continuum of infinite extent. In order to model this using a mesh of finite dimensions, a correcting layer is added to the perimeter of the mesh (Burd, 1986). Burd shows that if $a$ is the outer radius of the mesh, it is possible to simulate correctly the material behaviour of the infinite medium with a radius $a$ from the axis by the addition of a correcting layer with outer radius of $b$ provided that the following relationship is satisfied.

$$\frac{G^*}{G} = \frac{[(\frac{b}{a})^2 - 1](1 - 2\nu^*)}{1 + (\frac{b}{a})^2(1 - 2\nu^*)} \tag{352}$$

where $G$ is shear modulus of the continuum and $G^*$ and $\nu^*$ are the shear modulus and Poisson's ratio of the correcting layer.

The mesh used for the finite element calculation is shown in Figure 27. The soil was assumed to have a rigidity index of 50, where the rigidity index is defined as ratio of shear modulus and undrained shear strength. Again a Poisson's ratio of 0.49 was used to approximate the incompressibility condition used for the analytical solution. In this study, an expansion ratio of four was applied to the cavity.

The comparison of the finite element calculated stresses with the analytical solution is found to be remarkably good as shown in Figure 28.

### Cylindrical cavity expansion in Matsuoka materials

The objective of the analysis described now is to investigate the capability of the finite element program for calculations of cohesionless material behaviour involving large strain. The mesh used for the large strain cavity expansion in von Mises materials has

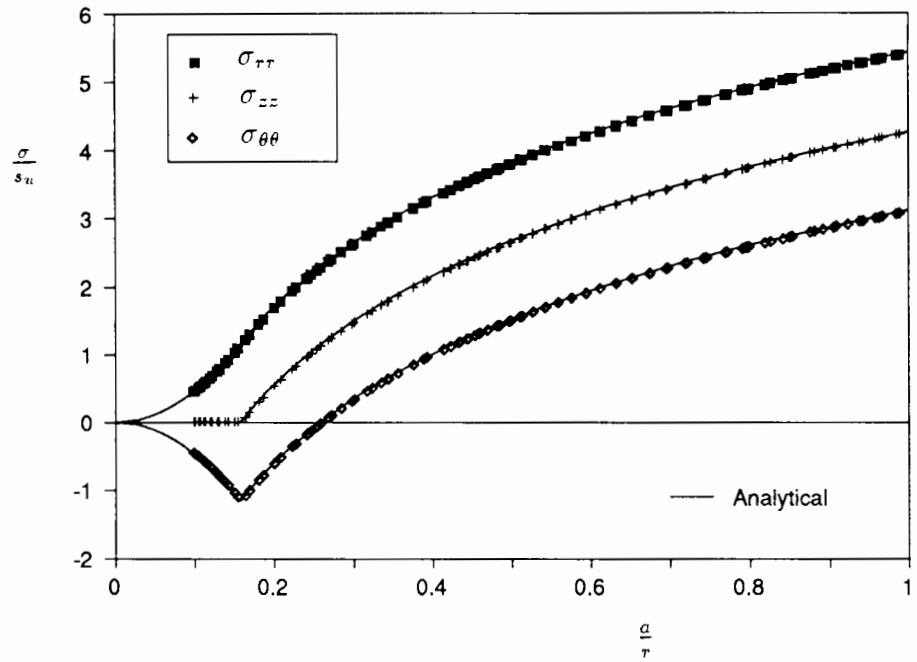


Figure 28: Comparison of stresses from finite element solution and analytical solution

been retained. The material behaviour was described by a stiffness index of $\frac{G}{P_0} = 50$ and a Poisson's ratio of 0.2. The triaxial friction angle and dilation angle were assumed to be $35.83^0$ and $6.15^0$, which correspond to the plane strain friction angle and dilation angle of $40^0$ and $7.10^0$ respectively. A radial displacement controlled analysis was used in the finite element calculation.

The load-displacement curve from the finite element analysis is shown in Figure 29. The cavity pressure, $P$, is normalised by the initial stress $P_0$. Plotted in the same diagram is the analytical pressure-displacement solution for finite cavity expansion in Mohr-Coulomb materials, as described in Chapter 2. A very good comparison between the finite element solution and the analytical solution has been observed.

### 6.2.3 Small strain collapse load analyses

It is well known that finite element plasticity solutions often become highly inaccurate in the fully plastic range. This difficulty is associated with the conflict between finite element discretization and plastic flow rule (Sloan, 1981). Since the analysis of the cone pressuremeter tests is a large strain problem where a large volume has yielded, it is

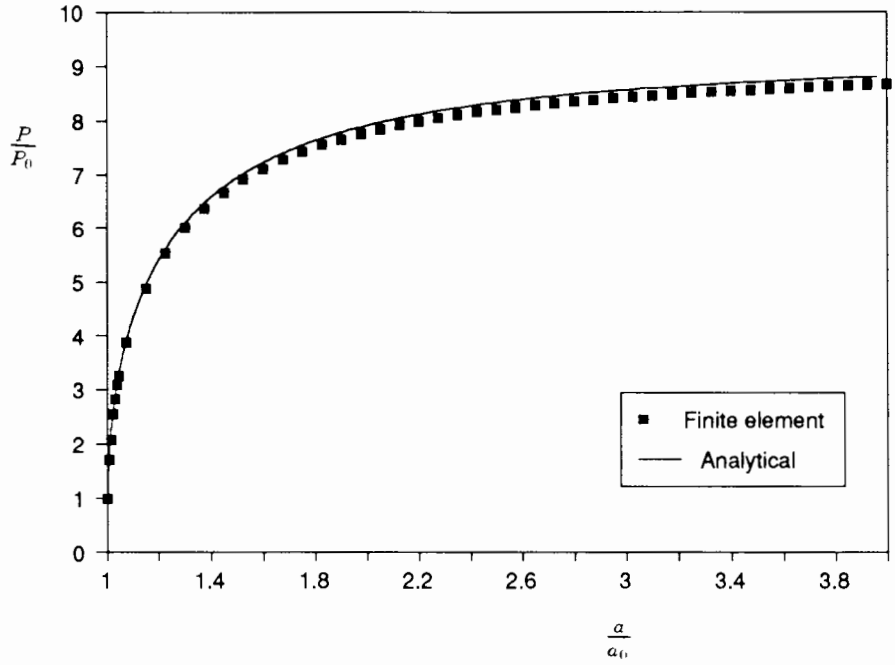


Figure 29: Comparison of pressure-displacement curve from the finite element solution and analytical solution

necessary to check that the proposed finite element formulation is capable of predicting collapse loads for materials in which incompressibility or constant dilation rate constraints are present.

In all the calculations presented in this section, the mesh shown in Figure 30 has been used. The semi-infinite soil mass is modelled by a square mesh with each side equal to 10B, where B is the radius of the footing. Around the edge of the footing, a refined mesh system is used to correctly model the high stress gradients and failure mechanism. Note the slightly curved element edges, since they are straight in the generalized $(R, z)$ space which is defined in Chapter 5.

### Circular smooth footing in von Mises materials

A collapse load calculation for a smooth footing resting on weightless von Mises soils has been performed. In the calculation, a uniform vertical displacement was prescribed to the footing base and horizontal movement of the nodes in contact with the footing was left free to simulate a smooth footing. The resulting load displacement curve is

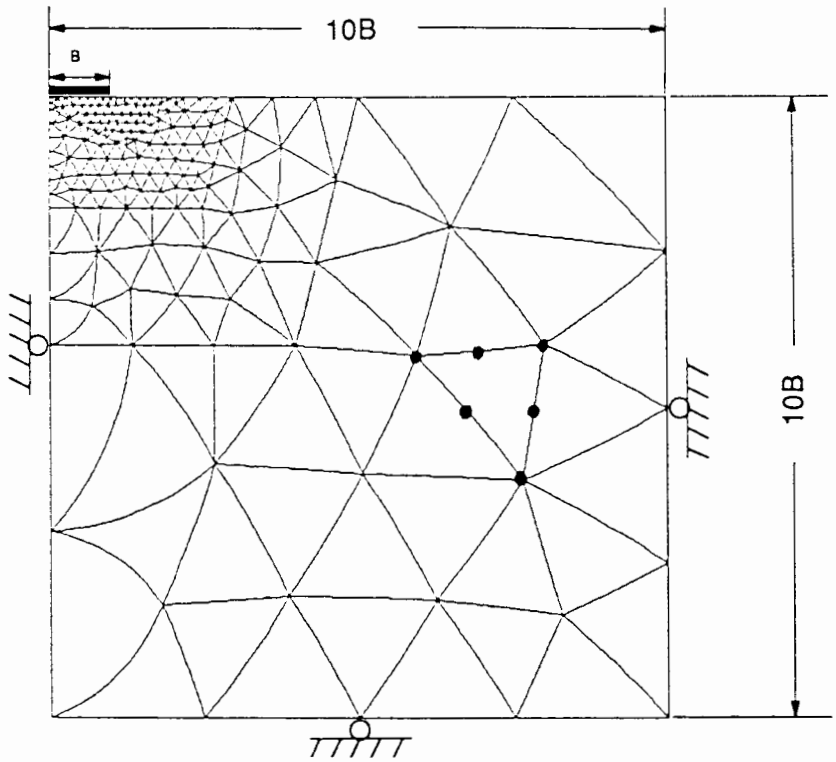


Figure 30: Finite element mesh for collapse load analyses

plotted in Figure 31. For a perfectly plastic von Mises material, no exact collapse load is known. However the collapse load must be greater than the solution obtained for a Tresca material (Shield, 1955; Chen, 1975) and less than the solution for the Tresca material multiplied by a factor of $\frac{2}{\sqrt{3}}$. This is because in triaxial stress states the von Mises yield surface is equivalent to the Tresca yield surface and in plane strain conditions the von Mises yield surface represents the Tresca surface scaled by a factor of $\frac{2}{\sqrt{3}}$. The stress state created by loading a circular footing corresponds neither to a triaxial stress state nor plane strain conditions. As shown in Figure 31, the finite element analysis yields a collapse load which is between these two collapse loads for triaxial stress states and plane strain conditions.

### Circular smooth footing in Matsuoka materials

A collapse load calculation involving a smooth footing on frictional soils with surcharge has been performed in order to check the capability of the proposed finite element formulation in modelling materials with dilation. The Matsuoka plasticity formulation described in Section 5.8 was used to represent the soil, and a triaxial friction angle of $26.29^0$ was

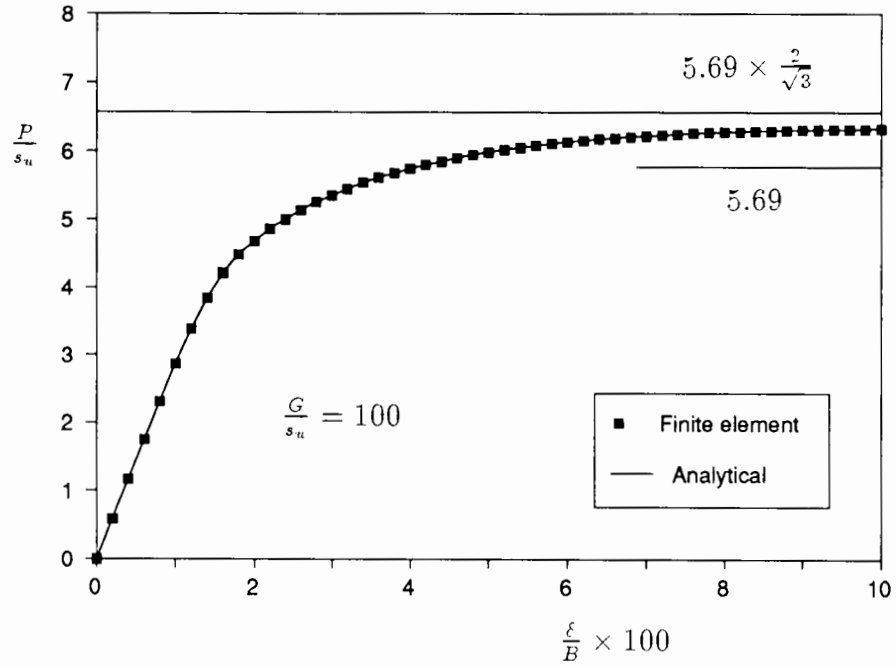


Figure 31: Numerical footing pressure-displacement curve for von Mises material

used in conjunction with an associated flow rule, which corresponds to a plane strain friction angle of $30^0$. For the collapse load problem, it is well known that the collapse load is relatively independent of dilation angle. Therefore, it does not really matter what value of dilation is used. The Poisson's ratio was assumed to be 0.2 and the initial stress state was assumed to be isotropic.

The load displacement curve obtained from the finite element analysis is plotted in Figure 32 and the resulting collapse load is comparable to the theoretical value obtained by the slip line theory for a Mohr-Coulomb material with a plane strain friction angle of $30^0$ (Houlsby, 1990). The slight oscillation observed before the limit state may be due to the finite element discretization and could be eliminated by using a refined mesh in the calculation.

## 6.3 Finite element modelling of pressuremeter tests

The application of the proposed finite element formulation to the analysis of pressuremeter tests is described in this section. A series of parametric studies has been carried out

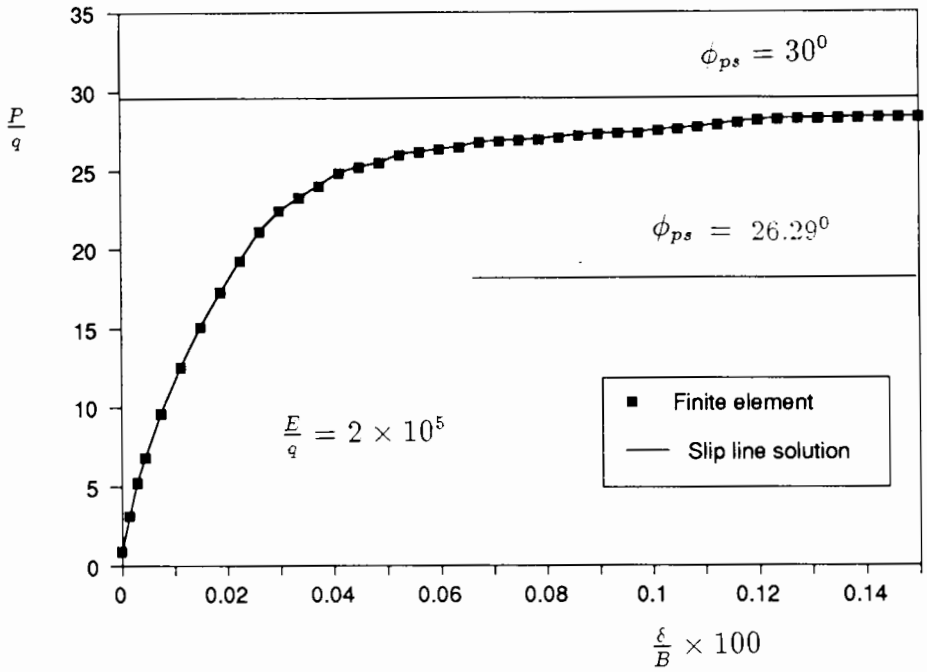


Figure 32: Numerical footing pressure-displacement curve for Matsuoka material

for self-boring pressuremeter tests in both clay and sand and cone-pressuremeter tests in clay. The parameters investigated include the pressuremeter geometry, the soil rigidity index and soil density.

The self-boring pressuremeter was assumed to be installed deep into the ground without any disturbance and the initial soil stress state was assumed unchanged by the installation of the pressuremeter. When modelling the cone-pressuremeter test, the installation was modelled as a cylindrical cavity expansion process and the pressuremeter expansion was modelled by the two dimensional finite element method. In other words, stresses derived from cavity expansion were used as initial stresses when modelling the cone-pressuremeter expansion tests, which have been pushed into the ground. As pointed out by Houlsby and Withers (1988), this modelling of the installation will be somewhat in error, as the penetration of a rod tipped by a $60^0$ cone involves different stress paths from the cavity expansion. However the analysis using the Strain Path Method (Teh, 1987; Teh and Houlsby, 1988) shows that the stress distribution far behind the cone tip is similar to the distribution created by the expansion of a cylindrical cavity from zero initial radius. The use of the simpler cylindrical cavity expansion theory is therefore justified,

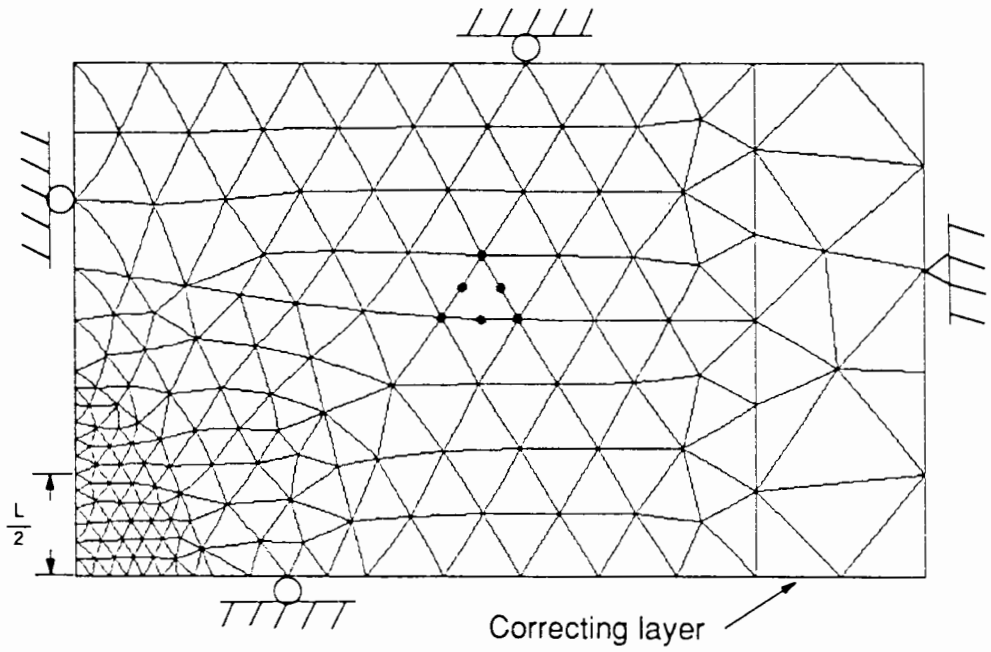


Figure 33: Finite element mesh used for simulation of pressuremeter tests

provided that the bottom of the pressuremeter section is located more than about 10 diameters behind the cone tip.

In order to isolate effects due to the finite length of the pressuremeter from possible numerical errors due to the non-linear solution algorithm, a calibration calculation with an infinitely long pressuremeter was carried out for each pressuremeter test with a finite length of probe. Figure 33 shows a mesh for real pressuremeter calculations which consists of 288 modified 6 node triangular elements and the mesh shown in Figure 27 is used for infinitely long pressuremeter calculations. Care was taken in designing these meshes so that possible regions with higher stress gradients have a higher density of elements. The pressuremeter membrane was modelled by 6 elements and boundary conditions used in calculations are shown in Figure 33.

A fixed ratio of the total height of mesh to half length of the pressuremeter has been used and different length to diameter ratios are obtained by multiplying the vertical coordinate of all meshes by a certain factor. The material behaviour of the infinite medium was simulated by a correcting layer for which the continuum properties and the correcting layer properties are related by Equation ( 352).

The analytical stress solution for cavity expansion in the von Mises material developed by Sagaseta (1984) using large strain theory throughout both elastic and plastic regions has been used to approximate the stress state due to the installation of the cone-pressuremeter test in clay.

In the analysis of self-boring pressuremeter tests, a small strain finite element formulation was adopted because the maximum cavity strain used in self-boring pressuremeter tests is not large. When modelling cone-pressuremeter tests, large soil rotations around the membrane edge are expected because the maximum cavity Hencky strain could be up to 40%. Therefore it is necessary to use a large strain finite element formulation to account for the large soil rotation and geometry change.

## 6.4 Analysis of self-boring pressuremeter tests in clay

### 6.4.1 Parameters for the analysis

Whilst the self-boring pressuremeter eliminates or reduces the problems associated with sampling and laboratory testing, the design parameters deduced from the tests are based on the shape of the expansion curve which may be affected by many factors. For tests carried out relatively quickly in clay, it is assumed that idealised undrained conditions exist although some dissipation of pore pressure will inevitably occur. The effects of partial drainage on the pressuremeter tests have been studied by a number of researchers (see, for example, Pyrah and Anderson, 1990; Fukagawa et al., 1990).

To quantify the effects due to the finite length of pressuremeter probes, numerical simulations of self-boring pressuremeter tests in clay have been carried out using the axisymmetric finite element method developed in Chapter 5. The soil mass has been idealised as an elastic-perfectly plastic medium which obeys the von Mises yield criterion and deforms under constant volume conditions. Pressure controlled 'quick' expansion tests were simulated and each test was continued to a cavity strain $\epsilon = 10\%$ for centre of pressuremeter membrane. Effects due to finite stiffness of membrane are ignored in this study.

Table 6.1 summarises all values of the key parameters varied in the numerical simulations. An isotropic initial stress state with zero value for all stress components was assumed.

Table 6.1 Numerical tests of self-boring pressuremeter in clay

| $\frac{L}{D}$ \ $I_r$ | 50 | 100 | 200 | 300 | 500 |
|---|---|---|---|---|---|
| 4 | F8 | F12 | F16 | F20 | F4 |
| 6 | F7 | F11 | F15 | F19 | F3 |
| 8 | F6 | F10 | F14 | F18 | F2 |
| $\infty$ | F5 | F9 | F13 | F17 | F1 |

Figure 34 shows a typical set of results of numerical simulations of the self-boring pressuremeter test in clay. The pressure-expansion curve from each numerical simulation was interpreted as if it were derived from a real field test, using the standard technique proposed by Gibson and Anderson. The shear modulus $G$ has been derived from the initial pressure-expansion curve over the range $\psi = 0 - s_u$, which is the elastic range for the Tresca material. For the von Mises material used in this section, the elastic range is expected to be even larger than that for the Tresca model. With respect to determination of shear strength, two approaches were recommended by Mair and Wood (1987). The plot of $\psi$ against $\ln \epsilon_v$ is usually used to define $s_u$, which can either be estimated from the slope of the curve or the extrapolated limit pressure at $\frac{V-V_0}{V} = 1$. As pointed out by Mair and Wood, strengths obtained with the limit pressure method appear to be less sensitive to the assumed reference conditions, and hence less sensitive to disturbance associated with installation of the pressuremeter. Both of these approaches have been used to derive undrained shear strength from the expansion curve for comparisons. In order to investigate possible effects of using different volumetric strain definitions, two different ways of deriving it namely, $\epsilon_v = 2\ln(\frac{a}{a_0}), \epsilon_v = \ln(\frac{V}{V_0})$ were used, where $a, a_0$ are the current and initial radius of the middle point of the pressuremeter membrane and $V, V_0$ are the current and initial pressuremeter volumes respectively. A least squares method was used to find the slope in deriving the shear strength. Two different strain ranges

measured by strain magnitude of the middle point of the membrane (i.e. $\epsilon_c = 2 - 5\%$ and $\epsilon_c = 2 - 10\%$) were chosen for deducing the undrained shear strength so that the analysis may be objective and possible effects due to different strain ranges used for deriving the undrained shear strength could be quantified.

When the undrained shear strength is estimated from the limit pressure by extrapolation, the so-called Menard limit pressure is used for interpretation. The Menard limit pressure is defined as the pressure at which $\frac{V}{V_0} = 2$, corresponding to $\frac{a}{a_0} = \sqrt{2}$. The choice of Menard limit pressure instead of the true limit pressure at which $\frac{V}{V_0} = \infty$ allows the interpretation to be made using the two different volumetric strain definitions described earlier. In determining the effects due to finite length of pressuremeters, we need to investigate the ratio of limit pressures of pressuremeter tests with an infinitely long probe and those with a finite length. The following expression was assumed:

$$\psi_{lm} = s_u^l(1 - \ln(\frac{G}{s_u^l})) \tag{353}$$

where $\psi_{lm}$ denotes the Menard limit pressure, which is found by extrapolating the expansion curve in the range $\epsilon_c = 5 - 10\%$, and $s_u^l$ represents the undrained shear strength corresponding to the Menard limit pressure. After obtaining $\psi_{lm}$ for each pressuremeter test, equation ( 353) can be used to derive $s_u^l$ using a Newton-Raphson solution scheme.

## 6.4.2 Numerical results

The derived undrained shear strengths for each pressuremeter test are summarised in Table 6.2 and Table 6.3. Table 6.4 shows the derived shear moduli. For all the cases, $s_{utc} = 1.0$ is used which corresponds to a plane strain undrained shear strength of $\frac{2}{\sqrt{3}}$. The derived values of plane strain undrained shear strength from the numerical analyses of the pressuremeter tests with an infinitely long probe are found to be in good agreement with the actual shear strength used in the analysis. The maximum error is found to be less than about 2%. This evidence suggests that the performance of the numerical method used in the analysis is very satisfactory. It is also necessary to note that in Table 6.4 the actual values of shear moduli used in the analysis are equal to the values of rigidity

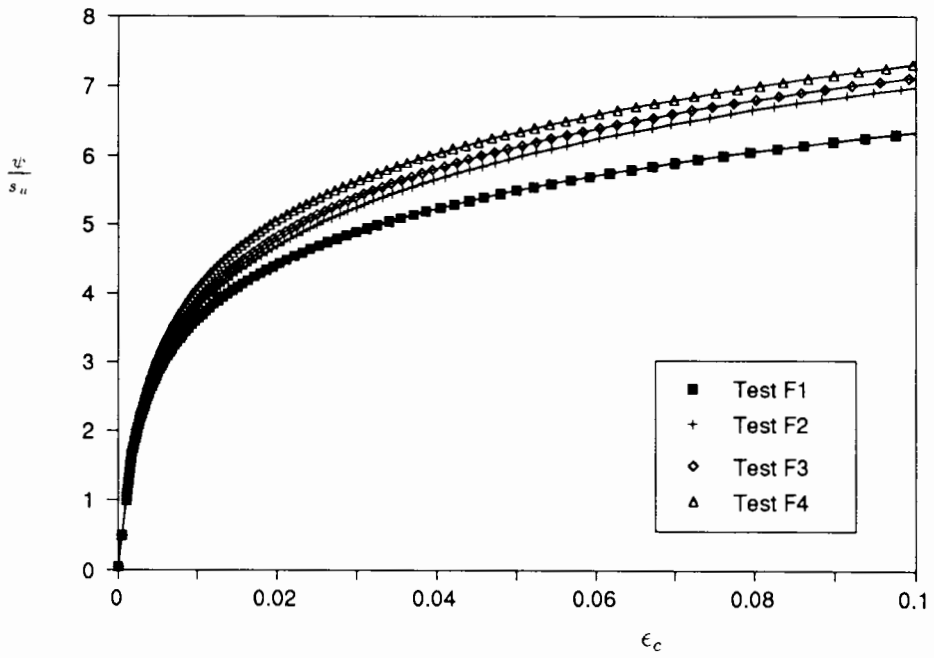


Figure 34: A typical set of results for numerical simulations of the self-boring pressuremeter test in clay

index (i.e. $I_r = \frac{G}{s_{utc}}$ ) listed in the Table because a value of unity for $s_{utc}$ is used in the calculation.

In general it can be seen that the use of conventional one dimensional cavity expansion theory to pressuremeter tests with finite length of probes tends to overestimate both undrained shear strength and shear moduli. When the volumetric strain is defined by twice central strain of the membrane, the overestimation of shear moduli was found to be negligible even for the pressuremeter tests with a length/diameter ratio of 4. Significant overprediction of shear moduli was observed, however, when the volumetric strain is calculated from the actual volume of the pressuremeter membrane. As far as undrained shear strength is concerned, the numerical results suggest that the overestimation due to the finite length/diameter ratio, using the approach of deriving undrained shear strength from the slope of logarithmic plot of expansion curve, largely depends on the rigidity index of the soil. The rigidity index is defined as ratio of shear modulus to undrained shear strength. By comparison, it is interesting to note that the effect on undrained shear strength due to pressuremeter geometry, using the approach of deducing undrained shear strength from the limit pressure, are relatively independent of the rigidity index. The

following sections are devoted to examining the variation of the length/diameter ratio effects with different parameters for the pressuremeter tests.

Table 6.2 The derived shear strength for self-boring pressuremeter test in clay using loading slope

| $\frac{L}{D}$ | $I_r$ | 50 | | 100 | | 200 | | 300 | | 500 | |
|---|---|---|---|---|---|---|---|---|---|---|---|
| | $\epsilon_c$ | 2 – 5% | 2 – 10% | 2 – 5% | 2 – 10% | 2 – 5% | 2 – 10% | 2 – 5% | 2 – 10% | 2 – 5% | 2 – 10% |
| 4 | $s_{uv}$ | 1.3227 | 1.3506 | 1.3546 | 1.3673 | 1.3625 | 1.3686 | 1.3582 | 1.3653 | 1.3563 | 1.3627 |
| | $s_{uc}$ | 1.3434 | 1.4057 | 1.4312 | 1.4553 | 1.4530 | 1.4430 | 1.4307 | 1.4172 | 1.3947 | 1.3884 |
| 6 | $s_{uv}$ | 1.2692 | 1.3055 | 1.3141 | 1.3330 | 1.3390 | 1.3583 | 1.3518 | 1.3668 | 1.3624 | 1.3705 |
| | $s_{uc}$ | 1.2514 | 1.3077 | 1.3297 | 1.3777 | 1.4042 | 1.4309 | 1.4264 | 1.4358 | 1.4269 | 1.4217 |
| 8 | $s_{uv}$ | 1.2329 | 1.2776 | 1.2883 | 1.3017 | 1.3046 | 1.3328 | 1.3261 | 1.3510 | 1.3478 | 1.3648 |
| | $s_{uc}$ | 1.2144 | 1.2582 | 1.2648 | 1.3123 | 1.3404 | 1.3842 | 1.3798 | 1.4130 | 1.4125 | 1.4264 |
| $\infty$ | $s_{uv}$ | 1.1488 | 1.1707 | 1.1676 | 1.1777 | 1.1666 | 1.1787 | 1.1689 | 1.1793 | 1.1697 | 1.1814 |
| | $s_{uc}$ | 1.1555 | 1.1744 | 1.1664 | 1.1769 | 1.1666 | 1.1784 | 1.1686 | 1.1790 | 1.1695 | 1.1812 |

Table 6.3 The derived shear strength for self-boring pressuremeter test in clay using limit pressure

| $\frac{L}{D}$ | $I_r$ | 50 | 100 | 200 | 300 | 500 |
|---|---|---|---|---|---|---|
| 4 | $s^l_{uv}$ | 1.2857 | 1.3099 | 1.3096 | 1.3091 | 1.3104 |
| | $s^l_{uc}$ | 1.2689 | 1.3045 | 1.3022 | 1.3005 | 1.3073 |
| 6 | $s^l_{uv}$ | 1.2270 | 1.2478 | 1.2692 | 1.2734 | 1.2808 |
| | $s^l_{uc}$ | 1.1938 | 1.2303 | 1.2545 | 1.2598 | 1.2762 |
| 8 | $s^l_{uv}$ | 1.1690 | 1.2057 | 1.2363 | 1.2395 | 1.2483 |
| | $s^l_{uc}$ | 1.1363 | 1.1779 | 1.2072 | 1.2260 | 1.2483 |
| $\infty$ | $s^l_{uv}$ | 1.0395 | 1.0491 | 1.0798 | 1.0844 | 1.0938 |
| | $s^l_{uc}$ | 1.0474 | 1.0491 | 1.0745 | 1.0844 | 1.0923 |

Table 6.4 The derived shear moduli for self-boring pressuremeter test in clay

| $\frac{L}{D}$ | $I_r$ | 50 | 100 | 200 | 300 | 500 |
|---|---|---|---|---|---|---|
| 4 | $G_v$ | 58.5628 | 116.8647 | 233.4681 | 350.0718 | 583.2787 |
| | $G_c$ | 49.8962 | 99.5284 | 198.7926 | 298.0567 | 496.5849 |
| 6 | $G_v$ | 55.0649 | 109.8705 | 219.4812 | 329.0920 | 548.3132 |
| | $G_c$ | 48.9956 | 97.7274 | 195.1905 | 292.6537 | 487.5797 |
| 8 | $G_v$ | 53.4678 | 106.6770 | 213.0952 | 319.5133 | 532.3491 |
| | $G_c$ | 48.8132 | 97.36259 | 194.4609 | 291.5592 | 485.7556 |
| $\infty$ | $G_v$ | 48.1071 | 95.9503 | 191.6364 | 287.3225 | 478.6946 |
| | $G_c$ | 48.5762 | 96.8885 | 193.5128 | 290.1371 | 483.3856 |

### 6.4.3 Effects of length to diameter ratio

The effects of length to diameter ratio on derived soil properties may be examined in detail by considering the case where the rigidity index is equal to 100. The ratio of derived parameters from pressuremeter tests with an infinitely long membrane to derived parameters from pressuremeter tests with a finite length of membrane was used to measure the effects of finite length.

The variation of the effects on stiffness, due to the finite length of pressuremeter probe, with length to diameter ratio is shown in Figure 35. It can be seen that the membrane end effects for the case when volumetric strain is calculated from the volume of the pressuremeter are more significant than the case when volumetric strain is assumed to be twice the central strain of the membrane. For the pressuremeter tests with a length to diameter ratio of 6, the overestimation of shear modulus is about 13% when the volumetric strain is calculated from volume of pressuremeter.

As far as the shear strength is concerned, different ways of deriving the strength were distinguished. The variation of the effects due to finite length of pressuremeter with length to diameter ratio is shown in Figure 36 to Figure 37 for different ways of

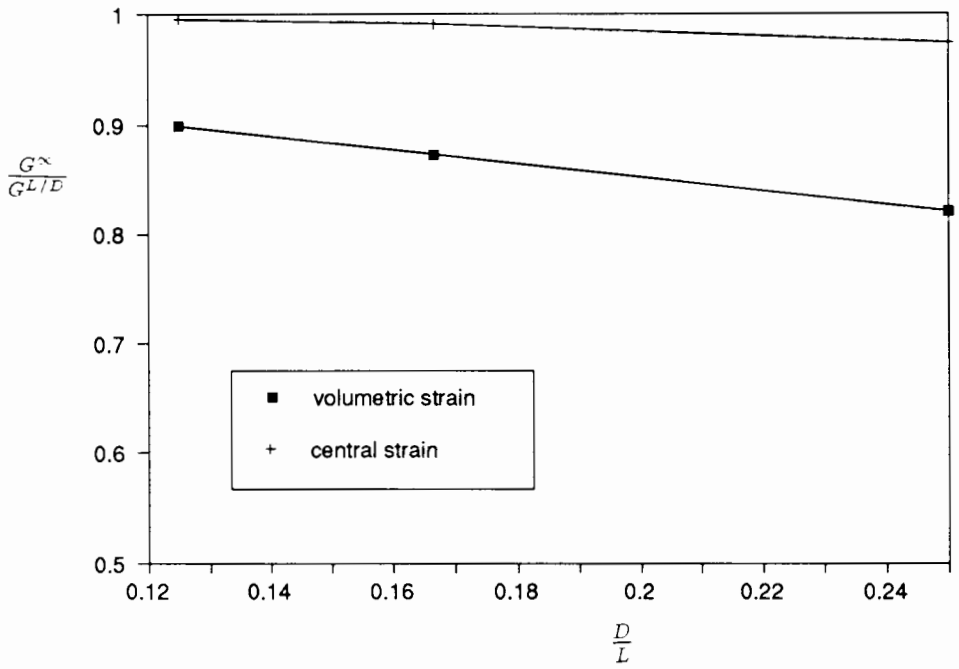


Figure 35: Effects on shear modulus due to length to diameter ratio

calculating the volumetric strain. It can be seen that the effects of finite length of the pressuremeter increases when the length to diameter ratio decreases.

### 6.4.4 Effects of soil rigidity index

Five different values of rigidity index, denoted by $I_r$, have been used in the numerical calculations so that the possible effects due to variation of rigidity index on the derived soil properties may be fully quantified. To isolate the effects of rigidity index from the effects due to different length to diameter ratios, the case when the length to diameter ratio is equal to 6 was chosen to highlight the importance of rigidity index.

From Table 6.4, it is easily noticed that the variation of effects on shear modulus, due to the finite length of pressuremeter probes, with rigidity index is very small, and could be neglected in practice.

The numerical results of the effect on undrained strength due to finite length of pressuremeters for the case when length to diameter ratio is equal to 6 are shown in Figure 38 to Figure 39 for two different ways of deriving the volumetric strain used in the analysis. It can be seen that the ratio of the derived undrained shear strength for

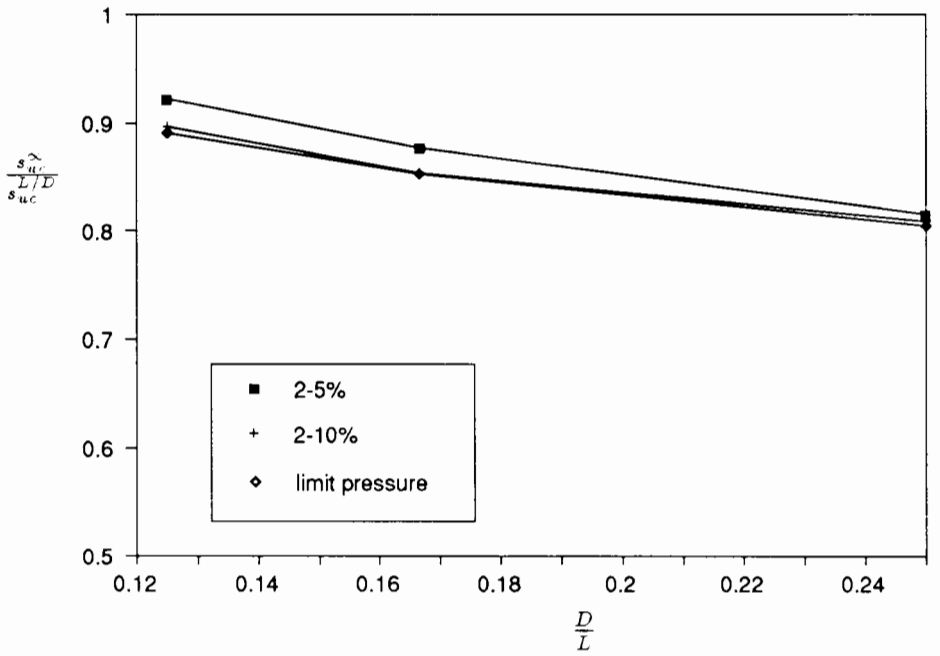


Figure 36: Effects on strength due to finite length using central strain

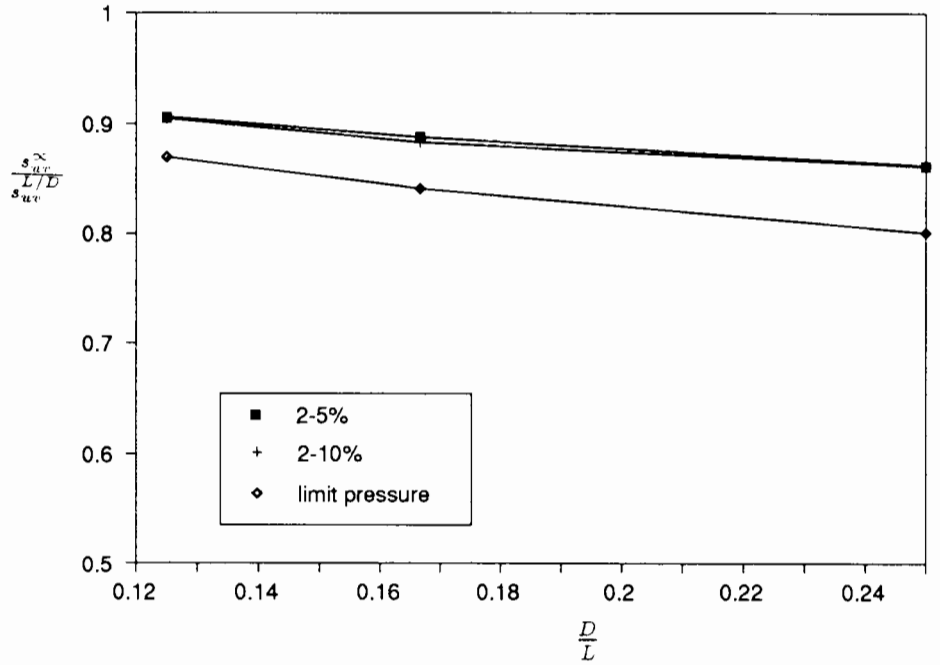


Figure 37: Effects on strength due to finite length using volumetric strain

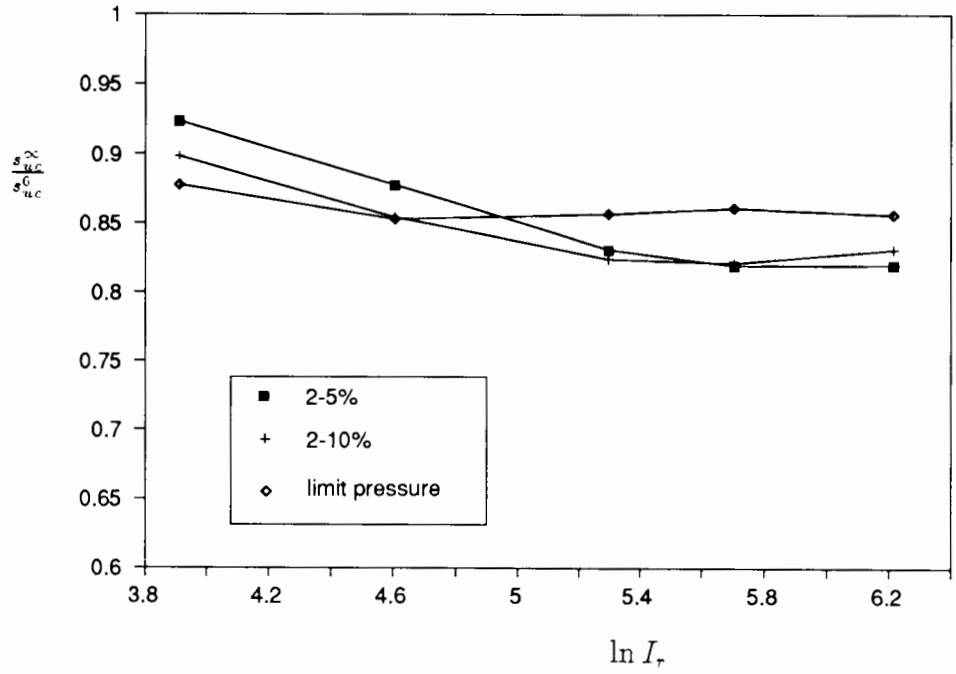


Figure 38: Variation of finite length effects on strength with rigidity index using central strain

pressuremeter tests with an infinitely long probe to the derived shear strength for the pressuremeter tests with a length to diameter ratio of 6 is less than unity for all cases.

It suggests that the use of the conventional one dimensional interpretation method for the real pressuremeter tests with a finite length tends to overestimate the 'true' undrained shear strength. It is interesting to see that the effects due to finite length are relatively independent of the rigidity index if the undrained shear strength is derived from the limit pressure. The average overestimation of undrained shear strength for this case is about 15%. For the case when the undrained shear strength is deduced from the slope of pressuremeter expansion curve, the finite length effects increase with the rigidity index.

## 6.5 Analysis of self-boring pressuremeter tests in sand

### 6.5.1 Parameters for the analysis

Two possible sources of error in deriving the fundamental soil parameters from pressuremeter tests in sand, when the conventional Hughes et al's interpretation method is

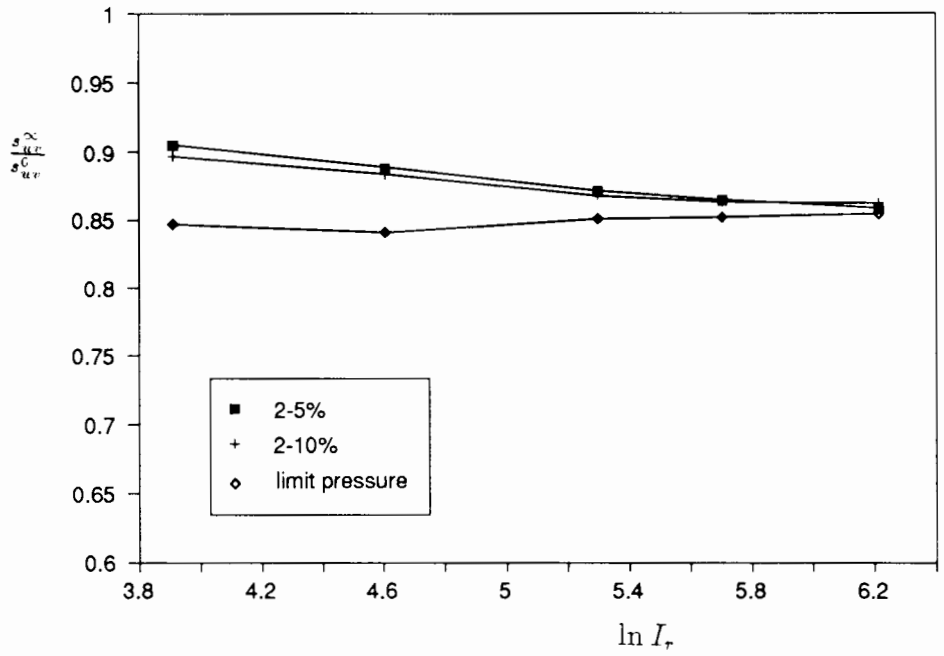


Figure 39: Variation of finite length effects on strength with rigidity index using volumetric strain

applied, are studied in this section. First of all, the pressuremeter geometry assumed in the Hughes et al's analysis may not be appropriate for the field conditions. In practice, the inflatable membrane is of limited length with a finite length to diameter ratio. Another basic assumption made in the analysis regarding the behaviour of the soil is that the elastic deformation in the plastic zone surrounding the cavity is small and may be ignored. The importance of this assumption can be assessed by comparing the analytical solution developed in Chapter 2 which includes elastic deformation, with the Hughes et al's analysis.

Twelve sets of numerical tests were designed to investigate possible effects due to finite length of pressuremeters for different soil density and stiffness. The detailed variation of parameters are shown in Table 6.5 and the initial stress state was assumed to be isotropic. A value of $100kPa$ was assumed for all initial stress components. The correlation between the triaxial parameters used in the Matsuoka plasticity and plane strain parameters used in Mohr-Coulomb model was described in Chapter 5. In this section, a length to diameter ratio of 6 was used for all analyses. Numerical pressuremeter tests with an infinitely long probe were also carried out in order to eliminate possible errors due to the proposed

non-linear solution algorithm. In the analyses, the critical state friction angle with the value of $\phi_{cv} = 33^0$ is assumed for all cases. For a given value of stiffness index (i.e. $I_s = \frac{G}{\sigma_{h0}}$), the possible effects due to friction angles of the soil can be investigated by varying peak friction angles. Friction and dilation angles were assumed to be related by Rowe's stress-dilatancy equation.

Table 6.5 Numerical tests of self boring pressuremeter in sand

| $\phi_{ps}$ | $\frac{L}{D}$ \ $I_s$ | 200 | 500 | 1000 |
|---|---|---|---|---|
| $48^0$ | 6 | D2 | D4 | D6 |
| | $\infty$ | D1 | D3 | D5 |
| $43^0$ | 6 | D14 | D16 | D18 |
| | $\infty$ | D13 | D15 | D17 |
| $38^0$ | 6 | D20 | D22 | D24 |
| | $\infty$ | D19 | D21 | D23 |
| $33^0$ | 6 | D8 | D10 | D12 |
| | $\infty$ | D7 | D9 | D11 |

### 6.5.2 Numerical results

The pressuremeter tests are simulated by applying an uniform radial pressure incrementally across the membrane wall. Each test was continued until the cavity strain reached 5% and the least square method was applied to a strain range of between 1 — 5% to derive the slope of pressuremeter expansion curve in logarithmic scale. Figure 40 shows a typical set of results of numerical simulations of the self-boring pressuremeter test in sand. After obtaining a value of loading slope, the conventional Hughes et al's method was used to backcalculate the friction angle and dilation angle using the input critical state friction angle and Rowe's stress-dilatancy relationship.

Table 6.6 and Table 6.7 show the derived plastic loading slopes and backcalculated strength parameters for all numerical tests. $(S^n_{dc6}, \phi^n_{dc6})$ and $(S^n_{dv6}, \phi^n_{dv6})$ represent the derived loading slopes and friction angles from the pressuremeter tests with $\frac{L}{D} = 6$ using

central strain and volumetric strain measurements respectively, and $(S^n_{dc\infty}, \phi^n_{dc\infty})$ and $(S^n_{dv\infty}, \phi^n_{dv\infty})$ denote the derived loading slopes and friction angles from the pressuremeter tests with $\frac{L}{D} = \infty$ for both central strain and volumetric strain measurements.

Also summarised in the Tables are the loading slopes $S^{te}_{d\infty}$ and friction angles $\phi^{te}_{d\infty}$ for cylindrical cavity expansion when an exact small strain analytical solution is used to produce the expansion curve. The importance of the elastic deformation in the plastic zone may be quantified by comparing these derived parameters with those denoted by $S^{ta}_{d\infty}$ and $\phi^{ta}_{d\infty}$ derived from the cylindrical cavity expansion curve when the elastic compressibility is ignored. The soil parameters were derived using two different plots, namely $\ln v$ against $\ln(\ln(\frac{a}{a_0}))$ and $\ln v$ against $\ln(\frac{1}{2}\ln(\frac{V}{V_0}))$, where $a, a_0$ are the current and initial radius of the middle point of membrane and $V, V_0$ denote current and initial volume of the pressuremeter respectively.

It is evident from Table 6.6 and Table 6.7 that the values of derived parameters $(S^n_{dv\infty}, \phi^n_{dv\infty})$ and $(S^n_{dc\infty}, \phi^n_{dc\infty})$ from the numerical analysis of the infinitely long pressuremeter tests are in remarkably good agreement with the theoretical values of $(S^{te}_{d\infty}, \phi^{te}_{d\infty})$, with a maximum deviation of less than half a percent. This suggests that the numerical method developed in Chapter 5 can be used with confidence for analysing the pressuremeter tests.

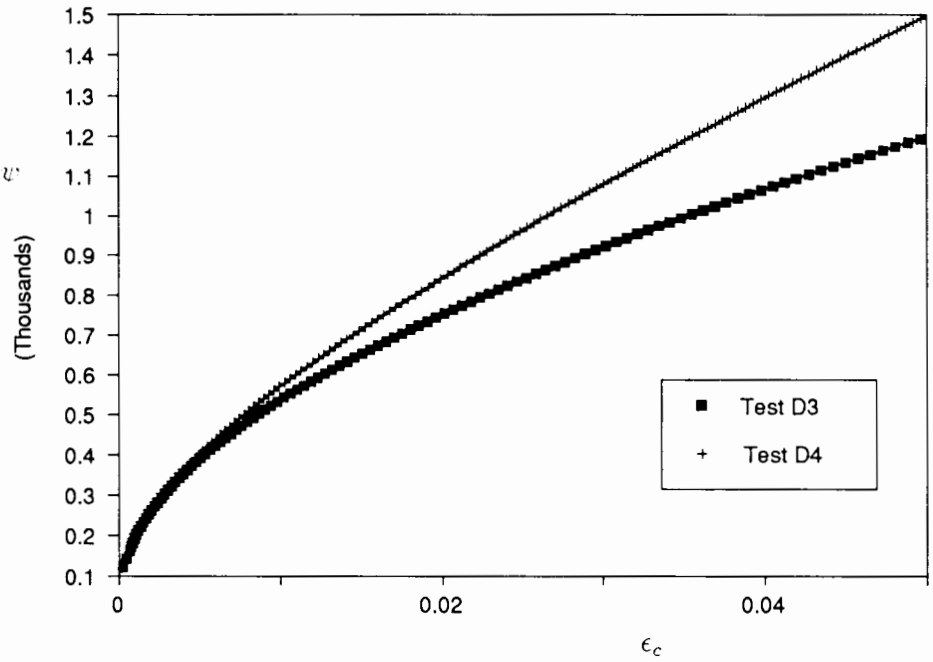


Figure 40: A typical set of results for numerical simulations of the self-boring pressuremeter test in sand

Table 6.6 The derived slopes for self-boring pressuremeter test in sand

| $\phi_{ps}$ | $I_s$ | $S^{ta}_{d\infty}$ | $S^{t\epsilon}_{d\infty}$ | $S^{n}_{dv\infty}$ | $S^{n}_{dc\infty}$ | $S^{n}_{dv6}$ | $S^{n}_{dc6}$ |
|---|---|---|---|---|---|---|---|
| $48^0$ | 200 | 0.5684 | 0.4719 | 0.4740 | 0.4737 | 0.5341 | 0.5355 |
| | 500 | 0.5684 | 0.4955 | 0.4996 | 0.4991 | 0.5907 | 0.6046 |
| | 1000 | 0.5684 | 0.5123 | 0.5162 | 0.5156 | 0.6302 | 0.6495 |
| $43^0$ | 200 | 0.4941 | 0.4249 | 0.4263 | 0.4261 | 0.4837 | 0.4860 |
| | 500 | 0.4941 | 0.4448 | 0.4462 | 0.4458 | 0.5308 | 0.5443 |
| | 1000 | 0.4941 | 0.4573 | 0.4596 | 0.4593 | 0.5636 | 0.5820 |
| $38^0$ | 200 | 0.4218 | 0.3747 | 0.3750 | 0.3749 | 0.4277 | 0.4306 |
| | 500 | 0.4218 | 0.3896 | 0.3911 | 0.3909 | 0.4654 | 0.4778 |
| | 1000 | 0.4218 | 0.3980 | 0.4007 | 0.4005 | 0.4910 | 0.5072 |
| $33^0$ | 200 | 0.3526 | 0.3226 | 0.3222 | 0.3224 | 0.3666 | 0.3696 |
| | 500 | 0.3526 | 0.3327 | 0.3333 | 0.3333 | 0.3967 | 0.4072 |
| | 1000 | 0.3526 | 0.3400 | 0.3405 | 0.3404 | 0.4153 | 0.4286 |

### 6.5.3 Effects of length to diameter ratio

The ratio between the derived parameters for the numerical pressuremeter test with an infinitely long membrane and the derived parameters for the pressuremeter test with a finite length to diameter ratio of 6 may be used to indicate the effects due to finite length of pressuremeters.

Figure 41 and Figure 42 show the ratios of loading slopes derived from the two different plots. It was found that the use of the conventional Hughes et al's approach for the pressuremeter test tends to overestimate the pressuremeter expansion slope for all values of stiffness. The implication of the overestimation of the loading slope may be assessed by using the conventional way to backcalculate friction angle and dilation angle from the derived slopes. The critical state friction angle was assumed to be unchanged due to the pressuremeter geometry in the backcalculations. The significant overestimation of friction angle due to finite length of the pressuremeter can be seen in Figure 43 and Figure 44. In general, it was observed that a slightly smaller overestimation of derived friction angles is suggested by adopting the plot of pressure against volumetric strain than the plot of pressure against the central strain of the membrane. The overprediction of friction angles by ignoring the pressuremeter geometry could be up to 17% for stiff soils.

Table 6.7 The derived friction angles for self-boring pressuremeter test in sand

| $\phi_{ps}^{in}$ | $I_s$ | $\phi_{d\infty}^{ta}$ | $\phi_{d\infty}^{te}$ | $\phi_{dv\infty}^{n}$ | $\phi_{dc\infty}^{n}$ | $\phi_{dv6}^{n}$ | $\phi_{dc6}^{n}$ |
|---|---|---|---|---|---|---|---|
| $48^0$ | 200 | $48.0^0$ | $41.49^0$ | $41.63^0$ | $41.61^0$ | $45.70^0$ | $45.80^0$ |
| | 500 | $48.0^0$ | $43.10^0$ | $43.37^0$ | $43.34^0$ | $49.48^0$ | $50.40^0$ |
| | 1000 | $48.0^0$ | $44.24^0$ | $44.50^0$ | $44.46^0$ | $52.11^0$ | $53.39^0$ |
| $43^0$ | 200 | $43.0^0$ | $38.22^0$ | $38.32^0$ | $38.30^0$ | $42.29^0$ | $42.45^0$ |
| | 500 | $43.0^0$ | $39.61^0$ | $39.71^0$ | $39.68^0$ | $45.48^0$ | $46.38^0$ |
| | 1000 | $43.0^0$ | $40.48^0$ | $40.64^0$ | $40.61^0$ | $47.67^0$ | $48.90^0$ |
| $38^0$ | 200 | $38.0^0$ | $34.63^0$ | $34.65^0$ | $34.64^0$ | $38.41^0$ | $38.62^0$ |
| | 500 | $38.0^0$ | $35.71^0$ | $35.81^0$ | $35.80^0$ | $41.04^0$ | $41.89^0$ |
| | 1000 | $38.0^0$ | $36.31^0$ | $36.50^0$ | $36.49^0$ | $42.79^0$ | $43.89^0$ |
| $33^0$ | 200 | $33.0^0$ | $30.75^0$ | $30.71^0$ | $30.72^0$ | $34.03^0$ | $34.25^0$ |
| | 500 | $33.0^0$ | $31.51^0$ | $31.56^0$ | $31.56^0$ | $36.22^0$ | $36.97^0$ |
| | 1000 | $33.0^0$ | $32.06^0$ | $32.09^0$ | $32.09^0$ | $37.55^0$ | $38.48^0$ |

The numerical results allow the conclusion to be drawn that a length to diameter ratio of 6, as in the case of the Cambridge self-boring pressuremeter, is insufficient to eliminate the finite length effects of the membrane on the values of the derived strength parameters. The finite length effects result in the deduction of non-conservative strength parameters.

### 6.5.4 Effects of friction angle

As was shown in Table 6.7, four different friction angles were chosen for each case with the same stiffness so that possible effects due to soil density could be quantified. In all numerical analyses presented in this section, the variation of friction angle was found to have little influence on the finite length effects, which can be seen clearly in Figure 41 to Figure 44. The finding is in agreement with Laier et al.(1975) who, based on large chamber test results, found that the effect on the pressuremeter limit pressure due to the

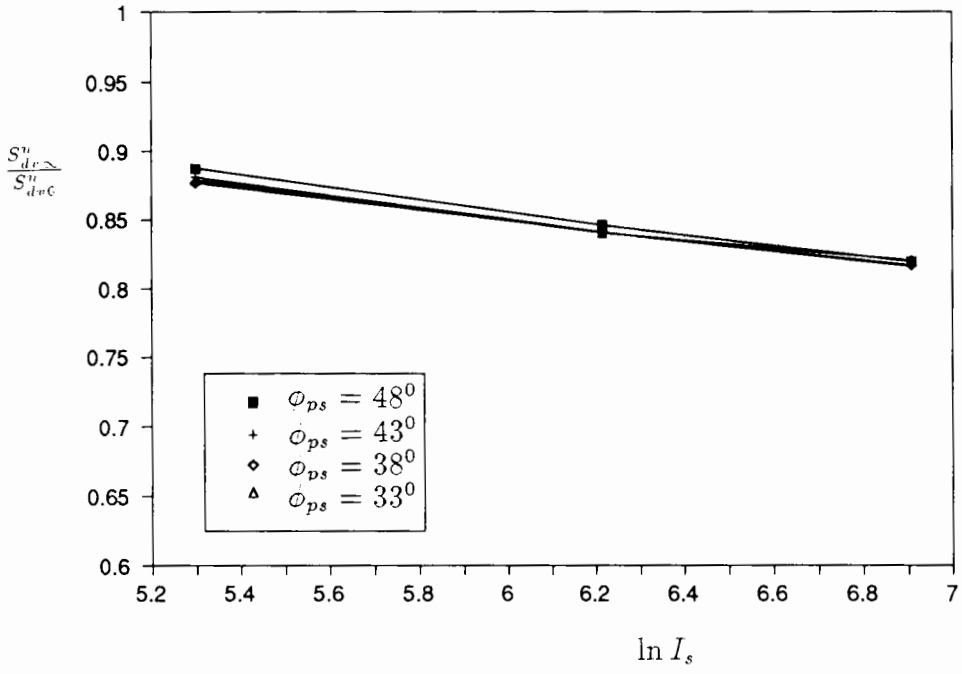


Figure 41: Variation of finite length effects on slope with stiffness index using volumetric strain

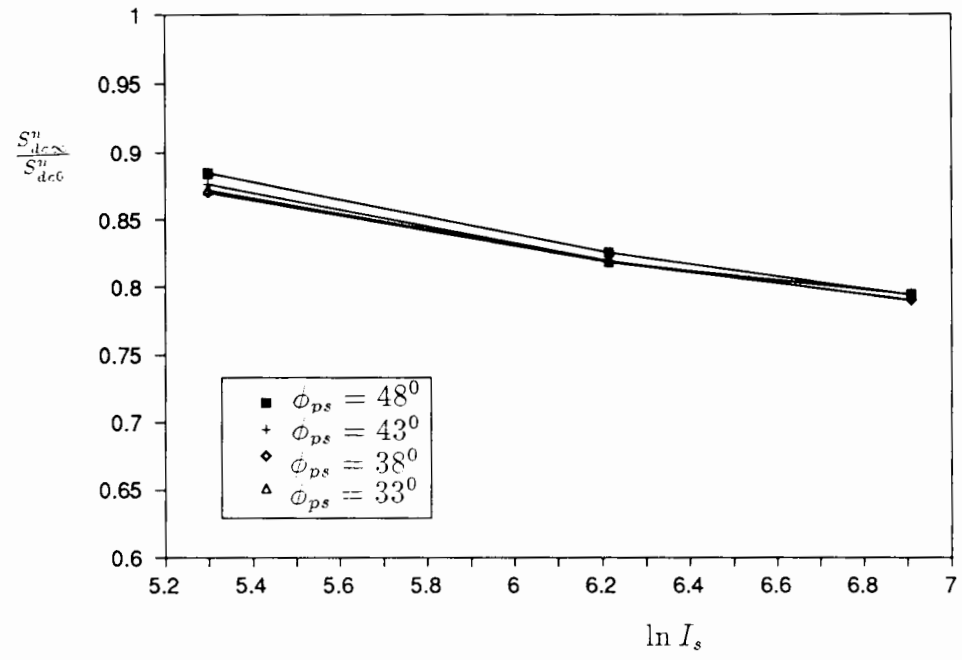


Figure 42: Variation of finite length effects on slope with stiffness index using central strain

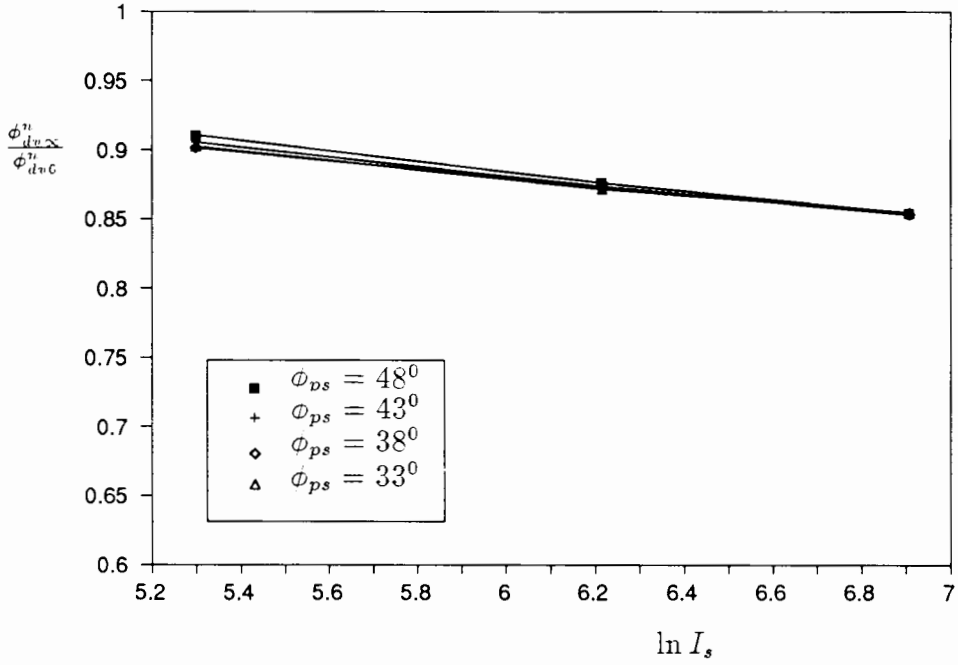


Figure 43: Variation of finite length effects on friction angle with stiffness index using volumetric strain

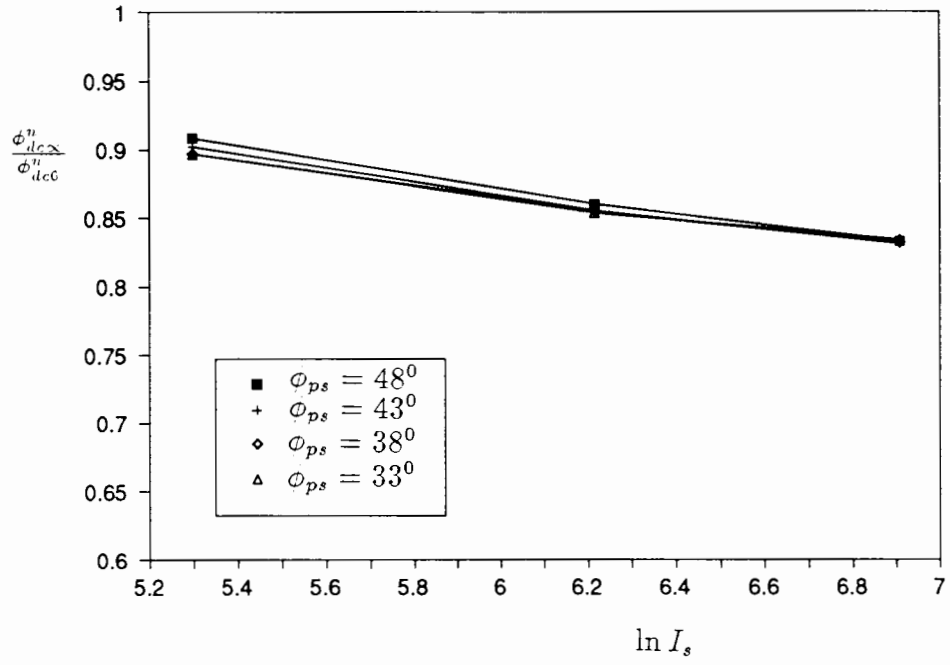


Figure 44: Variation of finite length effects on friction angle with stiffness index using central strain

finite length of probe is largely independent of the soil density. The important quantities which influence in-situ test results are discussed fully in the next section.

### 6.5.5 Effects of stiffness

The variation of the finite length effects on the derived strength parameters with soil stiffness index is shown in Figure 41 to Figure 44. Here the stiffness index was defined by the ratio of shear modulus to initial horizontal stress. As far as the friction angles are concerned, the effects of the stiffness index may be approximately expressed by

$$\frac{\phi^n_{dv\infty}}{\phi^n_{dv6}} = 1.076 - 0.0324 \ln I_s \tag{354}$$

for the case when the volumetric strain is used, and by

$$\frac{\phi^n_{dc\infty}}{\phi^n_{dc6}} = 1.129 - 0.043 \ln I_s \tag{355}$$

for the case when the central strain is used. $I_s$ denotes the stiffness index for sand.

The advantage of the numerical analysis is that both strength and stiffness of the soil can be investigated independently. As far as the finite length effect on the derived strength parameters is concerned, the numerical results suggest that the stiffness has a more important influence than that of the soil strength. The important effects of the stiffness on the results of in-situ tests have been discussed at length by Houlsby and Wroth (1989) based on the results from both laboratory and theoretical studies of various in-situ tests. The significant influence of the stiffness on the finite length effects for the self-boring pressuremeter tests provides more evidence to suggest that the stiffness is one of the most important quantities in the understanding of in-situ tests.

### 6.5.6 Effects of elastic deformation in plastic regions

In addition to the finite length effects, the elastic deformation in the plastic zones may have some effects on derived strength parameters based on Hughes et al's simplified analysis. The ratio of the derived parameters for the case when the exact cavity expansion solution is used to produce the expansion curve to those derived for the case when the

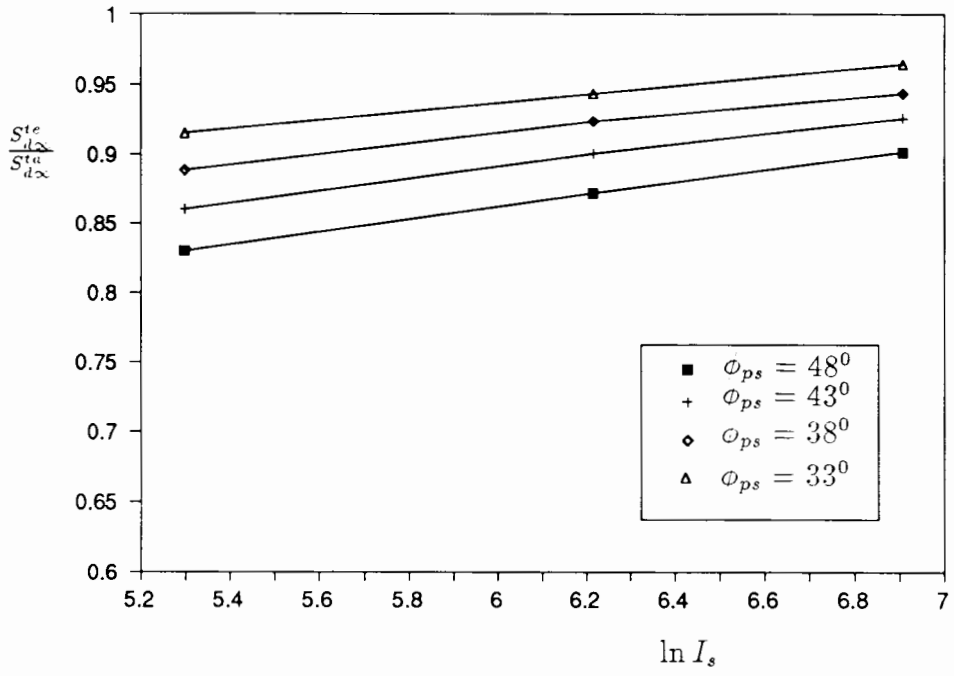


Figure 45: Variation of effects on slopes due to elastic deformation with stiffness index

Hughes et al's analysis is used may be used to assess the effects of the elastic deformations. The resulting ratios of cavity slopes and backcalculated friction angles are shown in Figure 45 and Figure 46 respectively. Both soil density and stiffness index are found to have significant influence on the effects of elastic deformation. It is important to note that the Hughes et al's simplified analysis tends to underestimate significantly the derived loading slopes and backcalculated strength parameters. As was expected, the effect of elastic deformation in the plastic zones is particularly marked for dense soil with low stiffness index.

## 6.6 Analysis of cone-pressuremeter tests in clay

### 6.6.1 Parameters for the analysis

The cone-pressuremeter is a new in-situ testing device which combines a $60^0$ electric piezocone with the pressuremeter test. The new test is intended to combine some of the merits of pressuremeter test with the operational convenience of the cone penetration test. By using the analysis published by Houlsby and Withers (1988), the cone-pressuremeter

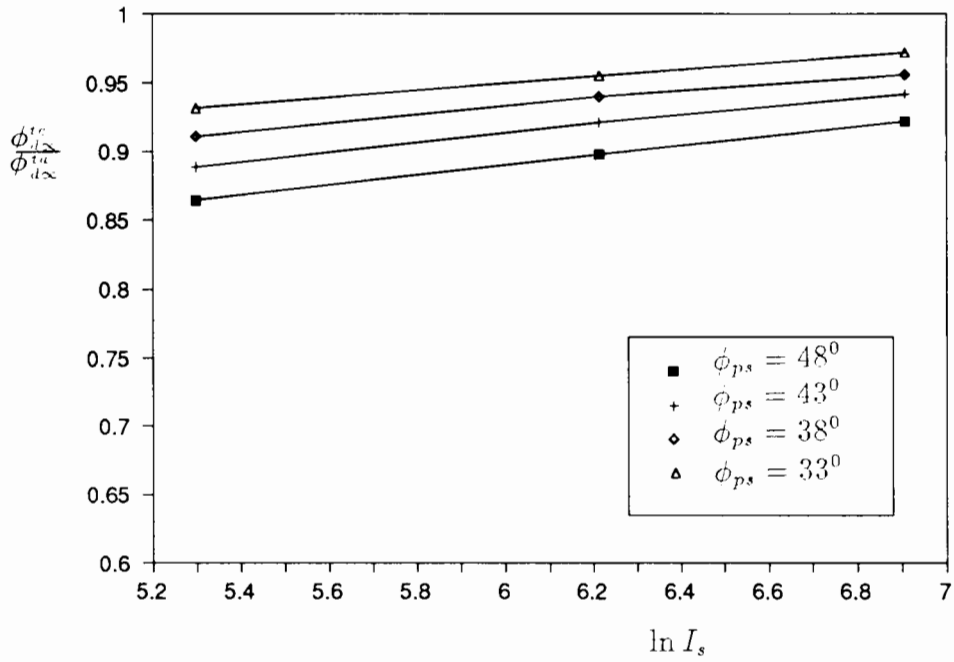


Figure 46: Variation of effects on friction angles due to elastic deformation with stiffness index

test allows the shear modulus and undrained strength to be determined. In the analysis, the initial installation of the full-displacement pressuremeter is modelled theoretically as the expansion of a cylindrical cavity expansion within the soil. The expansion phase of the pressuremeter test is modelled as a continued expansion of the same cylindrical cavity, and the contraction phase as a cylindrical cavity contraction. This modelling of expansion and contraction phases of the pressuremeter will be somewhat in error, as the pressuremeter has a finite length instead of an infinitely long length as assumed in the analysis. The error due to the finite length of pressuremeter membrane can be assessed by modelling the pressuremeter expansion and contraction phases using the finite element method.

In the numerical analyses, a length to diameter ratio of 10, which is the same as that used for the Fugro prototype device, was assumed. The large strain finite element formulation was adopted in order to be consistent with the Houlsby and Withers analysis.

Table 6.8 Numerical tests of cone-pressuremeter in clay

| $\frac{L}{D}$ \ $I_r$ | 200 | 300 | 500 | 800 |
|---|---|---|---|---|
| 10 | R8 | R4 | R6 | R2 |
| $\infty$ | R7 | R3 | R5 | R1 |

The parameters of four sets of numerical pressuremeter tests are shown in Table 6.8. The installation of the cone-pressuremeter is modelled by setting up initial stresses according to the large strain cavity expansion solution developed by Sagaseta (1984). The expansion phase of pressuremeter tests is carried out by further applying an uniform normal pressure incrementally along the membrane wall. The incremental nodal force induced by the applied normal surface pressure is calculated when the element geometry is updated. As the initial stresses represent the limit stress state of cavity expansion, it is necessary to use a very small increment of pressure for performing pressuremeter expansion in order to achieve a stable numerical solution. For the case of pressuremeter tests with an infinitely long membrane, it is not possible to perform pressuremeter expansion numerically by a pressure controlled analysis. Hence a displacement controlled analysis was used for modelling pressuremeter test with an infinitely long membrane.

### 6.6.2 Numerical results

Each set of numerical pressuremeter expansion tests with the same rigidity index was continued to the same maximum cavity strain before performing pressuremeter contraction tests so that possible effects due to the variation of the maximum strain were eliminated. Figure 47 shows a typical set of results of numerical simulations of the cone-pressuremeter test in clay. The Houlsby and Withers method is used to derive shear modulus, undrained strength and horizontal initial stresses. In order to do so, the pressuremeter expansion and contraction curve has to be plotted as pressure $\psi$ against $-\ln(\epsilon_{cm} - \epsilon_c)$. In this section, the results derived from the plot using cavity strain at the middle point of membrane are presented. The derived initial stress, stiffness and undrained shear strength are

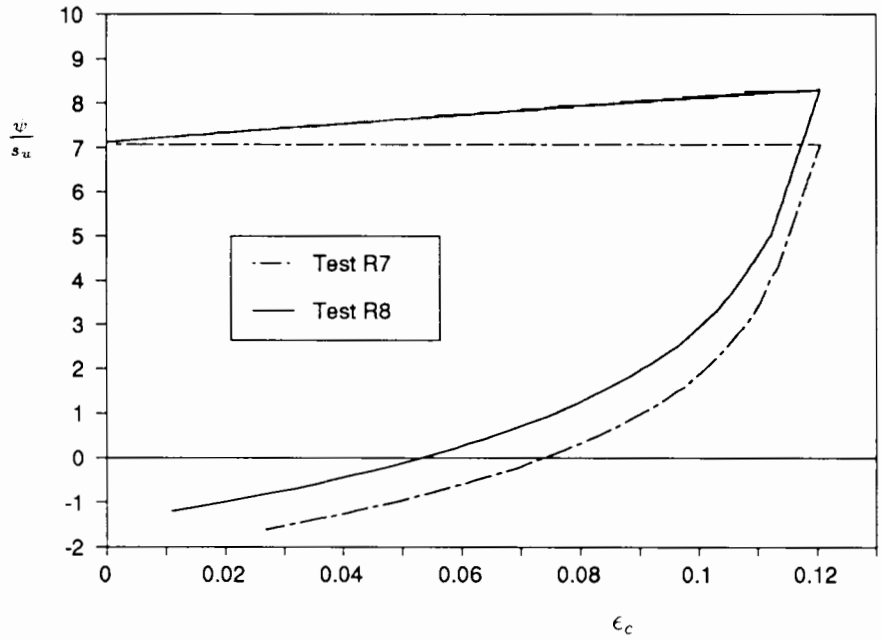


Figure 47: A typical set of results for numerical simulations of the cone-pressuremeter test in clay

shown in Table 6.9. The triaxial undrained strength $s_{utc}$ is assumed to be unity in the analysis and it corresponds to a plane strain undrained strength of $\frac{2}{\sqrt{3}}$. It is found that for the cone-pressuremeter test with an infinitely long probe the derived undrained plane strain shear strengths for all cases are in good agreement with the actual values used in the calculations with a maximum error of less than 1%. This indicates that the quality of the numerical method adopted in the analysis is very high.

Table 6.9 Summary of derived parameters for cone-pressuremeter test in clay

| $\frac{L}{D}$ | 10 | | | $\infty$ | | |
|---|---|---|---|---|---|---|
| $I_r$ | G | $s_u$ | $\sigma_{h0}$ | G | $s_u$ | $\sigma_{h0}$ |
| 200 | 187.14 | 1.2377 | 1.016 | 209.39 | 1.1644 | 0.0 |
| 300 | 272.91 | 1.2450 | 1.051 | 312.56 | 1.1556 | 0.0 |
| 500 | 446.60 | 1.2725 | 1.085 | 535.60 | 1.1623 | 0.0 |
| 800 | 684.91 | 1.3025 | 1.119 | 855.80 | 1.1599 | 0.0 |

The ratio between the derived parameters from pressuremeter tests with a finite length

of probe and the derived parameters from pressuremeter tests with an infinitely long probe may largely represent the effects of finite length of pressuremeter membrane. It was found that the application of the Houlsby and Withers method in deriving soil parameters for real cone-pressuremeter tests tends to overestimate the shear strength $s_u$ and initial stresses $\sigma_{h0}$ and underestimate the shear modulus $G$. As was expected, the overestimation of shear strength is relatively small due to the large length to diameter ratio used in the cone-pressuremeter. For clays where the rigidity index is under 600, the overestimation of the shear strength is under 10%. The underestimation of the shear modulus, however, could be up to 20%. In agreement with Houlsby and Withers (1988), it was found that the estimation of initial horizontal stress is so significantly affected by the pressuremeter geometry that the direct use of the cavity expansion theory may not be able to give any sensible results.

### 6.6.3 Effects of rigidity index

Figure 48 and Figure 49 show the variation of finite length effects on derived soil strength and stiffness with rigidity index. It was observed that the overestimation of shear strength and the underestimation of shear modulus increases with rigidity index. This variation may be expressed by the following expression

$$\frac{s_u^{\infty}}{s_u^{10}} = 1.131 - 0.0355 \ln I_r \tag{356}$$

for shear strength and

$$\frac{G^{\infty}}{G^{10}} = 0.606 - 0.0958 \ln I_r \tag{357}$$

for shear modulus.

### 6.6.4 Effects on initial stresses

The horizontal stresses derived from Houlsby and Withers method are known to be too high if cylindrical cavity expansion is used (Houlsby and Withers, 1988; Powell, 1990). The numerical analyses presented in this section highlight the significant effects due to

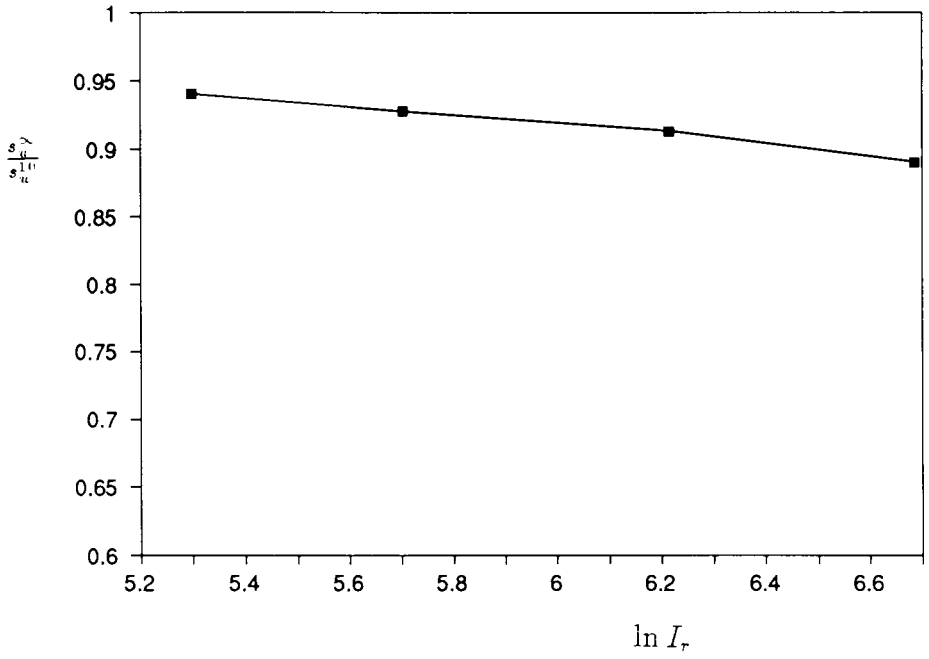


Figure 48: Variation of effects on undrained strength due to finite length with rigidity index

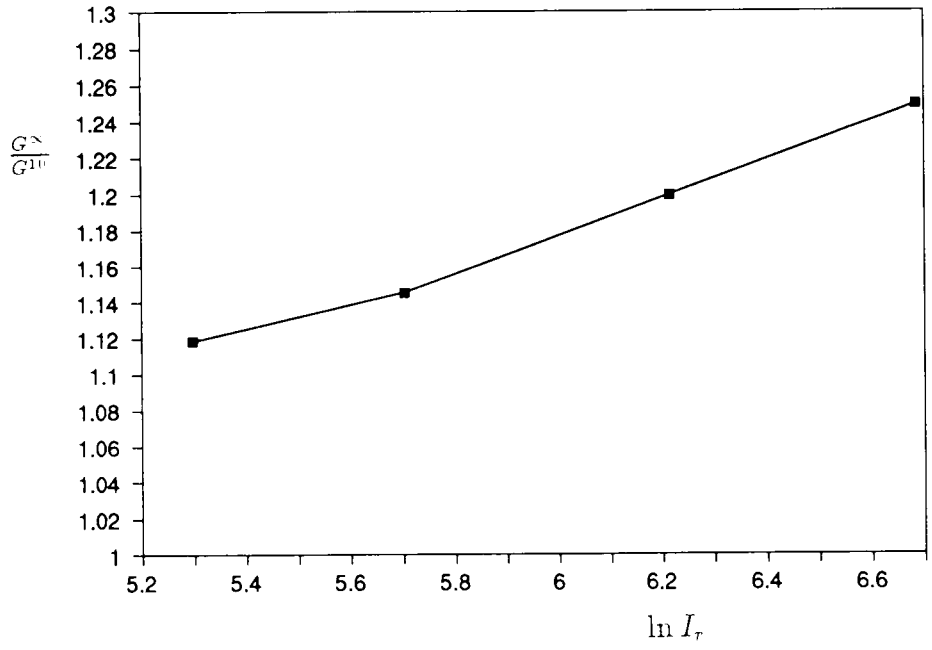


Figure 49: Variation of effects on stiffness due to finite length with rigidity index

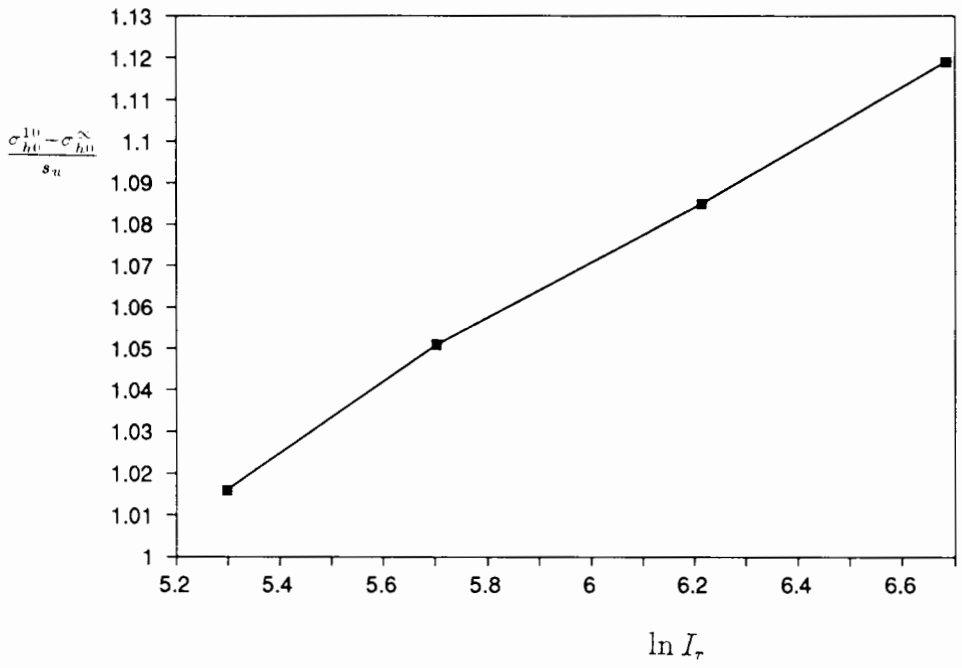


Figure 50: Variation of effects on initial stress due to finite length with rigidity index

finite length of pressuremeters. The use of Houlsby and Withers method for the cone-pressuremeter tests in field conditions tends to overestimate the initial horizontal stress significantly. In order to quantify this effect, the variable defined as $\frac{\sigma_{h0}^{10}-\sigma_{h0}^{\infty}}{s_u}$ was plotted against input soil rigidity index $I_r$ in Figure 50, where $\sigma_{h0}^{10}$ denotes the derived initial horizontal stress for the cone pressuremeter tests with a length to diameter ratio of 10 and $\sigma_{h0}^{\infty}$ represents the derived initial horizontal stress for the cone pressuremeter test with an infinitely long probe. The variation of $\frac{\sigma_{h0}^{10}-\sigma_{h0}^{\infty}}{s_u}$ with the rigidity index may be approximately expressed by the following equation:

$$\frac{\sigma_{h0}^{10} - \sigma_{h0}^{\infty}}{s_u} = 0.630 - 0.0733 \ln I_r \tag{358}$$

Equation ( 358) may be used to provide a better estimation of the initial horizontal stress from the cone-pressuremeter test results.

It is clear to see from Figure 50 that the overestimation of the initial horizontal stress due to the finite length varies from $1.02 s_u$ to $1.12 s_u$ when the soil rigidity index increases from 200 to 800. Houlsby and Withers (1988) found that using $\sigma_{h0}$ estimated from cylindrical cavity expansion theory and $\sigma_{v0}$ from the bulk unit weight of the soil could

sometimes result in a $(\sigma_{h0} - \sigma_{v0})$ value which significantly exceeds $2s_u$. It is impossible for a Tresca material to have a maximum shear stress of more than a $s_u$. This may largely be due to the significant overestimation of $\sigma_{h0}$ with a magnitude of more than $s_u$ because of ignoring finite length effects in the analysis.

## 6.7 Recommended interpretation procedure for pressuremeter tests in clay and sand

### 6.7.1 Self-boring pressuremeter tests in clay

The analysis presented in Section 6.4 has illustrated the danger of applying an undrained shear strength profile obtained from self-boring pressuremeter tests using the conventional Gibson and Anderson method. By using the numerical results, a correction may be made to the pressuremeter test results to account for the finite length effects.

A value of 6 for length to diameter ratio may be used to represent the geometry of the self-boring pressuremeter which has been widely used in practice (e.g. the Cambridge self-boring pressuremeter). Hence only numerical results for the pressuremeter tests with a length to diameter ratio of 6 are considered in the following discussion. Of course, the same argument may be used for self-boring pressuremeter tests with a different length to diameter ratio.

For self-boring pressuremeter tests in clay, the effects on derived undrained shear strength due to the finite length of the probe depends on the approach used to derive the undrained shear strength. As was mentioned earlier, when the undrained shear strength is estimated from the limit pressure, the finite length effect is relatively independent of the rigidity index and the average overestimation of the undrained shear strength was found to be about 15%. This suggests that when the undrained shear strength is obtained from the limit pressure approach, the finite length effects may be accounted for by multiplying the derived strength by a factor of 0.85.

On the other hand, if the undrained shear strength is estimated from the pressuremeter expansion slope, it is necessary to distinguish the two different strain definitions used in

presenting the pressuremeter expansion curve. When the undrained shear strength is obtained from the plot of pressure against the volumetric strain, the following expression may be used to represent the finite length effects on the derived strength:

$$\frac{s_{uv}^{\infty}}{s_{uv}^{6}} = 0.971 - 0.0185 \ln I_r \qquad (359)$$

If the undrained shear strength is estimated from the plot of pressure against the membrane central strain, the finite length effect was found to be slightly dependent on the strain ranges used in the interpretation. In general, the use of the membrane central strain could lead to a slightly more overestimation of the undrained strength due to finite length of pressuremeters.

Equation ( 359) may be used to improve the conventional Gibson and Anderson method in deriving the undrained shear strength from the pressuremeter test results.

With respect to the shear modulus, it was found that the effect on shear modulus due to finite length is negligible when the shear modulus is derived from the initial curve in the plot of pressure against membrane central strain. However, if the plot of pressure against volumetric strain is used to estimate the shear modulus, the finite length effect was found to be quite significant. The overestimation of the shear modulus due to the finite length may go up to 13%. It suggests that the derived shear modulus from the plot of pressure against volumetric strain for the pressuremeter test results needs to be multiplied by 0.87 in order to eliminate the effect due to pressuremeter geometry.

### 6.7.2 Self-boring pressuremeter tests in sand

The effects on derived soil friction angle and dilation angles due to the finite length of pressuremeter have been studied in Section 6.5. It was found that the use of the conventional Hughes et al analysis tends to overestimate friction angles. Based on the results using the strain range of between 1 — 5% to derive loading slope $S_d$, it may be concluded that such overestimation of friction angles is, however, largely independent of the friction angle.

However, the finite length effect on derived friction angles was found to be significantly

dependent on the soil stiffness index $I_s$. This dependence may be expressed approximately by the following expression:

$$\frac{\phi^n_{dc\infty}}{\phi^n_{dc6}} = 1.129 - 0.0432 \ln I_s \qquad (360)$$

for the case when the soil parameters are derived from pressuremeter test results plotted as pressure against central membrane strain.

The soil parameters can also be derived from the pressuremeter results plotted as pressure against volumetric strain. As this latter approach tends to overestimate the shear modulus $G$ very significantly, the former approach using central membrane strain is recommended. After obtaining the shear modulus and the initial horizontal stress using the conventional method, a better estimation of friction angle which takes into account the finite length effects may be provided by using equation ( 360). After the improved friction angle is obtained, a better estimation of dilation angle may be estimated by using the critical friction angle and Rowe's stress-dilatancy equation.

Another important effect produced by ignoring the elastic deformation in the plastic zone in the Hughes et al analysis may be taken into account by using the numerical results presented in Figure 45 and Figure 46. It can be seen that the Hughes et al simplified analysis tends to underestimate derived friction angles. As was expected, the underestimation is particularly marked in the soil with low elastic stiffness and high friction angle.

The combined effects of the finite length of the pressuremeter and ignoring the elastic deformation in the plastic zone may be assessed by comparing the actual friction angles $\phi^{in}_{ps}$ used in the analysis and backcalculated friction angles for field pressuremeter tests. Figure 51 shows the variation of the combined effects on the derived friction angle with the stiffness index. It was observed that the combined effects depend on both friction angle and stiffness index since the effects due to the ignoring the elastic deformation in the plastic zone are strongly dependent on friction angle.

The most interesting thing is that the combined effects of the finite length of pressuremeters and ignoring the elastic deformation in the analysis can be easily taken into account in the interpretation by presenting the data in Figure 51 in a plot of the combined

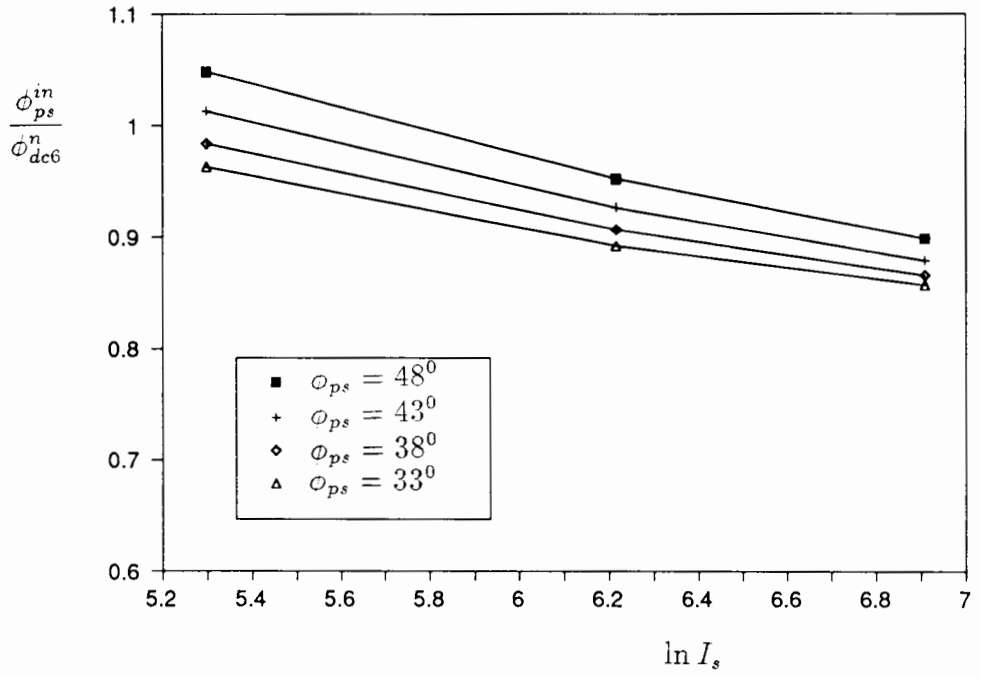


Figure 51: The combined effects on friction angles due to finite length and elastic deformation

effects against $I_s \frac{1-\sin\phi_{ps}^{in}}{\sin\phi_{ps}^{in}}$. The advantage of adopting the modified plot to present the numerical results is that all numerical data lies on a unified line as shown in Figure 52. The theoretical rationale of using this modified plot is that the analytical solution for both cylindrical and spherical cavity expansion in sand presented in Chapter 2 suggests the important effect of the parameter $I_s \frac{1-\sin\phi_{ps}^{in}}{\sin\phi_{ps}^{in}}$ on the cavity pressure-displacement relationship. We may therefore expect that the relationship between the pressuremeter pressure and cavity strain for the case when $\frac{L}{D}$ is between two extreme limits of cylindrical cavity and spherical cavity may also be related to the strength and stiffness of the soil in a similar manner.

Using linear regression, the following simple expression:

$$\frac{\phi_{ps}^{in}}{\phi_{dc6}^{n}} = 1.360 - 0.0775 \ln\left(\frac{1-\sin\phi_{ps}^{in}}{\sin\phi_{ps}^{in}} I_s\right) \tag{361}$$

in which $I_s = \frac{G}{\sigma_{h0}}$, may be used to represent the combined effects of pressuremeter geometry and ignoring elastic deformation in the analysis. The above equation can be used to

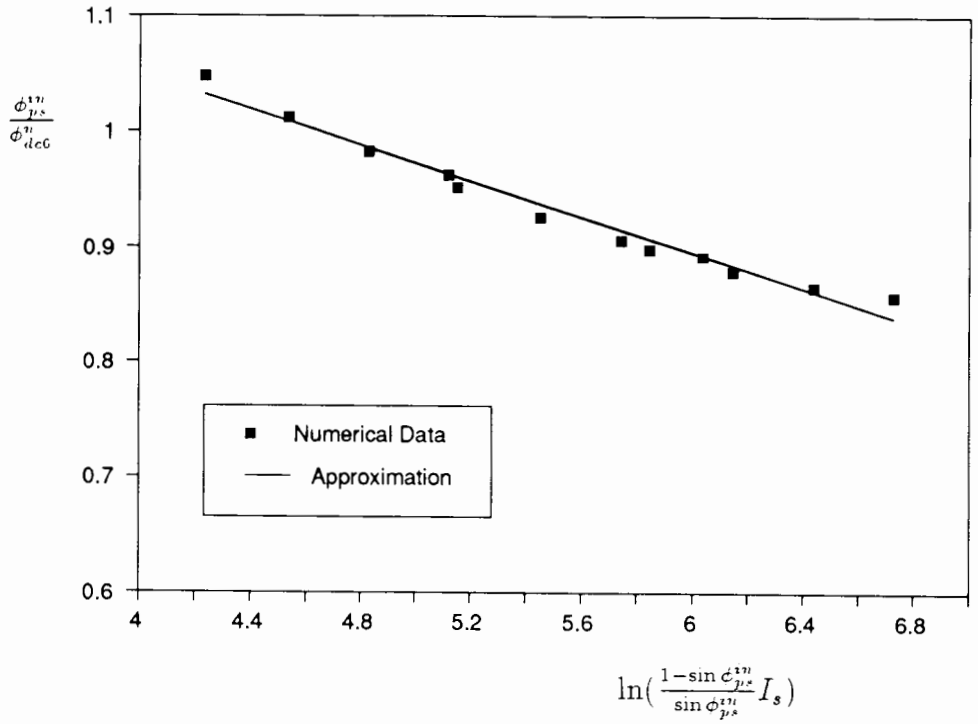


Figure 52: The combined effects on friction angles due to finite length and elastic deformation in a generalised plot

obtain a better estimation of friction angles denoted by $\phi^{in}_{ps}$ after the value of $\phi^{n}_{dc6}$ is estimated using the simplified Hughes et al method from the field self-boring pressuremeter tests.

### 6.7.3 Cone-pressuremeter tests in clay

The numerical results for the cone pressuremeter tests with length to diameter ratios of 10 presented in Section 6.6 suggest that the effect due to the finite length of the probe on undrained shear strength when using the Houlsby and Withers analysis is relatively small. The overestimation of the undrained shear strength is typically under 10% for a soil with a rigidity index less than 800. It is mainly because of large length to diameter ratio of the cone-pressuremeter. The variation of the finite length effects on strength with rigidity index may be expressed by the following equation:

$$\frac{s_u^{\infty}}{s_u^{10}} = 1.131 - 0.0355 \ln I_r$$

for the case when the central membrane strain is used to plot the pressuremeter test results.

However it was found that use of the Houlsby and Withers analysis in deriving shear modulus $G$ from the field pressuremeter test tends to underestimate the true value significantly. For the soil with $I_r = 600$, the shear modulus could be underestimated by 20%. Based on the numerical results, the following equation may be used to represent the variation of finite length effects on shear modulus with soil rigidity index.

$$\frac{G^{\infty}}{G^{10}} = 0.606 - 0.0958 \ln I_r$$

The numerical analyses suggest that the failure of the Houlsby and Withers method in deriving realistic initial horizontal stress may largely be blamed on effect of the finite length of pressuremeter probe. Based on the numerical results, an alternative way of estimating initial horizontal stress from field cone-pressuremeter tests may be made by using the following equation:

$$\frac{\sigma_{h0}^{10} - \sigma_{h0}^{\infty}}{s_u} = 0.630 + 0.0733 \ln I_r$$

In order to highlight the relevance of the numerical analyses, the field cone-pressuremeter test results reported by Houlsby and Withers (1988) are re-interpreted here for comparison. Emphasis has been placed on the prediction of the initial total horizontal stress $\sigma_{h0}$ because the numerical analysis suggests a considerable influence from the finite length of the pressuremeter on this particular quantity.

A total of seven tests at Madingley, Cambridge were made with the Fugro cone-pressuremeter ($\frac{L}{D} = 10$). A number of self-boring pressuremeter tests were also carried out at the same site by Clarke (1979). The cone-pressuremeter tests were interpreted by the original Houlsby and Withers method with use of cylindrical cavity case and the deduced total horizontal stress values are shown in Figure 53. Also included in Figure 53 is the total horizontal stress obtained from the self-boring pressuremeter test data. It can be seen that $\sigma_{h0}$ values predicted from the cone-pressuremeter test using the Holusby and Withers analysis are consistently higher than the self-boring pressuremeter test results, sometimes by a factor of 2. A similar finding was also reported by Powell (1990).

The cone-pressuremeter test data have been re-interpreted using the following alternative procedure, which accounts for the effect of the finite length of the pressuremeter

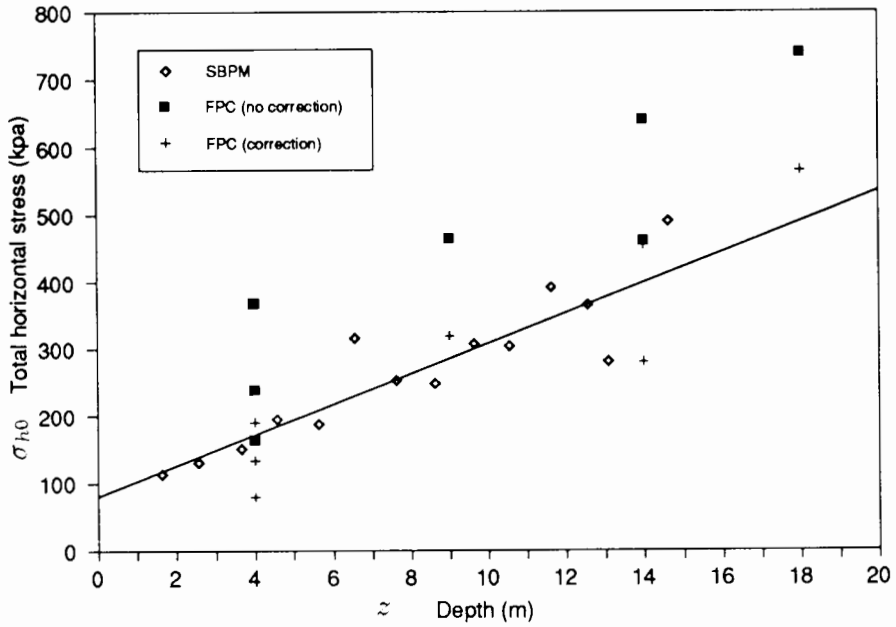


Figure 53: Comparsion of the horizontal stress measured by the self-boring pressuremeter and the cone-pressuremeter tests at Madingley, Cambridge

on the derived parameters. First of all, the Houlsby and Withers method is used to give an estimation of the undrained shear strength, shear modulus, rigidity index and total horizontal stress, which are denoted by $s_u^{10}, G^{10}, I_r^{10}$ and $\sigma_{h0}^{10}$ respectively, from the cone-pressuremeter test results. Secondly, equations ( 356) and ( 357) are used in an iterative manner to furnish a better estimation of $s_u, G$ and $I_r$. Finally, with the improved estimation of the rigidity index $I_r$, equation( 358) can be used to give a corrected estimation of the total horizontal stress $\sigma_{h0}$.

The derived values of $\sigma_{h0}$ using the alternative procedure are also presented in Figure 53. This shows that the total horizontal stress values interpreted in this way are in good agreement with the average trend predicted by the self-boring pressuremeter test. The remaining scatter for the shallow depth cone-pressuremeter test is possibly due to free surface effects.

## 6.8 Conclusion

One of the major advantages of the pressuremeter test is the possibility of evaluating fundamental soil parameters from the test data. In the past a simplified one-dimensional cavity expansion theory has been used to reduce the pressuremeter test data to give design parameters. The cavity expansion theory involves important assumptions about the material behaviour and pressuremeter geometry. In this chapter, the two-dimensional finite element formulation was used to assess the effects of using these simple assumptions on derived soil parameters.

For the self-boring pressuremeter tests in clay, it was found that use of the conventional Gibson and Anderson method for the field pressuremeter test tends to overestimate the undrained shear strength and shear modulus. It is interesting to note that the overestimation of the shear modulus, when derived from the plot of the pressure against central membrane strain, is negligible. As far as the shear strength is concerned, the numerical results suggest strong dependence of the finite length effects on rigidity index when the undrained shear strength is derived from the loading slope. By contrast, when using the limit pressure to obtain the undrained shear strength, the finite length effects have been found to be relatively independent of the rigidity index of the soil.

It has also been demonstrated that serious overestimation of the strength parameters of sands may be deduced by applying the Hughes et al method to field pressuremeter tests. The important role of the elastic deformation in the plastic zone was stressed with respect to derived soil parameters in the pressuremeter test.

As was expected, the numerical results show that the use of the cone-pressuremeter test with a length to diameter ratio of 10 may result in smaller effects due to the pressuremeter geometry. The use of the Houlsby and Withers method in deriving shear modulus, however, tends to underestimate the true value very significantly. The failure of obtaining the realistic initial stress using cylindrical cavity expansion theory may largely be explained by significant effects of the finite length of pressuremeters.

Based on numerical results, improved procedures for obtaining soil parameters from pressuremeter tests in both clay and sand have been proposed in order to eliminate effects

of using the simple assumptions in the conventional interpretation methods.

# Chapter 7

# Conclusion

## 7.1 Summary and remarks

The work described in this thesis had three objectives. Firstly, to develop analytical solutions for large strain cavity expansion and contraction in dilatant materials; Secondly, to develop a rational finite element formulation suited for axisymmetric elastic-plastic problems and thirdly, to quantify effects of real pressuremeter geometry on derived soil properties. These three aspects of the work are summarized in the following sections along with closing comments and recommendations for future work.

### 7.1.1 Analytical study of cavity expansion problems

An important aspect of the research presented in this thesis has been the development of closed form solutions for large strain cavity expansion and contraction in dilatant soils. A unified analytical solution is presented in Chapter 2 for the expansion of both cylindrical and spherical cavities in dilatant elastic-plastic materials, using the Mohr-Coulomb yield criterion with a non-associated flow rule. An explicit expression for the pressure-expansion relation can be found without any restriction being imposed on the magnitude of the deformations. Consequently, the limit pressure when the radius of the cavity approaches infinity can be determined analytically with no additional assumption being made about the deformation mode. Closed form solutions for residual stress and

displacement distributions are obtained at any stage of the unloading process.

### 7.1.2 Finite element analysis of axisymmetric constrained solids

In recent years, the finite element method was not only applied to the calculation of deformations but was also employed for the prediction of collapse loads. This is mainly due to the fact that the need for accurately determining limit load arises frequently, especially when exact limit solutions cannot be derived, or sophisticated plasticity models are employed for which the bounding theorems no longer hold. Unfortunately, it is found that most published work on finite element computations has failed to compare numerical and theoretical limit solutions. In general, the numerical analysis tends to overestimate the theoretical collapse load. The problem is normally believed to relate to the ability of the displacement based finite element in modelling an incompressible deformation mode. Although several approaches have been proposed to deal with this difficulty, none of these have been found to be wholly satisfactory. After a detailed theoretical study of the influence of the displacement interpolation function on the excessive kinematic constraints imposed by the incompressibility condition, a novel displacement interpolation function, which is well suited for both one-dimensional and two-dimensional axisymmetric elastic-plastic problems, has been used to develop a new large strain finite element for the analysis of this type of problem.

### 7.1.3 Interpretation of pressuremeter tests

The advantage of the pressuremeter test over other in-situ tests is the ability of deriving accurate soil parameters from the test data. This has been achieved conventionally by using the simplified one dimensional cavity expansion theory. The cavity expansion theory, however, involves important assumptions about the material behaviour and boundary condition. The effects of using these simplifying assumptions are studied in Chapter 6 in detail. It appears from the numerical results obtained from an axisymmetric finite element analysis that a significant error may be introduced into the soil parameters deduced from the pressuremeter data as a consequence of the use of an over-simplified

interpretation method.

For self-boring pressuremeter tests in clay, it was found that use of the conventional Gibson and Anderson method for the field pressuremeter test tends to overestimate the undrained shear strength of clay because of the finite length of the pressuremeter. The numerical results suggest that the overestimation of shear strength due to a finite length to diameter ratio is largely dependent on rigidity index when the undrained shear strength is derived from the loading slope. The effects of finite length on derived shear modulus may be negligible when the pressuremeter test results are plotted as pressure against strain at the middle point of the membrane. Based on the numerical results, an alternative procedure for interpreting pressuremeter tests in clays has been developed so that the possible effects due to finite length of the pressuremeter may be taken into account.

A similar study of drained pressuremeter tests in sand has identified two possible sources of error in deriving the soil properties when the conventional Hughes et al method is applied. First of all, it has been shown that the friction angle of the soil tends to be underestimated significantly by the Hughes et al. method because the analysis assumed that elastic strain in the plastic zone around the membrane is negligible. The effects of elastic deformation in the plastic zone have been assessed by comparing the exact small strain cavity expansion solution (see, for example, Carter et al. 1986) with the Hughes et al's simplified small strain solution. Secondly, the results of numerical simulation of a pressuremeter test with a finite length have shown that the strength parameters of soils may be overestimated because of finite length of the pressuremeter. This inaccuracy is particularly marked in tests performed in the soil with a high stiffness index. An improved interpretation procedure, which is based on the numerical results, has been developed to overcome some of the errors introduced by the conventional Hughes simplified analysis.

As was expected, the numerical results show that the use of cone-pressuremeter test with a length to diameter ratio of 10 may result in a lower effect on shear strength due to the pressuremeter geometry. The Houlsby and Withers method, however, tends to underestimate the shear modulus significantly. The finite element parametric study indicates that the initial horizontal stress could be overestimated by approximately the magnitude of the undrained shear strength when the Houlsby and Withers analysis is

applied. These effects may be eliminated using the results of numerical simulation of the cone-pressuremeter test.

## 7.2 Future work

This thesis has dealt with the application of cavity expansion theory to the analysis of pressuremeters. As described above, the numerical parametric studies include the self-boring pressuremeter test in both clay and sand and the cone-pressuremeter test in clay. It would appear that further analysis of the cone-pressuremeter test in sand is required. In the analysis presented in the thesis, a number of simplifying assumptions have been made in order to avoid unnecessary complications in the formulation. One of the most important assumptions made was in the choice of stress-strain relationship in which both clay and sand were modelled by an elastic-perfectly plastic theory. In the development of the closed form solution for the cavity expansion problem, the soil was assumed to behave according to the non-associated Mohr-Coulomb model. It is the author's belief that it might be too complicated, if not impossible, to develop the analytical solution for the cavity expansion problem using a more sophisticated material model. As far as the numerical analysis is concerned, the von Mises criterion and the Matsuoka model were used to represent the clay and sand behaviour respectively. These assumptions about the soil behaviour are obviously not completely realistic. In particular, the possible effect of partial drainage for the pressuremeter test in clay and the effect due to different soil behaviour during loading and unloading for the pressuremeter test in sand should be taken into account in any future studies. The analysis would also benefit if additional features of real soil behaviour such as strain hardening of a clay and dependence of strength parameters with shear strain and effective stress level of a sand could be included in soil models.

Alternatively, future research could also be directed towards applications of cavity expansion theory to other geotechnical problems. These include, for example, the design of driven piles and the theoretical interpretation of the cone penetration test.

A rational interpretation method for the cone penetration test in clay has been recently

developed by Teh (1988), in which the stresses evaluated by the Strain Path Method are used as the starting condition for the finite element analysis. This was believed to give the most realistic solution of the cone penetration problem because both the steady state and equilibrium conditions are approximately satisfied. It is interesting to note that Norbury and Wheeler (1987) showed that the stresses around a slender body can be approximated closely by cylindrical expansion theory. This prediction has been also reproduced quite satisfactorily by the Strain Path Method for a penetrometer with a very sharp conical tip. It would be therefore very interesting to know if the alternative approach, which uses the stresses obtained from cavity expansion theory as the starting condition for the finite element analysis of the cone penetration test, can give a reasonable prediction of cone factors with reference to the approach developed by Teh. If the comparison is encouraging, a relatively simple and yet rational interpretation method for the cone penetration test in both clay and sand may be obtained without using the sophisticated Strain Path Method.

# Bibliography


[1] F. Baguelin, J.F. Jezequel, H. Le Mee, and A. Le Mehaute. Expansion of cylindrical probes in cohesive soils. *J. Soil Mech. Found. Div., ASCE*, 98:1129–1142, 1972.

[2] F. Baguelin, J.F. Jezequel, and D.H. Shields. *The pressuremeter and foundation engineering.* Trans. Tech. Publication, Clausthal, Germany, 1978.

[3] M.M. Baligh. Strain path method. *J. Geo. Eng. Div. ASCE*, 111:1108–1136, 1985.

[4] D. Bigoni and F. Laudiero. The quasi-static finite cavity expansion in a non-standard elasto-plastic medium. *Int. J. Mech. Sci.*, 31:825–838, 1989.

[5] R.F. Bishop, R. Hill, and N.F. Mott. Theory of indentation and hardness tests. *Proc. Phys. Soc.*, 57:147, 1945.

[6] M.D. Bolton. The strength and dilatancy of sands. *Geotechnique*, 36(1):65–78, 1986.

[7] M.D. Bolton. Discussion on "the strength and dilatancy of sands". *Geotechnique*, 37(2):219–226, 1987.

[8] D. Bruzzi, V. Ghionna, M. Jamiolkowski, R. Lancellotta, and G. Manferedini. Self-boring pressuremeter tests in Po River. *Proc. 2nd Symposium of the Pressuremeter and its Marine Applications*, pages 57–74, 1986.

[9] H.J. Burd. *A large displacement finite element analysis of a reinforced unpaved road.* DPhil thesis, Oxford University, England, 1986.

[10] H.J. Burd and G.T. Houlsby. Finite element analysis of two cylindrical expansion problems involving near incompressible material behaviour. *In. J. Num. Analy. Meth. Geomech.*, 1990 (In press).

[11] J.P. Carter, J.R. Booker, and E.H. Davis. Finite deformation of an elasto-plastic soil. *Int. J. Num. Analy. Meth. Geomech.*, 1:25–43, 1977.

[12] J.P. Carter, J.R. Booker, and S.K. Yeung. Cavity expansion in cohesive frictional soils. *Geotechnique*, 36(3):349–358, 1986.

[13] J.P. Carter and S.K. Yeung. Analysis of cylindrical cavity expansion in a strain weakening material. *Comput. Geotech.*, 1:161–180, 1985.

[14] P. Chadwick. The quasi-static expansion of a spherical cavity in metals and ideal soils. *Q. J. Mech. Appl.. Math.*, 12:52–71, 1959.

[15] W.F. Chen. *Limit analysis and soil plasticity.* Elsevier, Amsterdam, 1975.

[16] B.G. Clarke. Results of self-boring pressuremeter tests. *PMIT Report T7/R1, Cambridge University Engineering Department*, 1979.

[17] E.H. Davis. Theories of plasticity and the failure of soil masses. *In: Soil mechanics (ed. I.K. Lee), London:Butterworths*, 1969.

[18] E.H. Davis, G.J. Ring, and J.R. Booker. The significance of the rate of plastic work in elasto-plastic analysis. *Proc. Int. Conf. Finite Element Methods in Engg., Sydney*, pages 327–337, 1974.

[19] R. de.Borst and P.A. Vermeer. Possibilities and limitations of finite elements for limit analysis. *Geotechnique*, 34(2):199–210, 1984.

[20] J.K. Dienes. On the analysis of rotation and stress rate in deforming bodies. *Acta Mechanica*, 32:217–232, 1979.

[21] W.P. Doherty, E.L. Wilson, and R.L. Taylor. Stress analysis of axisymmetric solids utilizing higher order quadrilateral finite elements. SERM Report No. 69-3. University of California.

[22] W.J. Eden and K.T. Law. Comparison of undrained shear strength results obtained by different test methods in soft clays. *Canadian Geotech. J.*, 17:369–381, 1980.

[23] M. Fahey. *A study of the pressuremeter test in dense sand.* PhD thesis, Cambridge University, England, 1980.

[24] M. Fahey and J.P. Carter. Some effects of rate of loading and drainage on pressuremeter tests in clay. *Proc. Special Geomechanics Symp. on Interpretation of Field Testing for Design Parameters, Adelaide, Institution of* engineers, *Australia*, pages 50–55, 1986.

[25] B. Fraeijs de Veubeke. Displacement and equilibrium method in the finite element method. In O.C. Zienkiewicz and G.S. Holister, editors, *Stress analysis*, London, 1965. John wiley.

[26] H. Fukagawa, H. Ohta, A. Iizuka, A. Nishihara, and Y. Morita. Effects of drainage on interpretation of pressuremeter tests in clay. *Proc. 3rd Int. Symp. on Pressuremeters, ISP3, Oxford*, pages 189–198, 1990.

[27] V. Ghionna, M. Jamiolkowski, R. Lancellotta, M.L. Tordella, and C.C. Ladd. Performance of self-boring pressuremeter tests in cohesive deposits. *MIT report, Cambridge, Mass.*, 1981.

[28] R.E. Gibson and W.F. Anderson. In-situ measurement of soil properties with the pressuremeter. *Civ. Engng. Publi. Wks. Rev.*, 56:615–618, 1961.

[29] L.R. Herrmann. Elasticity equations for incompressible and near incompressible materials by a variational theorem. *AIAAJ*, 3:1896–1900, 1965.

[30] H.D. Hibbitt, P.V. Marcal, and J.R. Rice. A finite element formulation for problems of large strain and large displacement. *Int. J. Solids Struct.*, 6:1060–1086, 1970.

[31] R. Hill. *The mathematical theory of plasticity.* Oxford University Press, London, 1950.

[32] G.T. Houlsby. Personal communication. 1987.

[33] G.T. Houlsby. Personal communication. 1990.

[34] G.T. Houlsby and N.J. Withers. Analysis of the cone pressuremeter test in clay. *Geotechnique*, 38:573–587, 1988.

[35] G.T. Houlsby and C.P. Wroth. The influence of soil stiffness and lateral stress on the results of in-situ tests. *Proc. 12th ICSMFE, Rio de Janeiro*, 1:227–232, 1989.

[36] G.T. Houlsby, B.C. Clarke, and C.P. Wroth. Analysis of the unloading of a pressuremeter in sand. *Proc. 2nd symposium of the pressuremeter and its marine applications*, pages 245–262, 1986.

[37] J.M.O. Hughes and P.K. Robertson. Full displacement pressuremeter testing in sand. *Canadian Geotc. J.*, 22:298–307, 1985.

[38] J.M.O. Hughes, C.P. Wroth, and D. Windle. Pressuremeter tests in sands. *Geotechnique*, 27:455–477, 1977.

[39] G. Jaumann. Sitzungsberichte akad. *Wiss. Wien.*, 120:385, 1911.

[40] M. Jamiolkowski, C.C. Ladd, J.T. Germaine, and R. Lancellotta. New developments in field and laboratory testing of soils. *Proc. 11th ICSMFE, San Francisco*, 1:57–153, 1985.

[41] R.J. Jewell, M. Fahey, and C.P. Wroth. Laboratory studies of the pressuremeter test in sand. *Geotechnique*, 30:507–531, 1980.

[42] W.T. Koiter. General theorems for elastic-plastic solids. *Progress in Solid Mechanics (Ed. I.N. Sneddon and R. Hill)*, 1:165–221, 1960.

[43] R.D. Krieg and D.B. Krieg. Accuracies of numerical solution methods for the elastic perfectly plastic model. *ASME, Journal of Pressure Vessel Technology*, 99:510–515, 1977.

[44] S. Lacasse, T.B. D'orazio, and C. Bandis. Interpretation of self-boring and push-in pressuremeter tests. *Proc. 3rd Int. Symp. on Pressuremeters, ISP3, Oxford*, pages 273–285, 1990.

[45] B. Ladanyi. Expansion of a cavity in a saturated clay medium. *J. Soil. Mech. Fdns. Eng. Div. ASCE*, 89(4):127–161, 1963.

[46] B. Ladanyi. In-situ determination of stress-strain properties of sensitive clays with the pressuremeter. *Canadian Geotech. J.*, 9:313–319, 1972.

[47] J.E. Laier, J.H. Schmertmann, and J.H. Schaub. Effects of finite pressuremeter length in dry sand. *Proc. Conference on In-situ Measurement of Soil Properties, ASCE, Raleigh*, 1:241–259, 1975.

[48] M.E. Lauren and M. Gellert. Some criteria for numerically integrated matrices and quadrature formulas for triangles. *Int. J. Num. Meth. Eng.*, 12:67–76, 1978.

[49] T. Lunne and A.K. Parkin. Boundary effects in the laboratory calibration of a cone penetrometer for sand. *Proc. ESPT2, Amsterdam*, 2:761–769, 1982.

[50] R.J. Mair and D.M. Wood. *Pressuremeter testing - Methods and interpretation.* Butterworths, London, 1987.

[51] D.S. Malkus. A finite element displacement model valid for any value of the compressibility. *Int. J. Solids Struct.*, 12:731–738, 1976.

[52] D.S. Malkus and T.J.R. Hughes. Mixed finite element methods - reduced and selective integration techniques : a unification of concepts. *Comp. Meth. Appl. Meth. Eng.*, 15:63–81, 1978.

[53] M. Manassero. Stress-strain relationships from drained self-boring pressuremeter tests in sand. *Geotechnique*, 39:293–308, 1989.

[54] A. Marsland. Laboratory and in-situ measurement of the deformation moduli of london clay. *Proc. Symp. Interaction of Structure and Foundation, Birmingham*, pages 7–17, 1973.

[55] H. Matsuoka. On the significance of the spatial mobilized plane. *Soils and Foundations*, 116:91–100, 1976.

[56] R.M. McMeeking and J.R. Rice. Finite element formulations for problems of large elastic-plastic deformation. *Int. J. Solids Struct.*, 11:601–616, 1975.

[57] G.G. Meyerhof. The ultimate bearing capacity of wedge-shaped foundation. *Geotechnique*, 2(3), 1951.

[58] G.C. Nayak and O.C. Zienkiewicz. Elasto-plastic stress analysis : A generalization for various constitutive relations including strain softening. *Int. J. Num. Meth. Eng.*, 5:113–135, 1972.

[59] D.J. Naylor. Stresses in nearly incompressible materials by finite elements with application to the calculation of excess pore pressures. *Int. J. Num. Meth. Eng.*, 8:443–460, 1974.

[60] D.J. Nagtegaal, D.M. Parks, and J.R. Rice. On numerically accurate finite element solutions in the fully plastic range. *Comp. Meth. Appl. Mech. Eng.*, 4:153–177, 1974.

[61] J. Norbury and A.A. Wheeler. On the penetration of elastic-plastic material by a slender body. *Q.J. Mech. Appl.. Math.*, 40:477–492, 1987.

[62] S. Nordal and P. Antonsen. Plastic collapse loads by finite element methods. *Proc. 11th ICSMFE, San Francisco*, 2:603–606, 1985.

[63] J.G. Oldroyd. On the formulation of rheological equations of state. *Proc. Roy. Soc.*, 200:523–541, 1950.

[64] J.R. Osias and J.L. Swedlow. Finite elasto-plastic deformation - theory and numerical examples. *Int. J. Solids Struct.*, 10:321–339, 1974.

[65] A.C. Palmer. Undrained plane strain expansion of a cylindrical cavity in clays. *Geotechnique*, 22:451–457, 1972.

[66] J.J.M. Powell. A comparison of four different pressuremeters and their methods of interpretation in a stiff heavily overconsolidated clay. *Proc. 3rd Int. Symp. on Pressuremeters, ISP3, Oxford*, pages 287–298, 1990.

[67] W. Prager. An elementary discussion of definitions of stress rate. *Quart. Appl. Math.*, 18:403–407, 1961.

[68] I.C. Pyrah and W.F. Anderson. Numerical assessment of self-boring pressuremeter tests in a clay calibration chamber. *Proc. 3rd Int. Symp. on Pressuremeters, ISP3, Oxford*, pages 179–188, 1990.

[69] M.F. Randolph and C.P. Wroth. An analytical solution for the consolidation around a driven pile. *Int. J. Num. Analy. Meth. Geom.*, 3:217–229, 1979.

[70] M.F. Randolph, J.P. Carter, and C.P. Wroth. Driven piles in clay – the effects of installation and subsequent consolidation. *Geotechnique*, 29(4):361–393, 1978.

[71] P.W. Rowe. The stress-dilatancy relation for static equilibrium of an assembly of particles in contact. *Proc. Roy. Soc.*, 267:500–527, 1962.

[72] C. Sagaseta. Quasi-static undrained expansion of a cylindrical cavity in clay in the presence of shaft friction and anisotropic initial stresses. Research Report, Oxford University Engineering Science Department, 1984.

[73] R.T. Shield. On the plastic flow of metals under conditions of axial symmetry. *Proc. Roy. Soc.*, A.233:265, 1955.

[74] F. Schnaid. *A study of the cone-pressuremeter test in sand.* DPhil thesis, Oxford University, England, 1990.

[75] F. Schnaid and G.T. Houlsby. Calibration chamber tests of the cone-pressuremeter in sand. *Proc. 3rd Int. Symp. on Pressuremeters, ISP3, Oxford*, pages 263–272, 1990.

[76] S.W. Sloan. *Numerical analysis of incompressible and plastic solids using finite elements.* PhD thesis, Cambridge University, England, 1981.

[77] S.W. Sloan. Substepping scheme for the numerical integration of elasto-plastic stress-strain relations. *Int. J. Num. Meth. Eng.*, 24:893–911, 1987.

[78] S.W. Sloan and J.R. Booker. Removal of singularities in Tresca and Mohr-Coulomb yield functions. *Commun. Appl. Num. Meth.*, 2:173–179, 1986.

[79] S.W. Sloan and M.F. Randolph. Numerical prediction of collapse loads using finite elements. *Int. J. Num. Analy. Geomech.*, 6:47–76, 1982.

[80] C.I. Teh. *An analytical study of the cone penetration.* DPhil thesis, Oxford University, England, 1987.

[81] C.I. Teh and G.T. Houlsby. Analysis of the cone penetration test by the strain path method. *Proc. 6th Int. Conference on Numerical Methods in Geomechanics, Innsbruck*, 1:397–402, 1988.

[82] M.T. Toh and S.W. Sloan. Finite element analyses of isotropic and anisotropic cohesive soils with a view to correctly predicting collapse. *Int. J. Num. Analy. Meth. Geomech.*, 4:1–23, 1980.

[83] C. Truesdell. The mechanical foundations of elasticity and fluid dynamics. *J. Rat. Mech. Analys.*, 2:593–616, 1953.

[84] M.T. Tumay, Y.B. Acar, M.H. Cekirge, and N. Ramesh. Flow field around cones in steady penetration. *J. Geo. Eng. Div. ASCE*, 111:193–204, 1985.

[85] A.S. Vesic. Expansion of cavities in infinite soil mass. *J. Soil. Mech. Fdns. Div. ASCE*, 98:265–290, 1972.

[86] N.J. Withers, J. Howie, J.M.O. Hughes, and P.K. Robertson. Performance and analysis of cone pressuremeter tests in sands. *Geotechnique*, 39:433–454, 1989.

[87] N.J. Withers, L.H.J. Schaap, and J.C.P. Dalton. The development of a full displacement pressuremeter. *Proc. 2nd Symposium of the Pressuremeter and its Marine Applications*, pages 38–56, 1986.

[88] C.P. Wroth. The interpretation of in-situ soil tests. *Geotechnique*, 34(4):449–489, 1984.